MULTISCALE CHARACTERIZATION OF FERROELASTIC DEFORMATION IN CERAMIC MATERIALS

BY

CHARLES SHERIDAN SMITH

DISSERTATION

Submitted in partial fulfillment of the requirements
for the degree of Doctor of Philosophy in Materials Science and Engineering
in the Graduate College of the
University of Illinois at Urbana-Champaign, 2020

Urbana, Illinois

Doctoral Committee:

Assistant Professor Jessica A. Krogstad, Chair
Associate Professor Shen J. Dillon
Professor John Lambros
Professor Nancy R. Sottos

ABSTRACT

Ceramic materials offer a variety of useful properties that make them desirable for a wide range of engineering applications, however, ceramics are limited in their utility by low toughness. Ferroelastic deformation provides a mechanism through which ceramics are intrinsically toughened, but the effect of microstructure on the deformation behavior has yet to be fully understood. In this present examination, the behavior of ferroelastic deformation was evaluated on a range of length scales, specifically highlighting the influence of several variables on the domain nucleation behavior.

Ferroelastic domain nucleation was first evaluated in micro-scale single crystals. The stress required for domain nucleation was measured while crystal orientation was tracked. Domain nucleation was observed to not follow a critical resolved shear stress criterion, suggesting that orientation alone cannot be used to predict the deformation behavior. Furthermore, multiple types of deformation were observed to act in concert with ferroelastic deformation. This suggests that domain nucleation is a complex process that may involve multiple potential mechanisms of deformation.

Domain nucleation in bulk polycrystals was also examined. Statistics collected on grain sizes that more frequently contain mechanically nucleated domains show that larger grains in close proximity to finer grains more frequently deform. The deformation behavior in polycrystals was contrasted against the domain nucleation behavior in single crystal nanopillars. The nanopillars exhibited high deformation stress, while prolific domain nucleation without fracture was observed in polycrystals. These results suggest that local constraints imposed by microstructure play a key role in locally increasing shear stresses responsible for domain nucleation.

To design microstructures with specific characteristics, ceramic processing routes must also be developed to control microstructural development during fabrication. To this end, spark plasma sintering (SPS) offers a promising processing route for fabricating dense nanostructured ceramics. The densification mechanisms associated with ceramic processing using SPS have also been investigated in the present work. Results collected on many samples that were processed under identical processing control conditions convey significant variability in the resulting material properties between and within individually produced samples. Furthermore, the results

indicate that electric current plays an important role in densifying ionic conducting ceramics during sintering using SPS.

Overall, the research presented in this dissertation shows that ferroelastic domain nucleation is a complex process involving several competing and cooperating mechanisms, and that domain nucleation is affected by different microstructural variables. Domain nucleation cannot be predicted based solely on crystal orientation, however, other microstructural variables including grain size do significantly impact the ferroelastic deformation behavior. Microstructures with large ferroelastic grains embedded in a more finely grained matrix promote ferroelastic deformation even without fracture, and the deformation is sensitive to the stress state being applied. Several processing routes presented here result in these favorable bimodal grain size distributions and may be tested more thoroughly in the future to explore the effect that such microstructures have on the intrinsic toughness.

Dedicated to my family.

ACKNOWLEDGMENTS

I am very grateful to my advisor, Prof. Jessica Krogstad, for her support and encouragement throughout my graduate degree. Her guidance has helped me become a better researcher and she has helped me find a home in the ceramics research community. I want to thank the rest of my committee members, Prof. Shen Dillon, Prof. Nancy Sottos, and Prof. John Lambros for their advice on this research as well.

I also must thank my labmates and friends: Pralav Shetty, Nathan Madden, Megan Emigh, and all the other members of the Krogstad group for creating a collaborative, friendly, and enjoyable place to work. This work would not have been possible without the many discussions we had. I will miss the late nights and early mornings brainstorming experiments and fighting with lab equipment with them. Nothing is better than working with your best friends.

The friends I have made during graduate school are truly the best people I could have ever imagined meeting. I consider myself extremely lucky to have such a supportive group of people who were always willing to talk about life or research. Thank you to Wang Xiang, Blanka Janicek, Aidan Gilchrist, Becca McAuliffe, Scott McCormack, Jacob Rueben, Ben Hulbert, Josh Leveillee, Siddharth Krishnan, and many others. I sincerely could not have done it without all of you. Thank you.

Finally, I want to thank my family. My parents Thomas Smith and Julie Sheridan-Smith, brother Maxwell Smith, sister Margaret Smith, and the rest of my extended family have provided me with endless love and support. I would not be the person I am today without all of you.

TABLE OF CONTENTS

CHAPTER 1

INTRODUCTION

1.1 Motivation

Ceramic materials offer a variety of useful properties for many types of engineering applications. For instance, ceramics often have excellent chemical and thermal stability, making them useful for thermal barrier coatings with resistance to degradation through oxidation and corrosion [1–4]. Ceramics also often have exceptional strength compared to other engineering materials such as metals and polymers, making them desirable for use in structural applications. Electrical properties such as high dielectric constants [5], piezoelectricity [6], ferroelectricity [7], and superconductivity [8,9] also greatly expand ceramics desired application range into a wide variety of electrical devices such as capacitors, actuators, and sensors of many varieties.

Unfortunately, despite their high strength, ceramics typically are hindered by considerably low toughness due to their limited ability to deform prior to fracture [10]. This low toughness is often a significant limiting factor in designing ceramics into their desired applications, therefore, many efforts have been made to toughen ceramics [11]. Some conventional methods used to toughen ceramics include modifying chemistry and thermodynamic stability giving the material the ability to increase toughness through stress induced phase transformations, which has proved to be very effective [12–14]. Engineers have also modified microstructures to increase toughness through the addition of second phase fibers, or by creating high aspect ratio grains that must be pulled out of a crack during fracture [15–18]. Unfortunately, many of these existing toughening strategies begin to fail in extreme environments. For instance, at high temperatures, phase transformation toughening impossible because there is no longer a thermodynamic driving formce for transformation [3]. Adding second phases to materials such as piezoelectrics generally deteriorates their desired properties as well [15,19].

This means that there is strong motivation to develop toughening mechanisms that do not rely on these external modifications of the material, but rather are active in a stable single phase material. It is even more beneficial if toughening can be active before a crack is introduced into the material since crack initiation is often failure itself. Such toughening mechanisms are termed “intrinsic toughening” mechanisms and will be discussed in detail in the next section. Ferroelastic

deformation in ceramics provides this type of toughening and may be active in many types of structural and electrical ceramics, making it particularly interesting and important to understand [20–27]. The aim of the research discussed in this dissertation was to determine how different microstructural variables impact ferroelastic deformation with the goal of developing an improved understanding of how microstructures may be designed to best take advantage of the intrinsic toughening that ferroelasticity provides.

This study was done by evaluating ferroelastic deformation on a range of scales. First, ferroelastic deformation was studied in single crystals, so that the fundamental domain nucleation and motion behaviors can be understood. Then, ferroelastic deformation was evaluated in more realistic polycrystalline microstructures. By comparing what was learned about ferroelastic deformation in single crystals to the behavior observed in polycrystals, the effect that microstructure has on this type of deformation was highlighted. This improved understanding of ferroelastic deformation in ceramics will ultimately allow us to bridge our understanding of how deformation behaves from the microscale to bulk materials, allowing for informed design of toughened ceramics.

The merit of understanding ferroelastic deformation is not limited to the context of toughening mechanisms since understanding ferroelasticity also furthers our fundamental knowledge of deformation mechanisms in ceramics. Expanding fundamental knowledge of materials behavior serves as a worthy scientific motivation, particularly when the unknown nature of future engineering endeavors is considered. Therefore, the motivations of this study may be considered to have merit in improving both the basic scientific understanding of ceramic deformation, as well as in improving the understanding of how to better engineer ceramics for improved toughness. However, toughening serves as a primary cohesive motivation for the engineering focus of this study, and therefore will be discussed in more detail in this dissertation.

This chapter introduces ferroelastic deformation as an intrinsic toughening mechanism and puts into context the reasons that currently exist for studying the nature of ferroelastic deformation for the purpose of toughening ceramic materials. Toughness will be described, as will the current state of the literature on ferroelastic deformation. Other mechanisms involved in deformation of ceramics will then be discussed. Finally, the specific objectives and hypotheses that motivate this research will be outlined.

1.2 Toughness and Toughening Mechanisms

Generally speaking, toughness is defined as a material's ability to absorb energy during deformation rather than releasing strain energy through the creation of new surfaces by fracturing. This energy absorption often takes place through deformation mechanisms such as dislocation motion, deformation twinning, and stress induced phase transformations. The toughness of a material is often described as the total energy absorbed (excluding elastic energy) during failure which can be found by integrating the area under the corresponding stress-strain curve. The extensive field of fracture mechanics has been developed in order to understand how materials fail through crack initiation and propagation, such that their failure behavior may be better predicted and designed against. The term fracture toughness refers more specifically to the definition of conditions that cause the extension of a crack from an existing flaw. Fracture toughness is also associated with quantification of material parameters such as a critical stress intensity factor, K_c, or critical strain energy release rate, G_c, that define those conditions for fracture [28]. Here, fracture toughness and toughening will be discussed in the context of defining and understanding intrinsic and extrinsic mechanisms, since it is important to distinguish and understand these different mechanisms to understand and motivate the study of ferroelastic deformation.

Fracture toughness is often defined in a few different ways. Several simplified and generalized fracture toughness parameters will be described here. One of the first ways of thinking about a crack propagation criterion is often attributed to Griffith, who used an energy-based criterion to define when a crack propagates [29]. The Griffith criterion may be written as

$$G_c = \frac{\sigma_f^2 \pi a}{E} \qquad \text{Equation 1.1}$$

where G_c is the critical energy release rate (fracture toughness), σ_f is the stress for failure, a is the crack length, and E is the elastic modulus. The energy terms within G_c contain the surface energy associated with creating two new surfaces as a crack advances as well as energy from plastic deformation.

The Griffith criterion does not explicitly account for the actual crack tip geometry and stress concentration that occurs there. Because of this, alternative fracture toughness criteria using

stress intensity factors have been developed, first proposed by Irwin [30]. A generalized critical stress intensity factor for crack opening geometries can be expressed as

$$K_c = \sigma_f \sqrt{\pi a} \qquad \text{Equation 1.2}$$

where K_c is the critical stress intensity factor (fracture toughness), and the other variables are the same as they were for G_c. For purely elastic cracks, G_c and K_c are equivalent and can be related through

$$G_c = \frac{K_c^2}{E} \qquad \text{Equation 1.3}$$

However, materials are rarely purely elastic. There are numerous other parameters used to define crack propagation behavior including the J-integral [31] and crack tip opening displacement (CTOD) [32]. Along with these parameters, many different experimental techniques for measuring fracture toughness have been developed that use a variety of sample geometries and crack conditions to quantify material toughness [28]. In the research presented in this dissertation, no quantification of toughness was done, however, it is important to appreciate the concepts involved in toughness and toughening to appreciate the motivation for this work. The key takeaway from this perspective on fracture toughness is that cracks propagate when the strain energy or stress intensity surrounding a crack reaches a critical point, therefore, methods that increase the energy stored in the material before fracture or that can dissipate stress around a crack will increase toughness.

Toughness and toughening mechanisms can be broken into two categories: intrinsic and extrinsic. Here intrinsic mechanisms will be defined as any processes taking place ahead of (or in absence of) a crack tip, whereas extrinsic mechanisms are active behind a crack tip. A schematic crack growth resistance curve (R-curve) for a material exhibiting increased resistance to crack growth with increasing crack length is shown in Figure 1.1. Intrinsic mechanisms increase toughness before a crack advances, as shown by $\Delta\Gamma_{int}$ (Γ is another variable often used to define energy-based toughness and is the same as G) indicating an increase in toughness with zero crack extension Δa. $\Delta\Gamma_{ex}$ shows increase in toughness due to extrinsic mechanisms. It can be seen that the fracture toughness increases as the crack extension proceeds and the extrinsic process zone increases in size until a maximum steady state fracture toughness is reached.

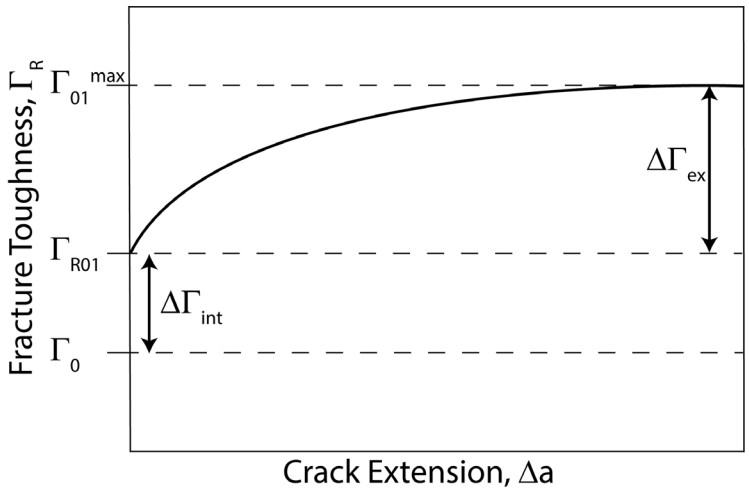

Figure 1.1: Schematic crack growth resistance curve showing changes in toughness due to intrinsic and extrinsic toughening.

Ferroelastic deformation actually provides both intrinsic and extrinsic toughening. A schematic of a ferroelastic process zone can be seen in Figure 1.2. The specifics of ferroelastic deformation will be discussed in the next section, however, from the schematic it can be seen that any ferroelastic deformation that takes place due to stresses acting ahead of the crack tip will contribute to intrinsic toughening, while the deformation that results from ferroelastic switching (a term used for ferroelastic domain reorientations) also acts to impose crack closure stresses in the crack wake, also contributing to extrinsic toughening. The increase in toughness due to the ferroelastic contribution toughening, $\Delta\Gamma$, has been described using the following relationship:

$$\Delta\Gamma = 2h\tau^T\gamma^T f \qquad \text{Equation 1.4}$$

where h is the width of the process zone, τ^T and γ^T are the coercive shear stress and shear strain for domain switching, and f is the volume fraction of material within the process zone experiencing the coercive strain [11]. Essentially, this toughening equation states that the increase in toughness due to ferroelastic deformation comes from the sum of the energy absorbed by material experiencing ferroelastic deformation (with its associated critical stress and resulting strain) in the process zone. The primary contribution to toughness that the work in this dissertation is concerned with is the intrinsic toughening contribution, and the work that is presented in following chapters focuses on types of ferroelastic deformation that are relevant to deformation ahead of or in absence of a crack.

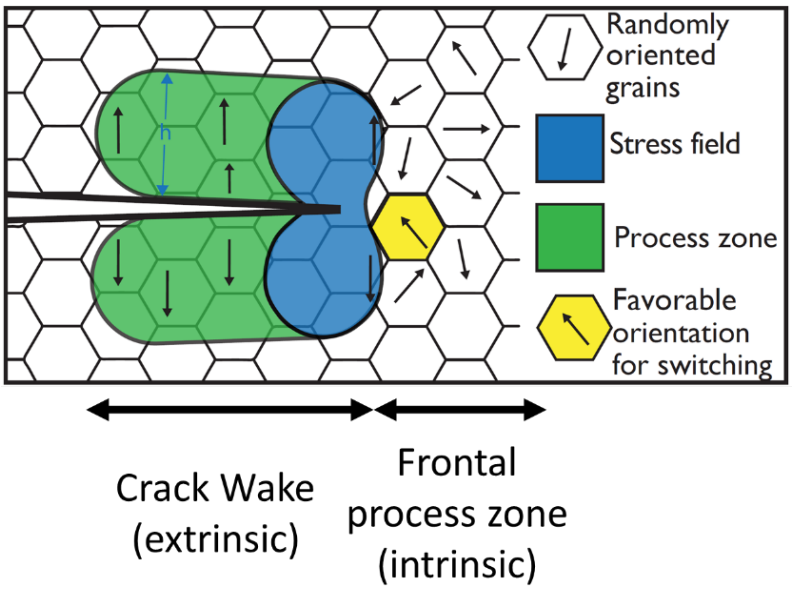

Figure 1.2: Schematic of a ferroelastic process zone around an advancing crack in a polycrystal. The orientation of domains has been shown by arrows within grains, for which only some of the grains will favorably reorient. Domains that reorient are aligned in the crack wake.

1.3 Ferroelasticity

A ferroic material is defined as a material which has two or more orientation states in the absence of an external stimulus (i.e. stress, electric field, magnetic field) that can be shifted in response to an external stimulus. Ferroic materials exhibit reversible switchability between these orientation states, resulting in hysteresis [33,34]. Ferroelasticity, like the other primary ferroic behaviors (ferroelectricity and ferromagnetism) shows this hysteretic behavior, specifically between stress and strain. An example of this hysteresis is shown in Figure 1.3.

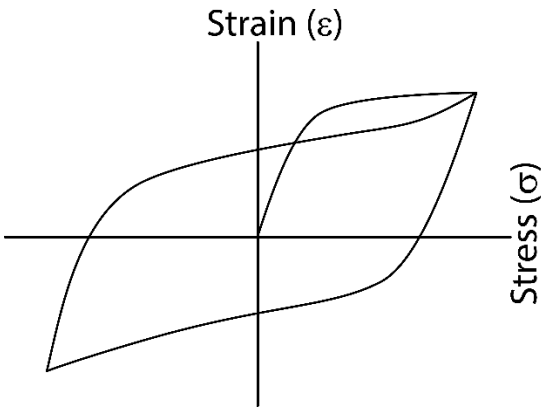

Figure 1.3: Stress-strain hysteresis in a ferroelastic alloy, showing the reversibility of deformation from ferroelasticity, adapted from Wadhawan [35].

This hysteresis relies on the nucleation of domains which differ in orientation states. The requirement of having multiple different orientation states available means that ferroic materials must have some degree of crystallographic anisotropy. In ferroelastic materials, this anisotropy is found in the crystal structures. Ferroelastic domains have different crystallographic orientation and are bounded by twins. The specific orientation relationships between ferroelastic domains, therefore, depends on crystal structure. Here, the tetragonal crystal structure will be discussed since it is relevant to many different ferroelastic ceramics and it is relatively easy to visualize the differences in orientation states. The work presented in this dissertation also primarily was performed on materials with tetragonal crystal structures. In tetragonal crystals, three different relative orientation states exist and are based on the direction of the elongated c-axis of the tetragonal unit cell. The three orientation states are shown schematically in Figure 1.4.

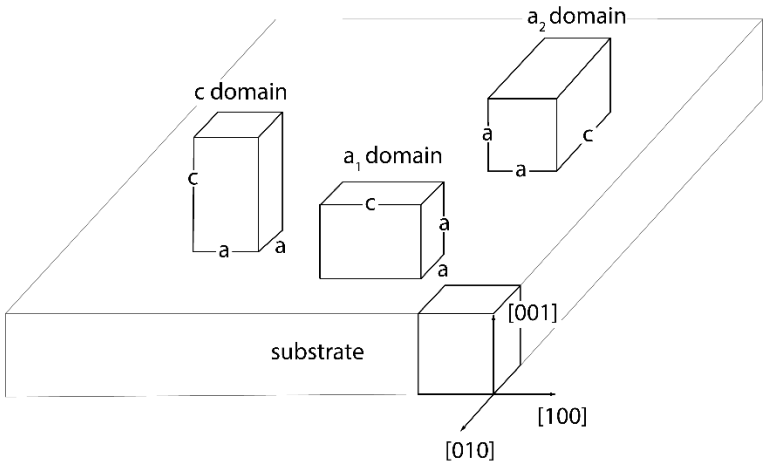

Figure 1.4: Three unique orientation states defining different domains in a tetragonal crystal. The c-axis can align along any of the three principle parent axes, represented as substrate axes here, adapted from Lee [36].

Another consequence of the definition of ferroelasticity is the specification of stresses and strains associated with the domain reorientations. Following the conventional terminology used for ferroics, these characteristic stresses and strains are termed the coercive stress and coercive strain. In this dissertation, the value of coercive stress in particular will be considered. It is important to distinguish between stresses necessary for domain nucleation, and for domain motion. Idealized stress-strain curves showing the difference between domain nucleation and motion are shown in Figure 1.5. Here, the positive stress and strain axes represent a compressive stress, as shown being applied to the representative tetragonal crystal below. It has been previously proposed

that domain nucleation requires higher stress (or additional energy input) than domain motion or propagation [37]. Consequently, domain nucleation may be more effective than domain motion for toughening purposes.

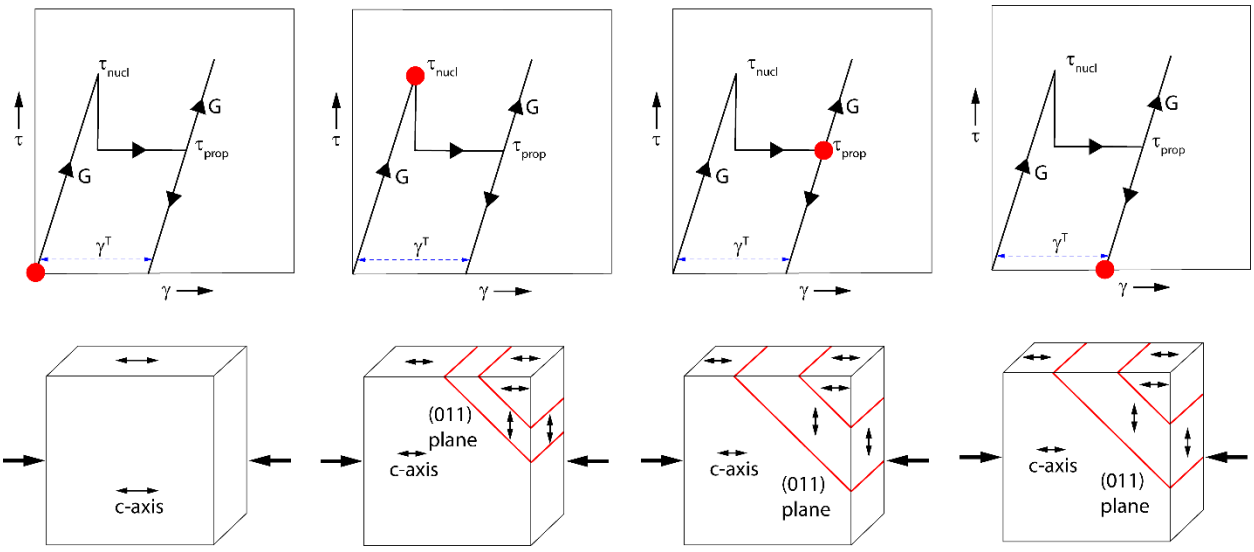

Figure 1.5: Idealized compressive stress-strain curves showing domain nucleation and propagation by a 90° reorientation of the tetragonal c-axis by twinning across the {011} family of planes. Each crystal represents an idealized domain configuration present when the associated stress and strain levels are reached, which are marked by red dots on the corresponding stress-strain curves. The shape of the stress-strain curve has been adapted from Mercer [24].

Ferroelastic domains form in order to the minimize elastic energy in crystals via the formation of twin boundaries in the material. When considering energies associated with domain formation (not including magnetic or electric contributions), the total energy, ω_{tot}, in a material can be expressed as

$$\omega_{tot} = \omega_E + \omega_W + \omega_S \qquad \text{Equation 1.5}$$

where ω_E represents elastic energy, ω_W represents domain wall energy, and ω_S represents surface energy [38]. Nucleation of these domains to minimize energy often occurs during structural phase transitions that occur when a material cools from a higher symmetry paraelastic phase to a lower symmetry ferroelastic phase. Domain nucleation may also occur during external mechanical deformation, which is beneficial for the case when toughening is desired. Domain nucleation and motion under stress absorbs energy as described by Equation 1.4. Domains may form into various energy minimizing structures examples of which are provided in Figure 1.6. To fulfill mechanical compatibility requirements, the particular type and arrangement of twins depends on the crystal

structure of the material as well as microstructural factors, including grain size and relative crystal orientations [39].

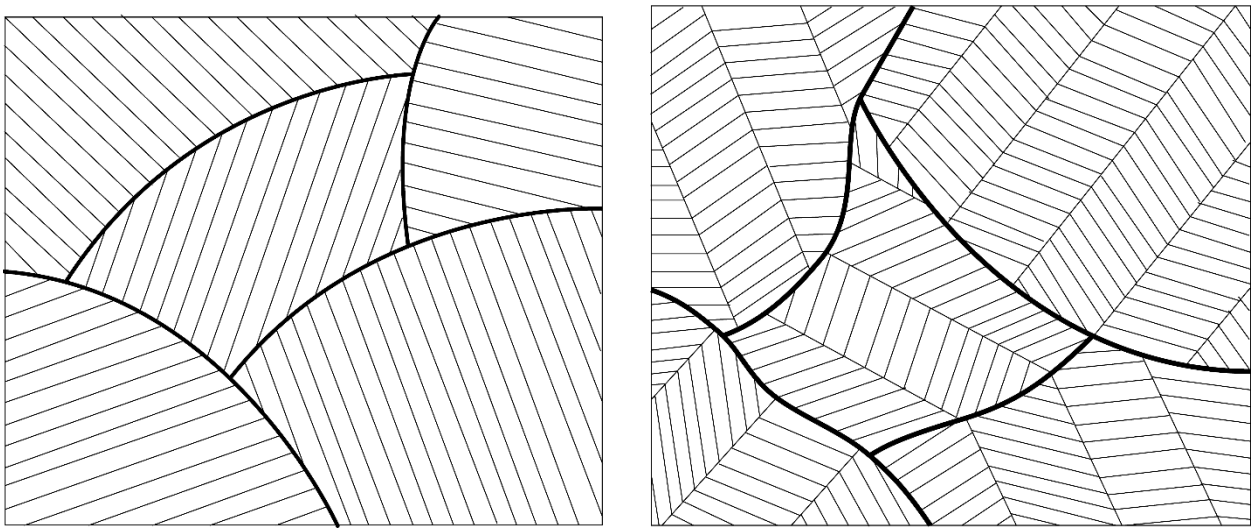

Figure 1.6: Schematic representations of lamellar (left) and banded (right) twin structures that form as a result of elastic energy minimization, adapted from Arlt [38]. Each domain differs in orientation relative to its surrounding domains.

In ferroelastics, the crystallographic anisotropy often leads to anisotropy in other properties such as elastic modulus, which affects locally how elastic energy is stored and released according to Equation 1.5. Even amongst materials with the same crystal symmetry, degrees of elastic anisotropy can differ, which will influence how the materials domain structures evolve. For instance, tetragonal yttria stabilized zirconia and tetragonal barium titanate have the same crystal symmetry, however, they have highly different elastic moduli and elastic anisotropy. Figure 1.7 shows the tetragonal crystal structures for both of these materials along with their elasticity tensors from Lunt and Wang, respectively [40,41]. Figure 1.8 then shows how the elastic modulus of each of these materials varies with crystal direction, calculated using the elasticity tensors from Figure 1.7. It can be seen that the modulus values as well as how they differ with orientation are not the same for these materials despite having the same crystal symmetry. Differences such as these influence how the stress-strain relationships that develop within microstructures during ferroelastic deformation.

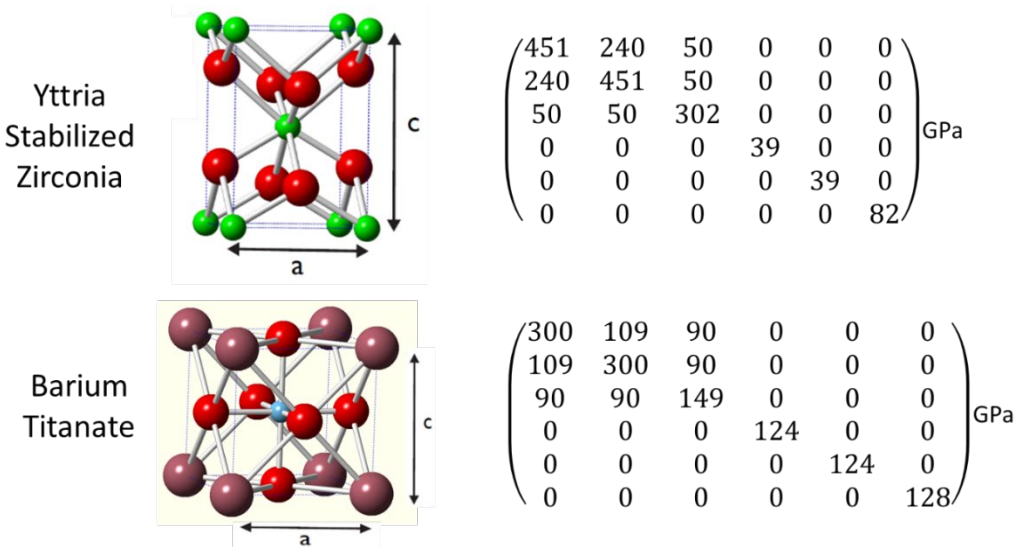

Figure 1.7: Crystal structures and elastic tensors for yttria stabilized zirconia and barium titanate. The yttria stabilized zirconia structure is shown without distinction between yttrium and zirconium cations (no vacancies are shown either) since they are disordered, while the barium and titanium atoms are distinguished in the tetragonal barium titanate structure.

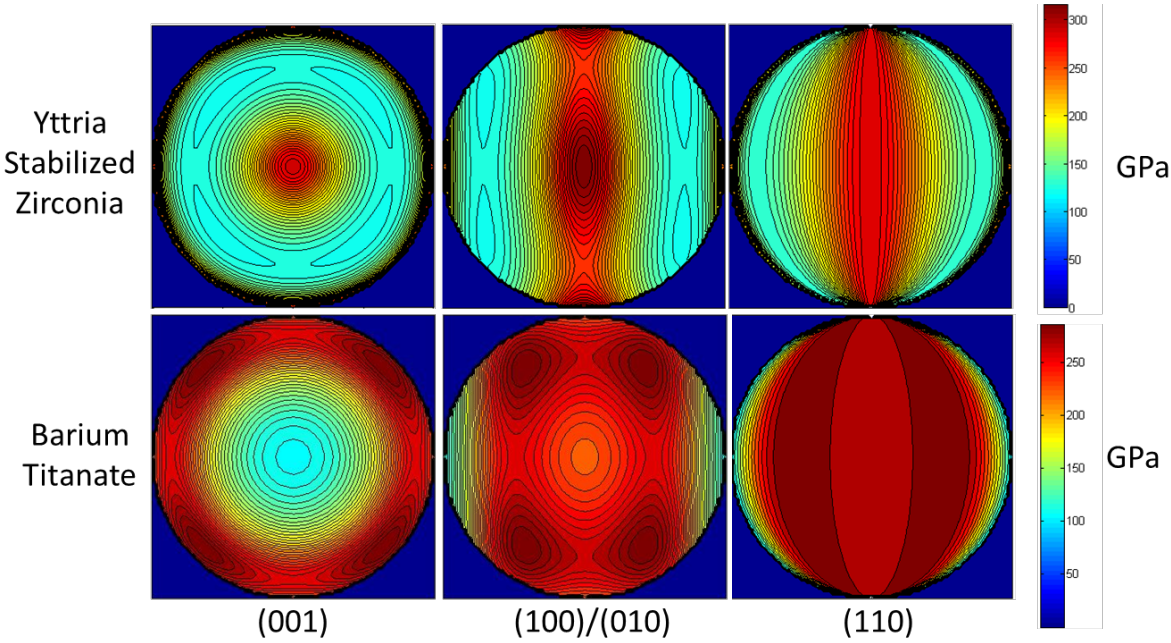

Figure 1.8: Pole figures showing elastic moduli for yttria stabilized zirconia and barium titanate. The projections along the (001), (100/(010) and (110) plane normal are shown. The color indicates the modulus value for a given direction and is indicated by the color gradient legends for each material.

1.4 Previous Characterization of Ferroelastics

Previous studies have done extensive work to characterize ferroelastic deformation and the impact it has on toughening in a wide variety of ceramic materials. Here, a section of that work with emphasis on materials and structures relevant to the present study will be discussed.

Much of the previous work that has been done on ferroelastics has focused on describing the toughening that results from ferroelastic deformation, and the effect that it has on the bulk deformation behavior. Previous studies have used macroscopic measurements to show that nonlinear, ferroelastic deformation in ceramics can increase the toughness by approximately 40-100% [42–44]. Many studies have shown that tetragonal ferroelastic materials such as lead zirconate titanate (PZT) [45,46], barium titanate (BTO) [25,47], and yttria and ceria stabilized zirconias (YSZ and CSZ) [48–50], exhibit R-curve toughening behavior as well as macroscopic hysteresis in their stress-strain response. This behavior has also been seen in other crystal structures such as orthorhombic ceramics such as lanthanum cobaltite (LCO) [51,52], lead niobite, and bismuth titanate [46], as well as monoclinic structures like bismuth vanadate [53]. However, in these previous studies. it has been difficult to deconvolute the contribution to the toughening that ferroelasticity provides from other toughening mechanisms such as crack bridging.

These macroscopic measurements do not consider the local mechanical compatibility requirements that may lead to incomplete or inefficient minimization of elastic energy by domain formation. Local deviations from bulk behavior often occur as a result of microscale heterogeneity in materials. Because of this, more recent work has focused on developing microscale understanding of how ferroelastic domains develop. Techniques such as x-ray and neutron diffraction have been used to measure domain reorientation during straining [45,54,55], while others have used more local measurements by piezoresponse force microscopy to observe local domain structures within grains directly [39]. Scanning and transmission electron microscopy is also commonly used to observe domain structures at the microscale as well as the nanoscale [56–59].

In many of these previous studies, there has been a focus on characterizing the domain conformations and morphology that results either from nucleation during phase transformations or from propagation and rearrangement of domains during deformation. For example, studies have characterized the geometries of domain colonies that form in tetragonal zirconia and barium

titanate during phase transformations [38,56–58]. Domains may form complex arrangements within single crystals, an example of which is shown in Figure 1.9.

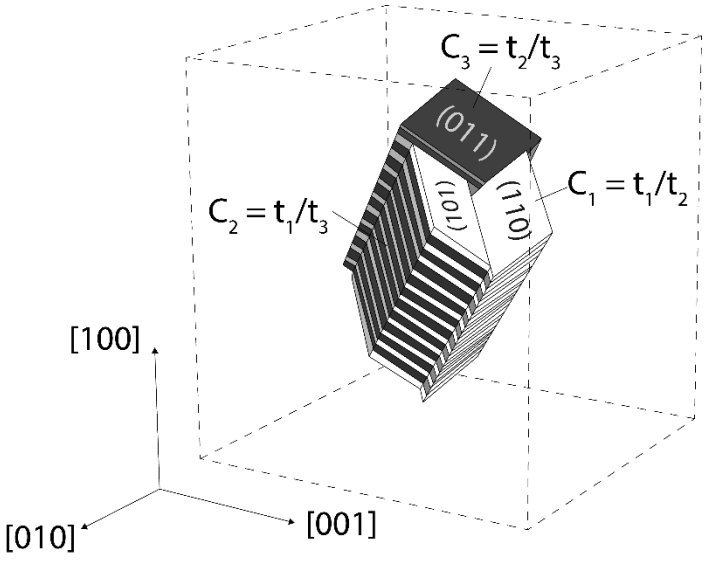

Figure 1.9: Schematic adapted from Baither et al. [56] showing the colony structure of domains in tetragonal YSZ. Domains align along the <111> axis and consist of multiple layers of {110} twins. It is also shown that the different colonies C1, C2, and C3 are bounded by {110} planes, however, specific domains between colonies are equivalently oriented such that domains may be shared across colonies.

The twins/domains form on multiple scales, with hierarchical structuring. It has also been shown that the boundary conditions imposed by the clamping of the surrounding microstructures have a significant impact on the morphology of domains that form during cooling [38]. Furthermore, *in situ* studies of the domain evolution during straining show that domain structures can progress through energetically unfavorable conformations due to the constraints of microstructure [39]. This highlights a need to understand the effect that specific microstructural features are having on the deformation processes.

Work has also been done to characterize domains that mechanically nucleate within fracture process zones, and to measure the coercive stresses associated with domain switching. Mercer characterized the width of the ferroelastic process zone in YSZ, and used Equation 1.4 to infer the coercive stress to be approximately 580 MPa [37]. Baither also characterized the coercive stress for YSZ, and found it to range from approximately 285-750 MPa with dependence on temperature and strain rate [58]. It will be interesting to compare these coercive stress values to those found for ceria-titania stabilized zirconia discussed later in this dissertation.

Coercive stress values have also been measured for a variety of other ferroelastic materials. For example, Jones measured coercive stress values in tension and compression of a number of materials including niobium doped PZT, strontium doped PZT, bismuth titanate, lead niobite, and lead titanate which had compressive coercive stress values of 11, 20, 40, 26, and 38 MPa respectively [46]. However, Jones also noted that these coercive stress values actually represent a median or mode of a distribution of coercive stress values found in the many grains of a polycrystal. This highlights the need to evaluate the effect that microstructure is having on domain dynamics in polycrystals, and to relate that to what is known about the behavior in single crystals.

Finally, it is important to discuss the modelling and simulation work that has been done on ferroelasticity. Authors have used techniques such as phase field modelling to predict domain evolution during fracture processes [60]. Constitutive models have also been developed to investigate the contribution to toughening from ferroelastic domain switching as well as strain saturation conditions in crack wakes through finite element modelling that take into account the anisotropy of ferroelastic deformation [61,62]. However, these models still do not take into account local heterogeneity present in polycrystalline ceramic microstructures, but rather determine stress fields using far field fracture mechanics descriptors.

What is clear from this previous work is that understanding must be developed connecting the microscale understanding of ferroelastic deformation to the macroscale response. In order to intelligently design microstructures to take advantage of ferroelastic deformation for toughening, specific microstructural features that influence ferroelasticity, and how they influence the deformation must be known. The experiments presented in this dissertation were designed with this in mind and seek to bridge our understanding of ferroelasticity across length scales.

1.5 Alternative Deformation Mechanisms in Ceramics

Despite not typically being thought of as deformable, ceramics can at times exhibit other types of deformation besides ferroelastic deformation. Here, several types of alternative deformation mechanisms found in ceramics will be outlined, with emphasis on mechanisms and types of defects found in tetragonal zirconia and ceramics similar to the zirconia-based materials primarily being studied here.

As has been mentioned previously, ceramics such as zirconia typically fail through brittle fracture, however, at conditions such as high temperature or small size scale, it is possible to activate dislocation plasticity. There are relatively few studies that have explicitly characterized dislocations in zirconia, but some previous studies of dislocations do exist on yttria stabilized zirconia (YSZ). Dislocations in YSZ have been observed to form on {100}, {110}, and {111} planes [63,64], but dislocations will only be complete if the burgers vector lies in the (001) basal plane [63]. That means that any dislocations outside of the (001) basal plane will be partial dislocations, which can dissociate and form stacking faults. In tetragonal (*t'*) YSZ, this dislocation activity is almost always preceded by ferroelastic deformation at temperatures up to 1000°C, however, the ferroelastic deformation may be accompanied by dislocation motion at high stress [63].

Different dislocation types that are active in zirconia will interact differently with the microstructures that are present. For example, complete (basal) dislocations behave as fairly standard dislocations and can interact with precipitates and other dislocations to form jogs, kinks, and locks. Alternatively, for example, when dislocations with 1/2 <110> Burgers vectors, which are partial dislocations, are found to be active, as they pass through multiple domains of tetragonal zirconia with different orientations, they create stacking faults and antiphase boundaries on the oxygen sublattice between the domains [63]. These additional defects may then affect the subsequent deformation behavior. Furthermore, partially stabilized zirconia, which contains both cubic and tetragonal phases after ageing, exhibits precipitation hardening due to the tetragonal phase precipitates interacting with active dislocations [63].

Size scale can also influence the plastic deformation of zirconia. At high temperatures and small grain sizes, zirconia has been shown to exhibit superplastic deformation, however, this deformation is attributed to diffusional creep rather than dislocation plasticity [65]. Reductions in overall sample volumes also lead to increased plasticity due to decreased likelihood of fracture due to critically sized flaws [66]. Very high strength as well as very high strains at failure have been observed for small scale zirconia samples relative to bulk samples. Size dependent plasticity in zirconia may occur through both dislocation plasticity as well as phase transformations, the mechanisms for which may compete within samples [64,66,67]. Samples with high surface area to volume ratios can accommodate significantly higher strains compared to their bulk counterparts.

Increasing surface area to volume ratios not only increases dislocation plasticity before fracture, but reduces mismatch stresses that form during phase transformation, allowing for much higher strain due to phase transformations [68,69]. Deformation by phase transformations will now be discussed.

At ambient temperatures, dislocation plasticity is rare, so phase transformations are often used as an alternative deformation mechanism. To activate stress induced phase transformations, it is important to control the thermodynamic stability of the phases in the material, such that metastable phases are able to transform without application of heat. Stabilization of the tetragonal and/or cubic phases of zirconia can be done using a variety of cation dopants [70]. The grain size or particle size of zirconia also affects the overall phase stability as well as the phase transformation behavior [71–73]. Once materials are able to release energy through phase transformations, they experience deformations due to the volume change associated with the phase transformation as well as the change in shape that results from the change in symmetry. Both of these contributions to the deformation can combine leading to significant deformation, as well as significant contributions to toughening as discussed previously.

1.6 Objectives and Hypotheses

Overall, the objective of this study was to develop a fundamental understanding of the relationship between local microstructure and the activation of ferroelastic deformation to contextualize how microstructure may be tuned to design durable ceramic materials. To accomplish this, ferroelastic deformation was evaluated on a range of length scales. The specific hypotheses being evaluated in this dissertation include:

- Ferroelastic domain nucleation is governed by a critical resolved shear stress criterion. Shear stresses in single crystals may be resolved onto specific planes and related to a critical value as is done for slip in Schmid's law.
- Local microstructural features such as grain size and orientation influence the probability and extent of ferroelastic deformation in ceramics due to mechanical compatibility requirements and elastic energy minimization.

To test these hypotheses, several research tasks were identified, and include:

- Fabricate a range of microstructures using ceramic processing techniques to characterize the influence of various microstructural features on ferroelastic deformation.
- Evaluate the effect that crystal orientation has on domain nucleation using electron backscatter diffraction combined with micropillar compression. Measure the coercive stress for domain nucleation for a range of crystal orientations.
- Evaluate the mechanisms associated with ferroelastic deformation in small scale single crystals using micropillar compression and nanoscale *in situ* TEM deformation.
- Deform polycrystalline samples using microindentation to determine whether variables such as grain size and grain conformation have an effect on ferroelastic domain nucleation.

Preliminary work has also been done to evaluate additional relationships between microstructure and ferroelastic deformation that have not yet been completed. The methods used and developed to perform these tasks will be discussed in Chapter 2, and some future directions that may be taken will be discussed in Chapter 6. These include:

- Characterize orientations favorable for ferroelastic deformation using micro-indentation coupled with electron backscatter diffraction (EBSD).
- Characterize local strain heterogeneity developed during ferroelastic deformation of specific grains in a polycrystalline sample using digital image correlation (DIC) and *in situ* scanning electron microscopy (SEM).
- Correlate local strain heterogeneity to the local microstructure using EBSD before and after *in situ* SEM deformation.

There is a secondary objective that will also be discussed in this dissertation that relates specifically to developing advanced ceramic processing techniques through improving our understanding of densification behavior of ionic conducting ceramics processed by spark plasma sintering (SPS). The hypothesis being tested for this objective is:

- Electric current plays a role in the densification of ionic conduction ceramics processed by spark plasma sintering.

To test this hypothesis the following research task is identified:

- Sinter a number of yttria stabilized zirconia samples with different conformations inside of an SPS die such that statistics on the variability in the resulting properties can be measured.

These two objectives focus on testing different fundamental hypothesis, however, they are linked by the fact that each study at its core is designed to evaluate the processing-microstructure-property relationships that are so important to understand when designing materials for all kinds of engineering applications.

1.7 References

[1] N.P. Padture, M. Gell, E.H. Jordan, Thermal Barrier Coatings for Gas-Turbine Engine Applications, Science (80-.). 296 (2002) 280–284. https://doi.org/10.1126/science.1068609.

[2] X.Q. Cao, R. Vassen, D. Stoever, Ceramic materials for thermal barrier coatings, J. Eur. Ceram. Soc. 24 (2004) 1–10. https://doi.org/https://doi.org/10.1016/S0955-2219(03)00129-8.

[3] R.A. Miller, Current status of thermal barrier coatings — An overview, Surf. Coatings Technol. 30 (1987) 1–11. https://doi.org/https://doi.org/10.1016/0257-8972(87)90003-X.

[4] A.G. Evans, D.R. Mumm, J.W. Hutchinson, G.H. Meier, F.S. Pettit, Mechanisms controlling the durability of thermal barrier coatings, Prog. Mater. Sci. 46 (2001) 505–553. https://doi.org/https://doi.org/10.1016/S0079-6425(00)00020-7.

[5] D. Hennings, Barium titanate based ceramic materials for dielectric use, Int. J. High Technol. Ceram. 3 (1987) 91–111. https://doi.org/https://doi.org/10.1016/0267-3762(87)90031-2.

[6] K.C. Kao, 4 - Ferroelectrics, Piezoelectrics, and Pyroelectrics, in: K.C. Kao (Ed.), Dielectr. Phenom. Solids, Academic Press, San Diego, 2004: pp. 213–282. https://doi.org/https://doi.org/10.1016/B978-012396561-5/50014-1.

[7] B. Malič, D. Kuščer, M. Vrabelj, J. Koruza, 5 - Review of methods for powder-based processing, in: B.D. Stojanovic (Ed.), Magn. Ferroelectr. Multiferroic Met. Oxides, Elsevier, 2018: pp. 95–120. https://doi.org/https://doi.org/10.1016/B978-0-12-811180-2.00005-0.

[8] D.R. Clarke, T.M. Shaw, D. Dimos, Issues in the Processing of Cuprate Ceramic Superconductors, J. Am. Ceram. Soc. 72 (1989) 1103–1113. https://doi.org/10.1111/j.1151-2916.1989.tb09691.x.

[9] J.G. Bednorz, K.A. Müller, Possible highTc superconductivity in the Ba−La−Cu−O system, Zeitschrift Für Phys. B Condens. Matter. 64 (1986) 189–193. https://doi.org/10.1007/BF01303701.

[10] R.O. Ritchie, The conflicts between strength and toughness, Nat. Mater. 10 (2011) 817–822. https://doi.org/10.1038/nmat3115.

[11] A.G. Evans, Perspective on the Development of High-Toughness Ceramics, J. Am. Ceram. Soc. 73 (1990) 187–206. https://doi.org/10.1111/j.1151-2916.1990.tb06493.x.

[12] R.C. GARVIE, R.H. HANNINK, R.T. PASCOE, Ceramic steel?, Nature. 258 (1975) 703–704. https://doi.org/10.1038/258703a0.

[13] E.P. Butler, Transformation-toughened zirconia ceramics, Mater. Sci. Technol. 1 (1985) 417–432. https://doi.org/10.1179/mst.1985.1.6.417.

[14] A.G. EVANS, A.H. HEUER, REVIEW—Transformation Toughening in Ceramics: Martensitic Transformations in Crack-Tip Stress Fields, J. Am. Ceram. Soc. 63 (1980) 241–248. https://doi.org/10.1111/j.1151-2916.1980.tb10712.x.

[15] J.S. Yang, X.M. Chen, T. Aizawa, M. Kuwabara, PZT based piezoelectric ceramics with enhanced fracture toughness, Solid State Ionics. 108 (1998) 117–121. https://doi.org/https://doi.org/10.1016/S0167-2738(98)00028-9.

[16] K. Xia, T.G. Langdon, The toughening and strengthening of ceramic materials through discontinuous reinforcement, J. Mater. Sci. 29 (1994) 5219–5231. https://doi.org/10.1007/BF01171532.

[17] P.F. Becher, Microstructural Design of Toughened Ceramics, J. Am. Ceram. Soc. 74 (1991) 255–269. https://doi.org/10.1111/j.1151-2916.1991.tb06872.x.

[18] R.W. Rice, Mechanisms of Toughening in Ceramic Matrix Composites, in: Proc. 5th Annu. Conf. Compos. Adv. Ceram. Mater. Ceram. Eng. Sci. Proc., John Wiley & Sons,

Ltd, 2008: pp. 661–701. https://doi.org/10.1002/9780470291092.ch20.

[19] B. Malic, M. Kosec, T. Kosmač, Mechanical and electric properties of PZT-ZrO2 composites, Ferroelectrics. 129 (1992) 147–155. https://doi.org/10.1080/00150199208016985.

[20] A. V Virkar, R.L.K. Matsumoto, Ferroelastic Domain Switching as a Toughening Mechanism in Tetragonal Zirconia, J. Am. Ceram. Soc. 69 (1986) C-224-C-226. https://doi.org/10.1111/j.1151-2916.1986.tb07341.x.

[21] A.G. Evans, D.R. Clarke, C.G. Levi, The influence of oxides on the performance of advanced gas turbines, J. Eur. Ceram. Soc. 28 (2008) 1405–1419. https://doi.org/https://doi.org/10.1016/j.jeurceramsoc.2007.12.023.

[22] A. Kolleck, G.A. Schneider, F.A. Meschke, R-Curve Behavior of BaTiO3 - and PZT Ceramics Under the Influence of an Electric Filed Applied Parallel to the Crack Front, Acta Mater. 48 (2000) 4099–4113. https://doi.org/10.1016/S1359-6454(00)00198-1.

[23] N. Orlovskaya, M. Lugovy, S. Pathak, D. Steinmetz, J. Lloyd, L. Fegely, M. Radovic, E.A. Payzant, E. Lara-Curzio, L.F. Allard, J. Kuebler, Thermal and mechanical properties of LaCoO3 and La0.8Ca0.2CoO3 perovskites, J. Power Sources. 182 (2008) 230–239. https://doi.org/10.1016/j.jpowsour.2008.03.072.

[24] C. Mercer, J.R.R. Williams, D.R.R. Clarke, a. G.G. Evans, On a ferroelastic mechanism governing the toughness of metastable tetragonal-prime (t′) yttria-stabilized zirconia, Proc. R. Soc. A Math. Phys. Eng. Sci. 463 (2007) 1393–1408. https://doi.org/10.1098/rspa.2007.1829.

[25] F. Meschke, A. Kolleck, G.A. Schneider, R-curve behaviour of BaTiO3 due to stress-induced ferroelastic domain switching, J. Eur. Ceram. Soc. 17 (1997) 1143–1149. https://doi.org/10.1016/s0955-2219(96)00211-7.

[26] K. Mehta, A. V. Virkar, Fracture Mechanisms in Ferroelectric-Ferroelastic Lead Zirconate Titanate (Zr: Ti=0.54:0.46) Ceramics, J. Am. Ceram. Soc. 73 (1990) 567–574. https://doi.org/10.1111/j.1151-2916.1990.tb06554.x.

[27] J.A. Krogstad, M. Lepple, C.G. Levi, Opportunities for improved TBC durability in the

CeO2-TiO2-ZrO2 system, Surf. Coatings Technol. 221 (2013) 44–52. https://doi.org/10.1016/j.surfcoat.2013.01.026.

[28] X.-K. Zhu, J.A. Joyce, Review of fracture toughness (G, K, J, CTOD, CTOA) testing and standardization, Eng. Fract. Mech. 85 (2012) 1–46. https://doi.org/https://doi.org/10.1016/j.engfracmech.2012.02.001.

[29] A.A. Griffith, G.I. Taylor, VI. The phenomena of rupture and flow in solids, Philos. Trans. R. Soc. London. Ser. A, Contain. Pap. a Math. or Phys. Character. 221 (1921) 163–198. https://doi.org/10.1098/rsta.1921.0006.

[30] G. Irwin, Analysis of stresses and strains near the end of a crack traversing a plate, J. Appl. Mech. 24 (1957) 361–64.

[31] J.R. Rice, A Path Independent Integral and the Approximate Analysis of Strain Concentration by Notches and Cracks, J. Appl. Mech. 35 (1968) 379–386. https://doi.org/10.1115/1.3601206.

[32] A. Wells, Application of fracture mechanics at and beyond general yielding, Br. Weld J. 10 (1963) 563–70.

[33] K. Aizu, Determination of the State Parameters and Formulation of Spontaneous Strain for Ferroelastics, J. Phys. Soc. Japan. 28 (1970) 706–716. https://doi.org/10.1143/JPSJ.28.706.

[34] V.K. Wadhawan, Ferroic materials: A primer, Resonance. 7 (2002) 15–24. https://doi.org/10.1007/BF02836749.

[35] V.K. Wadhawan, Ferroelasticity, Bull. Mater. Sci. 6 (1984) 733–753. https://doi.org/10.1007/BF02744001.

[36] K. Lee, S. Baik, Ferroelastic Domain Structure and Switching in Epitaxial Ferroelectric Thin Films, Annu. Rev. Mater. Res. 36 (2006) 81–116. https://doi.org/10.1146/annurev.matsci.36.090804.094613.

[37] C. Mercer, J.R. Williams, D.R. Clarke, a. G. Evans, On a ferroelastic mechanism governing the toughness of metastable tetragonal-prime (*t′*) yttria-stabilized zirconia, Proc.

R. Soc. A Math. Phys. Eng. Sci. 463 (2007) 1393–1408. https://doi.org/10.1098/rspa.2007.1829.

[38] G. Arlt, Twinning in ferroelectric and ferroelastic ceramics: stress relief, J. Mater. Sci. 25 (1990) 2655–2666. https://doi.org/10.1007/BF00584864.

[39] K. Kim, J.E. Huber, In situ observation of ferroelastic domain evolution in a near-morphotropic Pb(Zr,Ti)O3ceramic by piezoresponse force microscopy, J. Eur. Ceram. Soc. 35 (2015) 1459–1468. https://doi.org/10.1016/j.jeurceramsoc.2014.11.027.

[40] A.J.G. Lunt, M.Y. Xie, N. Baimpas, S.Y. Zhang, S. Kabra, J. Kelleher, T.K. Neo, A.M. Korsunsky, Calculations of single crystal elastic constants for yttria partially stabilised zirconia from powder diffraction data, J. Appl. Phys. 116 (2014) 1–9. https://doi.org/10.1063/1.4891714.

[41] J.J. Wang, F.Y. Meng, X.Q. Ma, M.X. Xu, L.Q. Chen, Lattice, elastic, polarization, and electrostrictive properties of BaTiO3 from first-principles, J. Appl. Phys. 108 (2010) 34107. https://doi.org/10.1063/1.3462441.

[42] H. Cao, a G. Evans, Nonlinear deformation of ferroelectric ceramics, J. Am. Ceram. Soc. 76 (1993) 890–896. https://doi.org/10.1111/j.1151-2916.1993.tb05312.x.

[43] C.M. Landis, Erratum: On the fracture toughness of ferroelastic materials (Journal of the Mechanics and Physics of Solids (2003) 51 (1347-1369)), J. Mech. Phys. Solids. 52 (2004) 497–498. https://doi.org/10.1016/S0022-5096(03)00089-9.

[44] C.M. Landis, On the fracture toughness of ferroelastic materials, J. Mech. Phys. Solids. 51 (2003) 1347–1369. https://doi.org/https://doi.org/10.1016/S0022-5096(03)00065-6.

[45] J.L. Jones, E.B. Slamovich, K.J. Bowman, Domain texture distributions in tetragonal lead zirconate titanate by x-ray and neutron diffraction, J. Appl. Phys. 97 (2005). https://doi.org/10.1063/1.1849821.

[46] J.L. Jones, M. Hoffman, R-curve and stress-strain behavior of ferroelastic ceramics, J. Am. Ceram. Soc. 89 (2006) 3721–3727. https://doi.org/10.1111/j.1551-2916.2006.01300.x.

[47] W.S. Kreher, Influence of domain switching zones on the fracture toughness of ferroelectrics, J. Mech. Phys. Solids. 50 (2002) 1029–1050. https://doi.org/https://doi.org/10.1016/S0022-5096(01)00110-7.

[48] K.M. Prettyman, J.F. Jue, A. V Virkar, C.R. Hubbard, O.B. Cavin, M.K. Ferber, Hysteresity effects in 3 mol% yttria-doped zirconia (t'-phase), J. Mater. Sci. 27 (1992) 4167–4174. https://doi.org/10.1007/BF01105121.

[49] M. V Swain, R.H.J. Hannink, R-curve behavior in zirconia ceramics, American Ceramic Society, Inc, United States, 1983. http://inis.iaea.org/search/search.aspx?orig_q=RN:17050039.

[50] G. Rauchs, T. Fett, D. Munz, R-curve behaviour of 9Ce-TZP zirconia ceramics, Eng. Fract. Mech. 69 (2002) 389–401. https://doi.org/https://doi.org/10.1016/S0013-7944(01)00073-X.

[51] G. Gogotsi, V. Galenko, B. Ozerskii, N. Orlovskaya, the Mechanical Behavior of Lanthanum Cobaltite-Based At Different Temperatures, Refract. Ind. Ceram. 42 (2001) 341–346.

[52] W. Araki, J. Malzbender, Ferroelastic deformation of La0.58Sr0.4Co0.2Fe0.8O3-δ under uniaxial compressive loading, J. Eur. Ceram. Soc. 33 (2013) 805–812. https://doi.org/10.1016/j.jeurceramsoc.2012.10.035.

[53] T.L. Baker, K.T. Faber, D.W. Readey, Ferroelastic Toughening in Bismuth Vanadate, J. Am. Ceram. Soc. 74 (1991) 1619–1623. https://doi.org/10.1111/j.1151-2916.1991.tb07148.x.

[54] D.A. Hall, A. Steuwer, B. Cherdhirunkorn, P.J. Withers, T. Mori, Micromechanics of domain switching in rhombohedral PZT ceramics, Ceram. Int. 34 (2008) 679–683. https://doi.org/10.1016/J.CERAMINT.2007.09.001.

[55] J.E. Daniels, J.L. Jones, T.R. Finlayson, Characterization of domain structures from diffraction profiles in tetragonal ferroelastic ceramics, J. Phys. D. Appl. Phys. 39 (2006) 5294–5299. https://doi.org/10.1088/0022-3727/39/24/029.

[56] D. Baither, B. Baufeld, U. Messerschmidt, A.H. Foitzik, M. Rühle, Ferroelasticity of t'-

Zirconia: I, High-Voltage Electron Microscopy Studies of the Microstructure in Polydomain Tetragonal Zirconia, J. Am. Ceram. Soc. 80 (1997) 1691–1698. https://doi.org/10.1111/j.1151-2916.1997.tb03040.x.

[57] B. Baufeld, D. Baither, U. Messerschmidt, M. Bartsch, A.H. Foitzik, M. Rühle, Ferroelasticity of t‘-Zirconia: II, In situ Straining in a High-Voltage Electron Microscope, J. Am. Ceram. Soc. 80 (1997) 1699–1705. https://doi.org/10.1111/j.1151-2916.1997.tb03041.x.

[58] D. Baither, M. Bartsch, B. Baufeld, A. Tikhonovsky, A. Foitzik, M. Rühle, U. Messerschmidt, Ferroelastic and Plastic Deformation of t′-Zirconia Single Crystals, J. Am. Ceram. Soc. 84 (2001) 1755–1762. https://doi.org/10.1111/j.1151-2916.2001.tb00911.x.

[59] P. Gao, J. Britson, C.T. Nelson, J.R. Jokisaari, C. Duan, M. Trassin, S.H. Baek, H. Guo, L. Li, Y. Wang, Y.H. Chu, A.M. Minor, C.B. Eom, R. Ramesh, L.Q. Chen, X. Pan, Ferroelastic domain switching dynamics under electrical and mechanical excitations, Nat. Commun. 5 (2014) 1–8. https://doi.org/10.1038/ncomms4801.

[60] T. Sluka, K.G. Webber, E. Colla, D. Damjanovic, Phase field simulations of ferroelastic toughening: The influence of phase boundaries and domain structures, Acta Mater. 60 (2012) 5172–5181. https://doi.org/10.1016/j.actamat.2012.06.023.

[61] J. Sheng, C.M. Landis, Toughening due to domain switching in single crystal ferroelectric materials, Int. J. Fract. 143 (2007) 161–175. https://doi.org/10.1007/s10704-007-9056-7.

[62] C.M. Landis, On the Strain Saturation Conditions for Polycrystalline Ferroelastic Materials , J. Appl. Mech. 70 (2003) 470–478. https://doi.org/10.1115/1.1600472.

[63] U. Messerschmidt, D. Baither, B. Baufeld, M. Bartsch, Plastic deformation of zirconia single crystals: A review, Mater. Sci. Eng. A. 233 (1997) 61–74. https://doi.org/10.1016/s0921-5093(97)00050-6.

[64] N. Zhang, M. Asle Zaeem, Effects of specimen size and yttria concentration on mechanical properties of single crystalline yttria-stabilized tetragonal zirconia nanopillars, J. Appl. Phys. 122 (2017). https://doi.org/10.1063/1.4991339.

[65] N. Balasubramanian, T.G. Langdon, Comment on the role of intragranular dislocations in

superplastic yttria-stabilized zirconia, Scr. Mater. 48 (2003) 599–604. https://doi.org/https://doi.org/10.1016/S1359-6462(02)00471-2.

[66] E. Camposilvan, M. Anglada, Size and plasticity effects in zirconia micropillars compression, Acta Mater. 103 (2016) 882–892. https://doi.org/10.1016/j.actamat.2015.10.047.

[67] N. Zhang, M. [Asle Zaeem], Competing mechanisms between dislocation and phase transformation in plastic deformation of single crystalline yttria-stabilized tetragonal zirconia nanopillars, Acta Mater. 120 (2016) 337–347. https://doi.org/https://doi.org/10.1016/j.actamat.2016.08.075.

[68] X.M. Zeng, Z. Du, N. Tamura, Q. Liu, C.A. Schuh, C.L. Gan, In-situ studies on martensitic transformation and high-temperature shape memory in small volume zirconia, Acta Mater. 134 (2017) 257–266. https://doi.org/10.1016/j.actamat.2017.06.006.

[69] X.M. Zeng, A. Lai, C.L. Gan, C.A. Schuh, Crystal orientation dependence of the stress-induced martensitic transformation in zirconia-based shape memory ceramics, Acta Mater. 116 (2016) 124–135. https://doi.org/10.1016/j.actamat.2016.06.030.

[70] T.K. Gupta, J.H. Bechtold, R.C. Kuznicki, L.H. Cadoff, B.R. Rossing, Stabilization of tetragonal phase in polycrystalline zirconia, J. Mater. Sci. 12 (1977) 2421–2426. https://doi.org/10.1007/BF00553928.

[71] A.G. Evans, N. Burlingame, M. Drory, W.M. Kriven, Martensitic transformations in zirconia—particle size effects and toughening, Acta Metall. 29 (1981) 447–456. https://doi.org/https://doi.org/10.1016/0001-6160(81)90170-X.

[72] T. Höche, M. Deckwerth, C. Rüssel, Partial Stabilization of Tetragonal Zirconia in Oxynitride Glass-Ceramics, J. Am. Ceram. Soc. 81 (1998) 2029–2036. https://doi.org/10.1111/j.1151-2916.1998.tb02584.x.

[73] S. Tsunekawa, S. Ito, Y. Kawazoe, J.-T. Wang, Critical Size of the Phase Transition from Cubic to Tetragonal in Pure Zirconia Nanoparticles, Nano Lett. 3 (2003) 871–875. https://doi.org/10.1021/nl034129t.

CHAPTER 2

EXPERIMENTAL METHODS

This chapter outlines the experimental methods and techniques used in this dissertation to study the behavior of ferroelastic ceramics. It also outlines techniques that were developed and used during the process of carrying out this research that are not directly discussed in the results in the following chapters but may be valuable for future studies. Therefore, some preliminary results associated with several of the methods will also be briefly discussed in this chapter. This section will begin with a discussion of the synthesis and processing of ceramic materials. Electron backscatter diffraction techniques used for microstructural analysis will then be outlined, followed by discussion of techniques used for deforming ferroelastic single crystals and polycrystals.

2.1 Ceramic Synthesis

There are many techniques that may be used to synthesize ceramics with a wide range of compositions. Here, synthesis techniques used for fabrication of materials used in this dissertation will be discussed. This discussion primarily focuses on liquid solution-based synthesis techniques.

2.1.1 Ceria-Titania-Zirconia (CTZ) Synthesis

Throughout this dissertation, the primary ferroelastic ceramic of interest is a zirconia-based (ZrO_2) material stabilized into the tetragonal phase with 10 mol% ceria (CeO_2) and 10mol% titania (TiO_2). The molar ratios of the various components can be changed to alter the phase stability of the material [1], but the $10CeO_2$-$10TiO_2$-$80CZrO_2$ composition will be discussed here since the tetragonal phase of interest is stable with these molar ratios. A schematic phase diagram adapted from Krogstad et al. is shown in Figure 2.1, which shows the composition used here sitting within the tetragonal phase field [1]. This material will be referred to as CTZ. This material was prepared using a liquid solution processing technique called reverse coprecipitation. This technique, pioneered by Mayo for fabrication of nanopowders, allows for synthesis of relatively large quantities of nanopowders that can then be used to process bulk samples with finer control of the resulting microstructure [2]. This synthesis technique is not limited to CTZ and has been used to synthesize other ceramics as well, but the focus here will be on the process used for CTZ nanopowder synthesis.

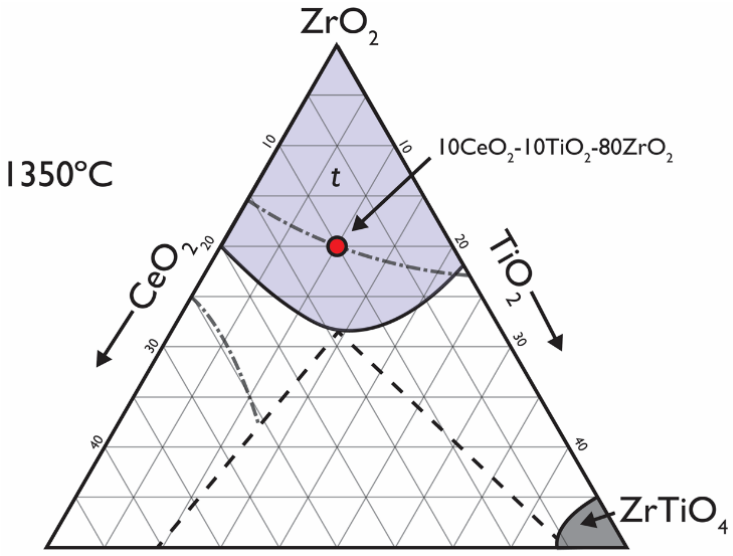

Figure 2.1: Partial schematic phase diagram or CTZ adapted from Krogstad [1] showing the $10CeO_2$-$10TiO_2$-$80CZrO_2$ composition used for this study.

To synthesize nanopowders of CTZ, precursors containing the three cations of interest were dissolved into solution in the correct stoichiometry. Synthesis ideally should be done without the use of water since water is known to contribute to undesirable agglomeration of zirconia nanopowders. Therefore, precursors that are all soluble in ethanol were selected (although a variety of alternative precursors with appropriate solubility can be used). The cerium precursor was cerium nitrate hexahydrate ($Ce(NO_3)_3•6H_2O$), the titanium precursor was titanium isopropoxide ($C_{12}H_{28}O_4Ti$), and the zirconium precursor was zirconium n-butoxide ($C_{16}H_{36}O_4Zr$).

In order to achieve the correct molar ratios of cations in the final oxide, the precursors all were calibrated to determine the molar yield of cations from a given mass of the precursors. This was particularly important since these precursors are hygroscopic and may accumulate water weight over time that decreases the cation yield for a given mass of precursor. This calibration was done using the same precipitation, drying, and calcination procedure that will be outlined shortly, but was done separately for each cation precursor. The mass of the resulting oxide was weighed and used to determine how many moles of the cation were produced using the initial mass of each precursor. It is important to note that the oxygen stoichiometry of the resulting oxides must be known in order to accurately calculate the moles of cation present from the oxide mass.

Once each of the precursors were calibrated, they were weighed and the mass of each that were needed to achieve the desired moles of cations in the final powder was dissolved into ethanol. This dissolution was done separately for each precursor to ensure that they were completely dissolved before mixing. The three precursor solutions were then slowly mixed together and added to a separatory funnel. This separatory funnel was placed above a large beaker containing ammonium hydroxide (NH_4OH) solution, and the precursor solution was slowly dripped into the ammonium hydroxide while constantly stirring. Metal hydroxides ($Ce(OH)_4$, $Ti(OH)_4$, and $Zr(OH)_4$) immediately precipitated. The pH of the solution was checked throughout the precipitation process and maintained above 10.5, since higher pH results in faster precipitation and reduced particle size [3].

Once the precipitation of hydroxide powders was finished, the powders may be separated from the liquid by filtration or centrifuging. The method used for CTZ synthesis in this dissertation was centrifuging. Once the powders were separated from the liquid, they were washed twice with 200 proof ethanol. It was important to resuspend and mix the powders well within the ethanol to ensure that the entire volume of powder is well washed. The powders were then centrifuged out of the ethanol again (repeated twice, once for each ethanol wash). After washing, the powders were dried in a drying oven at 80°C for at least 12 hours until completely dry. The powders were then finely ground in an agate mortar and pestle before calcining in air at 600°C for 4 hours. The powders were then be composed of the desired oxide and contain only the tetragonal phase of interest, which was confirmed using x-ray diffraction. Powders were then compacted using dry pressing and sintered using conventional sintering techniques that will be described in section 2.2. The microstructure that resulted from ranges of processing parameters used with these powders will also be described in detail in later chapters of this document.

2.1.2 Barium Titanate (BTO) Synthesis

Barium titanate ($BaTiO_3$ or BTO) is a very common ceramic material used in a variety of applications. It is commonly used as a dielectric in capacitors due to its high dielectric constant and is also often used as a piezoelectric material [4]. The tetragonal phase is ferroelectric and also exhibits a ferroelastic response [5,6]. Here, barium titanate was synthesized as a ferroelastic material, however, results of mechanical tests done on BTO will not be directly discussed in the

following chapters of this document. Nevertheless, BTO synthesis and microstructures will be briefly outlined here.

Barium titanate was synthesized here using the organic-steric entrapment synthesis according to Kriven [7]. This synthesis route can utilize a variety of organics such as polyvinyl alcohol, ethylene glycol, and polyethylene glycol to interact with dissolved cations in solution to homogeneously distribute the cations on the nanoscale. Here, ethylene glycol was used to synthesize the barium titanate following Lee [8]. For this synthesis Barium nitrate ($Ba(NO_3)_2$) and titanium isopropoxide ($C_{12}H_{28}O_4Ti$) were dissolved into liquid ethylene glycol (EG) in a molar ratio of 1:4 moles of cations to moles of EG. This mixture was dried and then calcined at 600°C. The powders were then pressed into pellets and sintered at 1200°C and 1350°C.

The microstructures that resulted from sintering at 1200°C were highly porous as can be seen in Figure 2.2(d). Sintering at 1350°C resulted in increased density, however, samples showed abnormal grain growth. Some grains increased in size up to millimeter scale and sometimes grew across the entire thickness of the pellet, while other grains remained much smaller (on the order of tens of microns). The samples with abnormal grain growth also exhibited unusual grain shapes, with cavities present on the surface of many grains. Other samples contained spherical bubbles throughout the cross section which could indicate liquid or gas phase evolution during sintering. Examples of these microstructures can be seen in Figure 2.2. Furthermore, a mixture of the tetragonal barium titanate phase as well as the orthorhombic orthotitantate phase were sometimes observed in x-ray diffraction patterns after sintering.

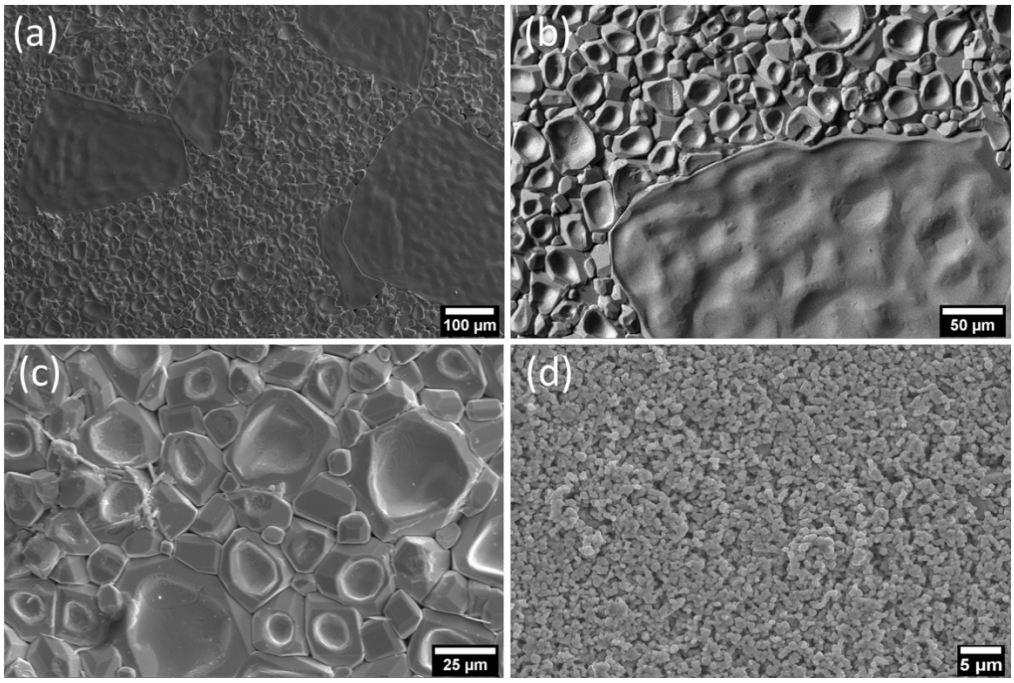

Figure 2.2: (a-c) SEM images of BTO sintered at 1350°C that show abnormal grain growth. (a) Several large grains embedded in a much finer grained matrix are visible. (b) The surface of a large grain interfacing many smaller grains shows that the surface of the large grain is rough but is smoother than the cratered surface of the smaller grains. (c) The morphology of the smaller BTO grains shows that some are faceted while most exhibit a concavity on the surface, that often takes up much of the grain surface. (d) BTO sintered at 1200°C showing high porosity and incomplete sintering.

2.1.3 Lanthanum Cobalt Oxide (LCO) Synthesis

Not only tetragonal ferroelastics can be synthesized. Other structures, such as rhombohedral perovskites also can exhibit ferroelasticity. Lanthanum cobaltite ($LaCoO_3$ or LCO) based ceramics have this rhombohedral perovskite structure and exhibit a ferroelastic response [9,10]. This material is often doped with other cations such as strontium or calcium in order to modify its electrical and optical properties [11], and is useful in applications such as lasers, solid oxide fuel cells, oxygen separation membranes, and catalysts [12–15]. Here, LCO was synthesized as a ferroelastic material, however, it was not used in any of the subsequent mechanical evaluations. Nevertheless, its synthesis and resulting microstructure will also be briefly outlined here.

Lanthanum cobalt oxide perovskite was synthesized according to the process outlined by Chen [16]. In this procedure, equimolar ratios of lanthanum nitrate hexahydrate ($La(NO_3)_3 \cdot 6H_2O$)

and cobalt nitrate hexahydrate ($Co(NO_3)_3 \cdot 6H_2O$), both having been calibrated for cation yield, were dissolved into water. This solution was then mixed with three times the molar ratio of ethylenediaminetetraacetic acid (EDTA) which was dissolved in water and ammonia. The mixture of these solutions was heated on a hot plate until viscous then dried and ground. The dried gel/powder was then calcined at 900°C in air for 16 hours. These oxidized powders were then pressed into pellets and sintered at 1200°C for 2 hours.

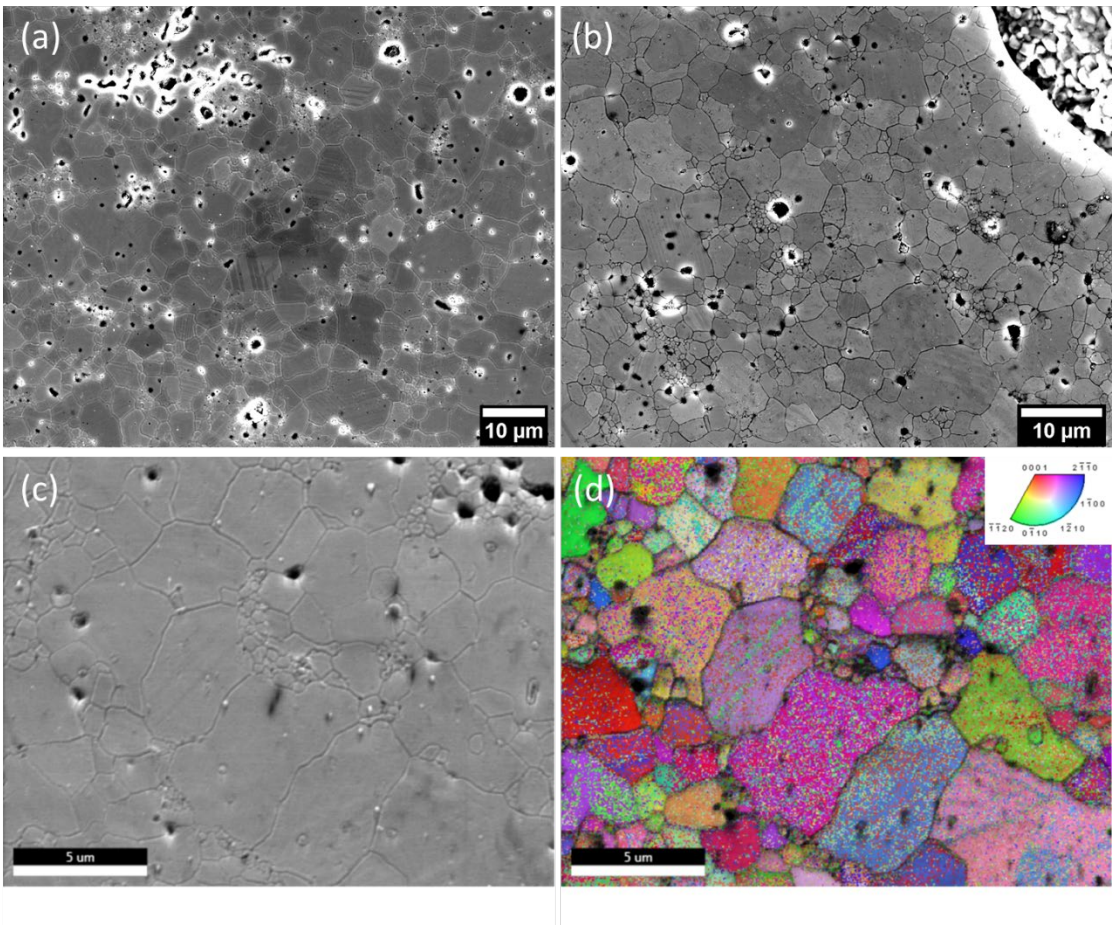

Figure 2.3: (a) Scanning electron micrograph of LCO after sintering where many grains contain twins. (b) Scanning electron micrograph of LCO after sintering where fewer grains contain twins. A large area of porosity is also visible in the upper right corner of the image. (c,d) Image and corresponding inverse pole figure orientation plot collected using electron backscatter diffraction indexed to a rhombohedral lanthanum cobalt oxide phase. Residual porosity is visible in all images.

The synthesis resulted in a heterogeneous microstructure. Some regions were heavily twinned as can be seen by close inspection of Figure 2.3(a), while other regions contained significantly fewer twins, as seen in Figure 2.3(b). The microstructure may have been a result of

heterogeneous chemistry throughout the samples. The grain size distribution was also bimodal, with some grains growing much larger than others during sintering, and there was significant residual porosity in some regions of the pellets. It is interesting to note that the smaller grains tended to be clustered. EBSD was also performed on LCO samples. Figure 2.3 shows a region from which EBSD was collected in (c) and the corresponding orientation map in (d). The indexing rate was very high (99.09%), however, there was clear misindexing, as evidenced by may grains containing roughly equal, random, distributions of several orientations, due to pseudosymmetry and other sources of error, which will be discussed in detail in section 2.3.

2.2 Ceramic Processing

There are many ways to form and process ceramics. Specific techniques are often chosen to achieve a desired final form and microstructure. For instance, if the final goal is to create a ceramic film for use as a capacitor sheet, tape casting followed by debinding and sintering may be used [17]. Whereas to create a high temperature thermal barrier coating, plasma spraying may be a more useful technique. Controlling microstructure through processing was highly important for this research since evaluating the influence of microstructure on the ferroelastic response in materials was a key aim for the projects discussed in this dissertation. In this section, the specific processing routes used to create dense, monolithic ceramic bodies, while having control over the grain size will be discussed.

2.2.1 Conventional Ceramic Processing

Typically, ceramic processing follows the following steps: synthesis of powders, mixing (may involve binders, plasticizers, or other additives), forming, drying (may include debinding), and sintering. The final microstructure that is achieved relies on the starting materials used as well as the specific processing parameters that are employed. In this section, the conventional processing techniques to fabricate samples in this dissertation are outlined. This focuses primarily on dry pressing and conventional sintering methods.

The method used to consolidate powders into green body (not yet sintered) pellets was dry pressing. This forming method relies on applying pressure to the powder while confined inside a cylindrical die. While the addition of lubricants to decrease friction within the dies, and binders such as PVA along with plasticizers such as water or stearic acid is common for increasing the

strength of green bodies, they were not used here. This was mostly because the nanoscale size of the powders being pressed here lead to good compaction of the powders even without binders. However, there are several flaws that commonly occurred due to friction and heterogeneous stress distribution in the pellets during compaction. Possible flaws include vertical cracking, ring capping, end capping, and delamination. Schematics of these flaws can be seen in Figure 2.4.

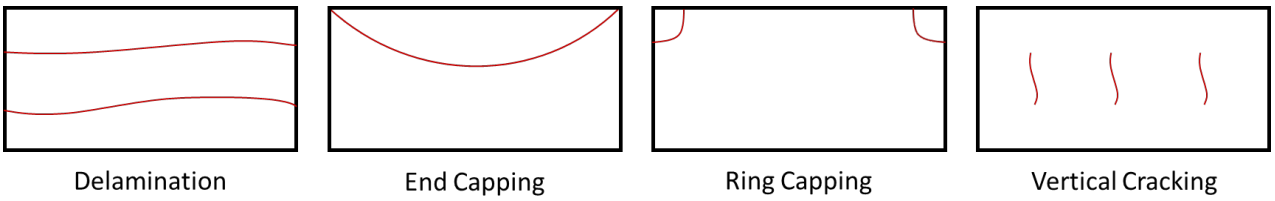

Figure 2.4: Schematics of flaws that form during compaction of dry powders including delamination, end capping, ring capping and vertical cracking.

Pellets pressed in this way were then densified using conventional sintering techniques. Conventional sintering has driving forces and mechanisms associated with it. The driving force for sintering is the powder body decreasing its total energy. The powders have high surface energy in the green body state. Sintering enables the reduction of surface area and surface curvature which reduces the overall energy of the pellet. The mechanism though which this densification occurs is solid state diffusion. By applying heat to the compacted powder body, the mobility and diffusivity of the atoms/ions in the particles is greatly increased, and diffusion enables the compacted powder to transform into a dense polycrystalline pellet with mostly planar grain boundaries. The drawback of this conventional sintering process, however, is that during densification, coarsening of the microstructure also occurs, causing the grains (and often pores) in the final microstructure to grow significantly compared to the crystal size in the initial powder. Furthermore, depending on the shape of pores that form, stable pores can be left within the microstructure that cannot be completely removed using conventional pressureless sintering. Grain growth was an advantage for several aspects of this study, as discussed in later chapters, however, maintaining a small grain size is also valuable in many instances and is difficult to achieve using conventional sintering techniques.

2.2.2 Spark Plasma Sintering

Conventional ceramic processing methods have limitations. For instance, sintering ceramic bodies often takes long periods of time (hours to days) and high temperatures, which leads to high

energy consumption. It is also difficult or impossible to achieve high densities while maintaining nanoscale microstructural features using conventional processing. Spark plasma sintering (SPS) is an alternative processing route that has generated significant interest in the past few decades for its ability to process dense, bulk nanostructured materials [18,19]. Conventional sintering techniques typically rely on external application of heat to compacted powder samples to form a densified body. SPS achieves densification through the application of mechanical pressure to the material while rapidly heating the sample directly using high electric currents. A schematic of an SPS machine with the range of parameters available for processing in this work is shown in Figure 2.5. The model used in this research is the Fuji SPS-615 Dr. Sinter.

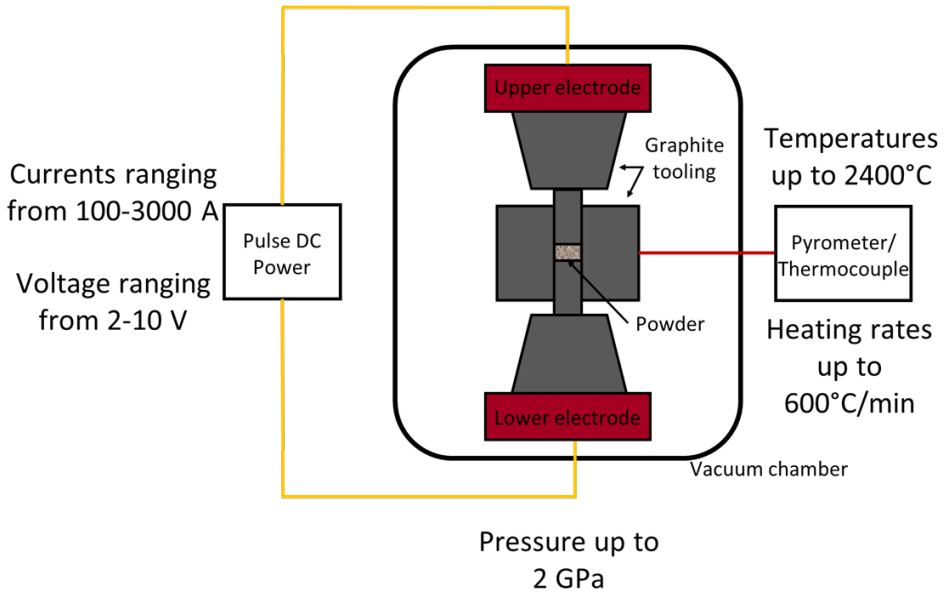

Figure 2.5: Schematic of a spark plasma sintering machine. The values shown for parameters including voltage, current, pressure and temperature are given for the range of parameters used in this research.

However, there currently exists little discussion of the variability in properties (including physical and electrical properties) achieved by processing ceramic materials using SPS. Furthermore, there is no consensus on the mechanisms that may be responsible for densification of various materials during SPS. Sometimes, this incomplete understanding of SPS results in unpredictable and undesirable behavior in sintered samples. For this reason, SPS was not used in processing ferroelastic samples used for the mechanical characterizations discussed in later chapters of this dissertation. Rather, studies using SPS were specifically designed to evaluate the variability within and between samples prepared by SPS and will be discussed separately in

Chapter 5. Furthermore, many smaller research projects that will not be directly discussed in the results presented in this document were performed using SPS during the course of the research associated with this dissertation. Therefore, this section will outline the procedures used and developed to process a variety of materials using the SPS technique.

Most SPS samples were prepared using cylindrical graphite dies with inner diameters of 20 or 20.5mm. 20mm dies were primarily used for low temperature sintering (<1000°C) when the sample reacting with the die is limited. During low temperature sintering, boron nitride spray was applied to the punches prior to sintering as a release agent. 20.5mm dies were used for higher temperature sintering (>1000°C). During high temperature sintering graphite foil was wrapped around the sample and the punches to prevent the sample reacting with the die, thus the extra 0.5mm diameter is needed for the foil layer to snugly fit between the punches and inner die wall. Graphite foil disks were also used between the sample and punches to ensure a clean release. When sintering was done below 1000°C, a K-type thermocouple was placed into a small hole in the die wall to monitor and control temperature. When sintering was done above 1000°C, temperature was monitored and controlled using an optical pyrometer. These dies were used to sinter materials including nickel, nickel chromium, aluminum, titanium-silicon carbide composites, alumina, yttria stabilized zirconia, tungsten, and tungsten-transition metal carbide composites. Typically, materials were sintered with temperatures ranging from 500°C-1800°C and applied pressures of 10-60MPa using these standard graphite dies. When sintering using temperatures below approximately 1400°C, the chamber was held under vacuum, while for higher temperature sintering, inert argon gas was used to fill the chamber to slightly below atmospheric pressure. Sintering was nearly always performed using automatic programs to control the temperature and applied pressure to ensure as much consistency between samples as possible.

One way to improve the density of samples produced by SPS while maintaining very fine grain size is to greatly increase the applied pressure while sintering, while applying relatively moderate to low temperatures. Maintaining fine grain sizes has been used by other researchers to fabricate bulk transparent ceramics, as well as ceramics with vastly increased hardness. Recently, a high pressure deformable punch SPS (DP-SPS) technique has been introduced by Muche et al. to process transparent samples with sub 10nm grain sizes and very high hardness [20]. In the research discussed here, this high pressure SPS technique was used to fabricate samples with

several compositions in order to maintain fine grain sizes and avoid thermal degradation of certain phases. To reach pressures up to 2 GPa, a modified die setup was needed. This die setup consisted of a graphite inner die with 5mm inner diameter. The inner die had punches made of cemented tungsten carbide (WC) that were finely polished before sintering. This inner die is placed into a large graphite outer die, in which a series of medium sized and large sized punches are used to increase the pressure applied to the innermost WC punches. Details about this setup can be found in the supplemental information provided in Muche et al. [20]. The only difference in the die configuration used in this work is that the silicon carbide spacers were replaced with additional tungsten carbide spacers.

This high pressure SPS die configuration was used to process materials including alumina, tungsten, and CTZ. Since the thermal mass of this die setup was larger than the standard graphite dies, automatic control programs were not suited for accurately controlling the heating when this die was used. Therefore, manual monitoring and control of the temperature and pressure was used. This also helped prevent catastrophic failure of the die since any misalignment of the punches resulted in dies fracturing at moderate applied loads. Preliminary samples prepared using this method ranged in quality, with many fracturing upon removal from the die due to residual stresses or incomplete sintering. For instance, CTZ powder was sintered using 500MPa applied pressure and a maximum temperature of 700°C held for 0 minutes. Upon removal from the die, the sample was significantly reduced (indicated by blackening of the material) and fractured into many pieces. The fractured pieces contained density gradients that can be seen in Figure 2.6. Some regions exhibited significant porosity as shown in Figure 2.6(c), while other areas were much denser as seen in Figure 2.6(d). Despite the failure of this sample, it did remain nanocrystalline with approximately 60-80nm grains. Because of this technique's current inability to effectively densify CTZ into bulk samples, it was not used to produce any samples for mechanical testing.

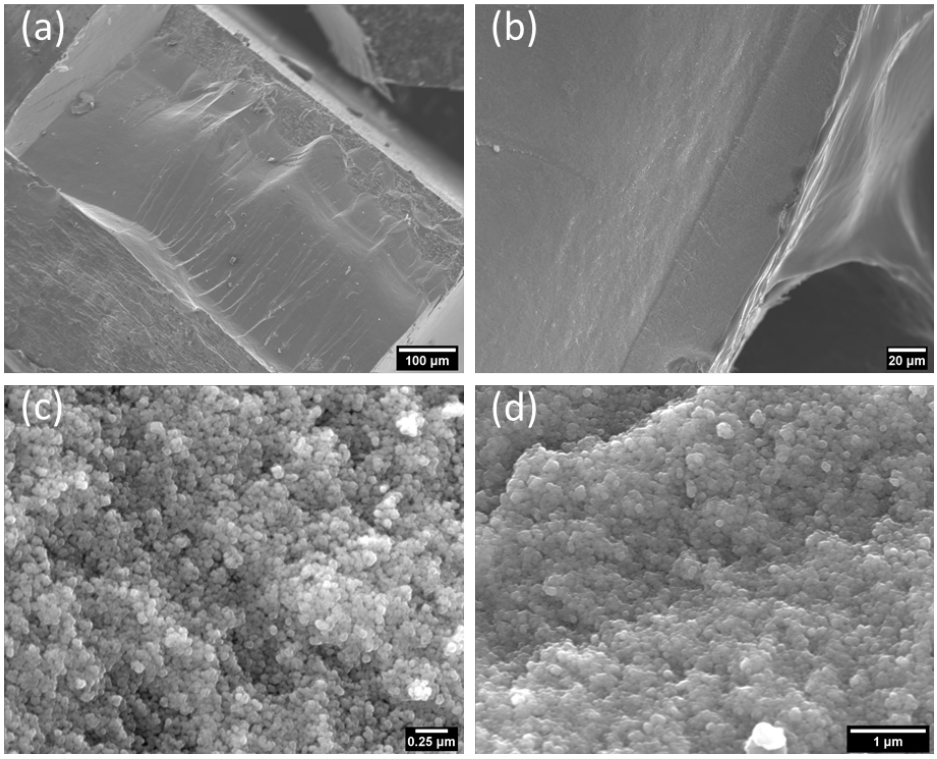

Figure 2.6: (a,b) Fracture surfaces showing the cross-section of a CTZ pellet prepared using high pressure SPS. Gradients in color are caused by gradients in densification throughout the sample. (c,d) Images of a less dense and more-dense region of the pellet respectively.

2.3 Electron Backscatter Diffraction

Electron backscatter diffraction (EBSD) is a technique used primarily for determining the orientation of crystals using a scanning electron microscope (SEM). EBSD can also be used for other applications such as phase mapping, measuring strain in crystals, and measurement of grain boundary character. In this dissertation it has been used to determine the orientation of singe crystal pillars, as well as for determining orientations of crystals in polycrystalline microstructures. In this section, the fundamentals of how EBSD works, and how orientation is currently determined using the diffraction patterns will be outlined.

EBSD works using a type of diffraction called Kikuchi diffraction, which involves electrons going through a sequence of scattering/diffraction events. During Kikuchi diffraction, electrons from the electron beam source first undergo incoherent scattering events within the material being imaged, which results in diffusely scattered electrons travelling in all directions (although mostly backward for thick samples, thus most are backscattered). This diffuse cloud of

electrons contains electrons with ranges of energies since the initial incoherent scattering event may be elastic or inelastic, however, the majority of EBSD signals come from electrons that have lost little energy. In crystalline materials, these diffusely scattered electrons may then be Bragg diffracted. Since electrons are incident on the atomic planes from all directions they diffract as two cones at the Bragg angle to the crystal planes. These cones are called Kossel cones and are emitted from the sample surface to create diffraction patterns unique to the crystal they are emitted from, with each pair of cones corresponding to a particular crystallographic plane [21]. The orientation of these cones depends on the orientation of the crystal forming the diffraction pattern, meaning they can be used to determine the crystallographic orientation of the area they are emitted from [22–24]. A schematic of Kossel cones diffracting from a crystal plane is shown in Figure 2.7.

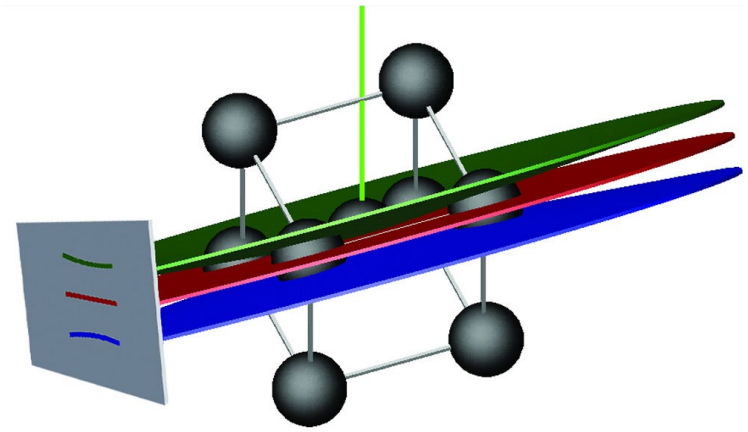

Figure 2.7: Schematic showing cones of diffracted electrons generated by Bragg diffraction off of a particular crystallographic plane. As the crystal rotates, the orientation of the cones changes with it [25].

In order to image these diffraction patterns, EBSD detectors are inserted near the samples emitting the diffracted electrons. These detectors consist of a phosphor screen that fluoresces when the diffracted electrons hit it, and a high-speed digital camera that images the phosphor screen. Pairs of Kossel cones incident on the phosphor screen appear as bright bands that correspond to crystallographic planes, many of which will intersect on the detector screen, as can be seen in Figure 2.8 which shows an Kikuchi pattern and an overlaid indexing solution for tetragonal zirconia.

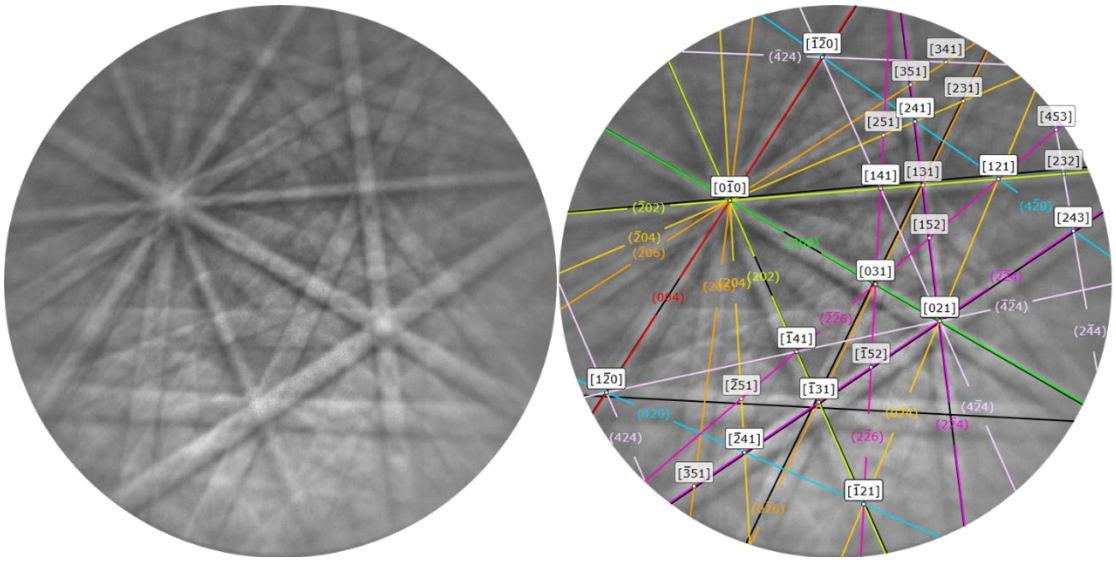

Figure 2.8: EBSD diffraction patterns of tetragonal CTZ. The left is the diffraction pattern after subtracting a background, and the right shows the indexing solution overlaid on the Kikuchi bands.

The width of the bands depends on the interplanar spacing for the given plane, while the angle between the bands corresponds to the angle between planes in the crystal. As the incident electron beam scans across the sample, the Kikuchi diffraction patterns are collected and correlated to the location they have been emitted from at the sample surface. The orientation of the crystal at specific locations where the diffraction patterns have been emitted from can then be determined by indexing the diffraction patterns using the band widths and angles. This indexing can be done in several different ways and is very sensitive the geometry of the sample and EBSD detector. Specification of sample and detector geometries will not be discussed in detail here, but several examples of how the diffraction patterns are indexed to determine orientation will be discussed in the following sections.

2.3.1 Current Indexing Methods and Limitations

In order to determine the orientation of the crystals in the sample, the geometry of the Kikuchi bands must be determined and correlated to known geometries of a crystal structure that is being indexed. Most software currently available that are used to index EBSD patterns rely on a feature extraction technique called a Hough transform to identify Kikuchi bands. Once the bands are identified, their widths and angles must be measured and matched against known structures [22,26].

The full image of a Kikuchi diffraction pattern is complex and contains a large amount of information. Indexing the diffraction patterns very rapidly in an automated fashion relies on an analysis computer identifying Kikuchi bands. This is necessary so that data collection can be done in a reasonable amount of time since many thousands of patterns are collected during orientation mapping. To identify bands on a noisy background, Hough transforms (or more generally, Radon transforms) are used. The Hough transform converts lines in a coordinate system (x,y) to points in Hough space (ρ,θ) through the relation:

$$\rho = x\cos\theta + y\sin\theta \qquad \text{Equation 2.1}$$

where ρ is the perpendicular distance from the line to the origin and θ is the angle of the line with respect to the x-axis. This relationship is shown schematically in Figure 2.9.

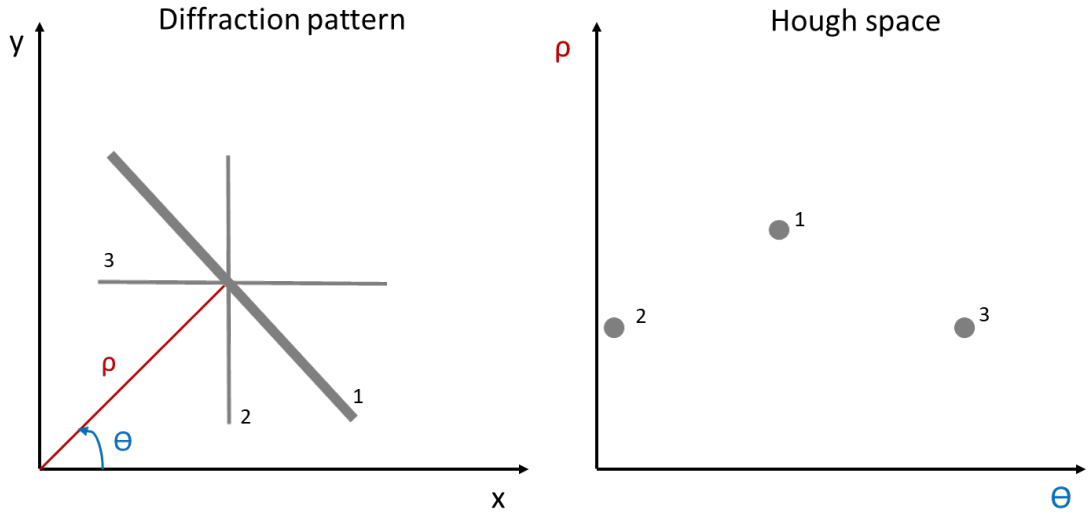

Figure 2.9: Schematic showing how a Hough transform converts Kikuchi lines in a diffraction pattern to points in Hough space. Each line in the (x,y) coordinate system corresponds to a point in Hough space depending on its perpendicular distance, ρ, from the origin and the angle, θ, form the x-axis.

The Hough peaks are then identified and used to determine a series of angles between Kikuchi bands which are compared to known angles between planes for a given crystal structure. This is done for a number of bands (for most software 4-8 bands is ideal) in the Kikuchi pattern, and is used to determine the crystal orientation.

This method of indexing is very useful due to its very fast data processing speeds. However, Hough based indexing discards most of the information contained in each diffraction pattern. This

means that there is opportunity for artifacts in the data to cause errors in indexing, and also means that a lot of the information about the material being analyzed is lost. In low symmetry materials, there is a more continuous spectrum of angles between planes, which means that indexing to a low number of bands has a higher probability of matching to an incorrect orientation solution. For higher symmetry materials, some orientations that are crystallographically distinct become impossible to differentiate using the Hough transform, leading to systematic misindexing of certain orientations. This error is known as pseudosymmetry. Tetragonal crystal structures such as tetragonal zirconia have been difficult to index reliably due to pseudosymmetry caused misindexing that is impossible to resolve using Hough based indexing [27–30].

The data presented in this dissertation was all analyzed using standard Hough based indexing. Software packages including Oxford Instruments HKL Channel 5 and EDAX OIM Analysis have been used to analyze the EBSD data. Pseudosymmetry was a source of misindexing errors for all of the data presented here, however, all of the single crystal EBSD data was manually checked during indexing to ensure that the solution found using Hough indexing actually matched the experimental diffraction patterns. This manual checking cannot be performed for large orientation maps. There are several techniques commonly used for smoothing and reprocessing data in EBSD maps, however, these have been avoided here since data smoothing relies on interpolation and extrapolation of data that can produce false results when pseudosymmetry is involved.

2.3.2 Advanced Indexing Methods

Due to the limitations in current indexing techniques, there has been a need for new methods of indexing Kikuchi patterns that are better suited to dealing with issues such as noise in the patterns and misindexing due to pseudosymmetry. To avoid eliminating data as is done in Hough based indexing, several techniques have been developed that compare the full diffraction pattern image to diffraction patterns that have been simulated for the material of interest, accounting for all of the intensity information [30–35]. Here, a dictionary indexing method and associated software package, EMsoft, developed by Marc De Graef and his group will be briefly outlined.

The principle of dictionary indexing relies around accurately simulating diffraction patterns for a material that are then compared against experimentally collected diffraction patterns

for that material to determine the orientation of the experimental patterns. These simulated patterns become the "dictionary" that the indexing of experimental patterns is based on. To develop this dictionary, several simulation steps are involved. First, the spatial, energy, and depth distribution of backscattered electrons is simulated using a Monte Carlo simulation. This step requires the input of the energy of the incident electrons used experimentally as well as the specification of the material being measured. Secondly, the dynamical diffraction is modelled for the crystal structure of the material being measured. After this is done, a three-dimensional Kikuchi diffraction pattern will have been simulated. Finally, the detector geometry must be modelled so that the section of the full diffraction pattern that intersects the detector for a given orientation and detector geometry can be modelled and compared to the experimental patterns. This requires specification of detector geometry parameters such as scintillator pixel size, sample and detector tilt angles, and pattern center coordinates. Once all three simulation steps are complete, the experimental patterns are compared to simulated patterns by turning the intensity in pattern images into column vectors. Dot products of experimental and simulated vectors are calculated, with the maximum dot product being found for the closest matching patterns [36].

This dictionary indexing technique has been shown to much more reliably index patterns for EBSD but is currently much more computationally expensive than traditional Hough based indexing. However, it still relies on accurate simulation of diffraction patterns for the microscope system that has been used for data collection, as well as collection of appropriate patterns to use for the indexing. In this research, the EBSD camera that was used to collect patterns for dictionary indexing was not centered with respect to the phosphor screen. This misalignment in the detector hardware led to cropping of experimentally collected patterns that could not be resolved with software calibrations of the pattern cropping. Patterns were cropped with a non-circular mask resulting in artifacts that were saved into each experimentally collected pattern, as seen in Figure 2.10. Since non-centered circular masks are not yet supported in the EMsoft programs, this resulted in difficulty simulating detector geometries using these experimental patterns as well as difficulty indexing data collected on this particular EBSD system. Nevertheless, dictionary indexing should be utilized more fully in the future since it eliminates many of the issues currently experienced during EBSD data collection for CTZ.

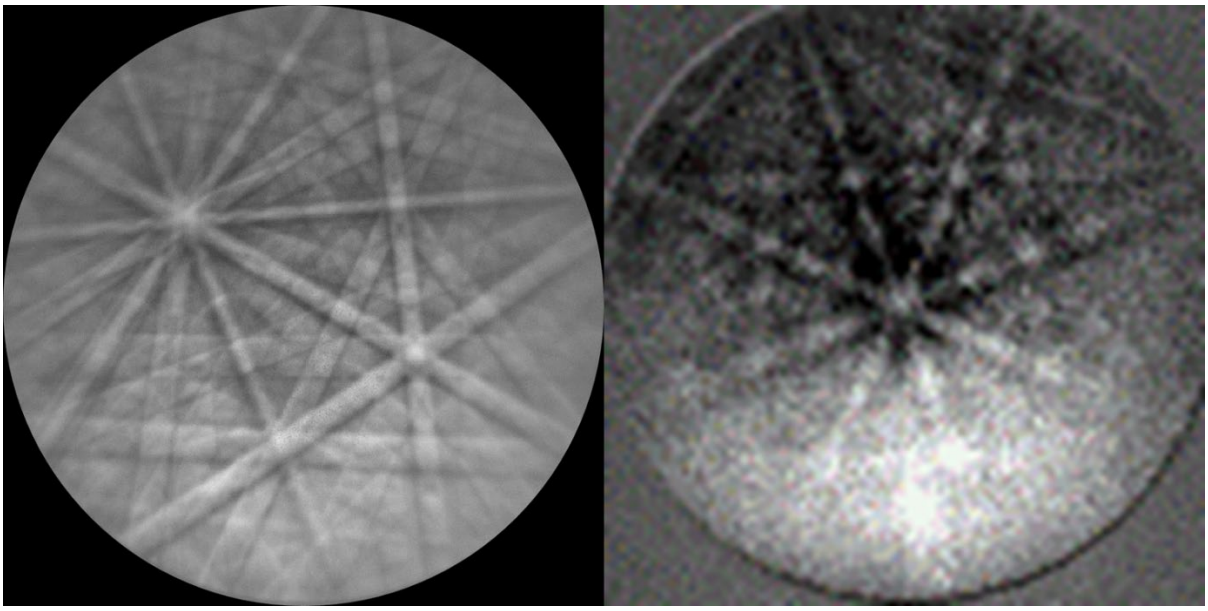

Figure 2.10: Images of Kikuchi patterns captured from a circular phosphor screen on a rectangular CCD camera. The image on the left shows proper circular cropping of an EBSD pattern while the image on the right shows a pattern that was saved during EBSD map collection where the circular pattern is cut off at the top and sides. This introduces artifacts into each experimental diffraction pattern. The image on the right is also noisier due to increased pixel binning used to increase the data collection speed.

2.4 Single Crystal Deformation

Deformation of single crystals has often been used as an important method for observing and determining the deformation mechanisms active in different materials. In this dissertation, single crystal deformation is used to observe the deformation mechanisms active in single crystals of ferroelastic CTZ. This is done to determine the mechanisms responsible for and associated with ferroelastic deformation as well as to measure the effect that variables such as crystal size and crystal orientation have on the deformation behavior. In this section, the methods used to deform samples at the micro-scale and nano-scale will be outlined.

2.4.1 Micropillar Compression

The micropillar compression test methodology was developed by Uchic et al. [37] to measure size effects in mechanical properties. For ceramic materials, reducing the size of samples is highly beneficial in reducing the volume of materials that may contain flaws that lead to fracture. For this reason, micropillar compression of ceramics has become advantageous for evaluating deformation mechanisms other than fracture for brittle ceramic materials [38–42]. Here,

micropillar compression of CTZ single crystals with a range of known orientations was used to determine the effect of orientation on ferroelastic domain nucleation stress. Specifically, these tests were used to evaluate whether domain nucleation follows a critical resolved shear stress criterion, the results of which are discussed in detail in Chapter 3.

To fabricate single crystal pillars at the micron scale, milling with a focused ion beam (FIB) was used. This technique allowed for site specific pillar fabrication with control of the dimensions down to the nanometer scale. For this study, the diameter of the pillars was selected such that approximately 10GPa of stress could be reached using a Hysitron Pi-85 Picoindeneter with a maximum load of 30mN. This size of pillar was small enough to suppress fracture while still being a large enough sample volume to represent a crystal size that may be found in many polycrystalline ceramic samples. Orientations of grains were determined using EBSD prior to pillar fabrication.

Pillars were milled using a four-step procedure optimized to reduce the taper angle of the pillars and to enable control of the dimensions of each pillar. Before any pillars could be milled, the milling ratio (ratio of actual trench depth to specified trench depth in the FIB software) for CTZ was determined. The milling ratio was found to be 2.2, meaning that for every 1 μm of milling depth specified for the milling step, 2.2μm depth of material was actually removed. This number was then used to determine the depths set for each subsequent milling step. First, rough 5μm diameter, 3μm length pillars were formed by milling with a 9.3nA FIB current to create a 25μm diameter annular trench large enough to accommodate the indenter tip during loading. The FIB current was then reduced to 790pA and the pillar diameter was decreased to 3μm through annular milling using reduced outer diameter of 6μm. Finally, the FIB current was reduced to 80pA and the pillar diameter was reduced to 2μm in two steps, one with an outer diameter of 4μm, and a second with an outer diameter of 2.4μm. The final height of each pillar was approximately 6.2μm. This milling procedure resulted in pillar geometries with very uniform dimensions and little taper, as shown in Figure 2.11, which shows a micropillar with a taper angle of 1.1°.

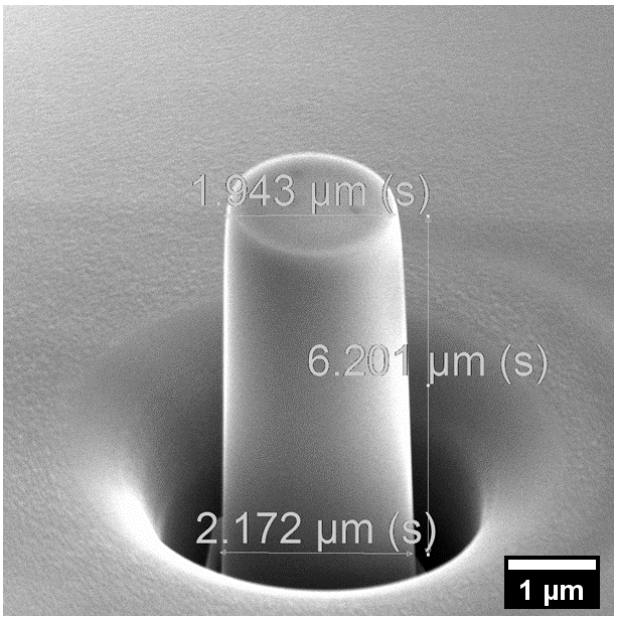

Figure 2.11: Image of a representative micropillar with measurements overlaid. The taper angle is 1.1°.

The locations of pillars were tracked using fiducial marks on the surface of the pellet such that the location of known orientations for each pillar could be tracked while indenting was done. The pellet was kept on the same stub while moving between the microscope in which EBSD was done and the FIB in which the pillars were fabricated so that the alignment did not change. That same stub was then loaded into the Hysitron PI-85 for deformation, again so that alignment was maintained between FIB milling and deformation steps.

2.4.2 *In Situ* TEM Deformation

Micropillar compression is extremely useful, however, it does not allow for direct observation of the microstructure (other than the pillar shape) or of defects during deformation. In order to observe the deformation events in greater detail, *in situ* transmission electron microscopy (TEM) deformation was used. TEM allows for direct observation of defects such as dislocations and twins, and when combined with in situ deformation, the nucleation and motion of those defects can be studied while quantitative stresses are simultaneous measured.

In situ TEM deformation tests were performed using a Hysitron PI-95 TEM Picoindenter inside of a JEOL 2010 TEM. Experiments were performed on samples in different geometries, including pillar compression and three-point notched beam bending. These geometries allowed for evaluation of the materials response under different loading conditions and stress states, each with

their own advantages and disadvantages. Samples consisted of single crystals or in some cases bicrystals.

Pillars were fabricated from grains with random orientations as well as in some cases from grains with known orientations. In cases where the orientation was known, careful tracking of the grain location was done between measuring the orientation using EBSD and lifting the grain out for nanopillar fabrication. A series of images showing the process for fabricating a pillar with known orientation is shown in Figure 2.12. In order to track the location of specific grains while moving them between microscopes, areas marked with various shapes were milled into polished and thermally etched pellets. EBSD was then done on the marked areas to collect orientation information for a large number of grains. Several grains with specific orientation were then marked using platinum deposition in the FIB. The selected grains were then lifted out using standard TEM sample preparation procedures, with the excess material cut away. Here, the samples were mounted on the top of a post on a copper TEM grid. Annular milling was then used to thin the pillars to diameters ranging from 250-600nm. The top of the pillar and any remaining platinum is removed by milling perpendicular to the pillar loading axis. In situ deformation of these pillars allowed for quantification of stresses associated with deformation events. However, since the pillars were still relatively thick for TEM samples, imaging of the deformation events had limited effectiveness.

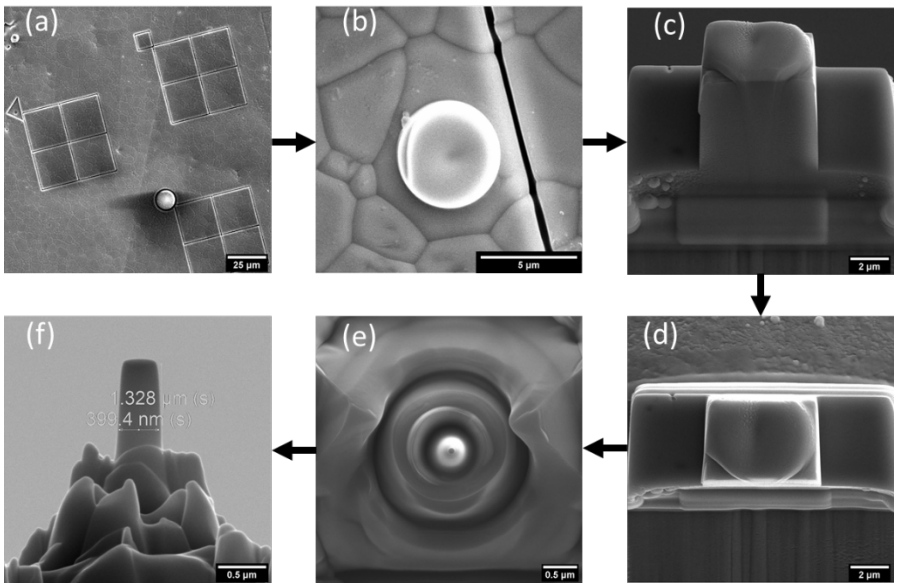

Figure 2.12: Images taken at various stages of fabricating a nanopillar with known orientation. (a) Areas are marked out on a polished polycrystalline surface where EBSD is performed. (b) A grain with known orientation is marked for FIB liftout. (c) The marked grain is lifted out using standard TEM sample preparation procedures. (d-e) The grain is milled into a pillar shape using a series of annular milling steps. (f) The top of the pillar is cut off perpendicular to the pillar loading axis to ensure a flat contact with the indenter tip. Typically pillars are several hundred nanometers in diameter and over a micron in length as shown by the overlaid measurements.

The three-point bending geometry was based off work done by Hu et al. [43]. This geometry allows for direct observation of crack growth. The same liftout steps were used to fabricate beam samples that were used for pillar samples, however, instead of annular milling, a standard TEM sample thinning procedure was used to thin the sample on top of the copper grid, and rectangular boxes the same as used by Hu et al. were milled through the samples. The crack growth in samples with this geometry was stable due to the clamped beam geometry, which prevents catastrophic crack growth. The goal of observing the region around the notch during bending was to image the nucleation of domains near a stress concentrator. The notch created a location with high tensile stress, making the presumed location of domain nucleation predictable. However, the stress state that forms around a notch in a sample with this geometry is complex, so correlating a coercive stress to any domain nucleation observed was difficult and has not yet been done.

Examples of a single crystal and a bicrystal beam being deformed are shown in Figure 2.13. The fracture process can be observed in real time for these samples. There is no obvious

dislocation plasticity or twinning visible during bending and crack propagation. In both cases the cracks arrest due to the compressive stress field induced by the cube corner indenter and the double cantilever beam geometry applying crack closure stresses.

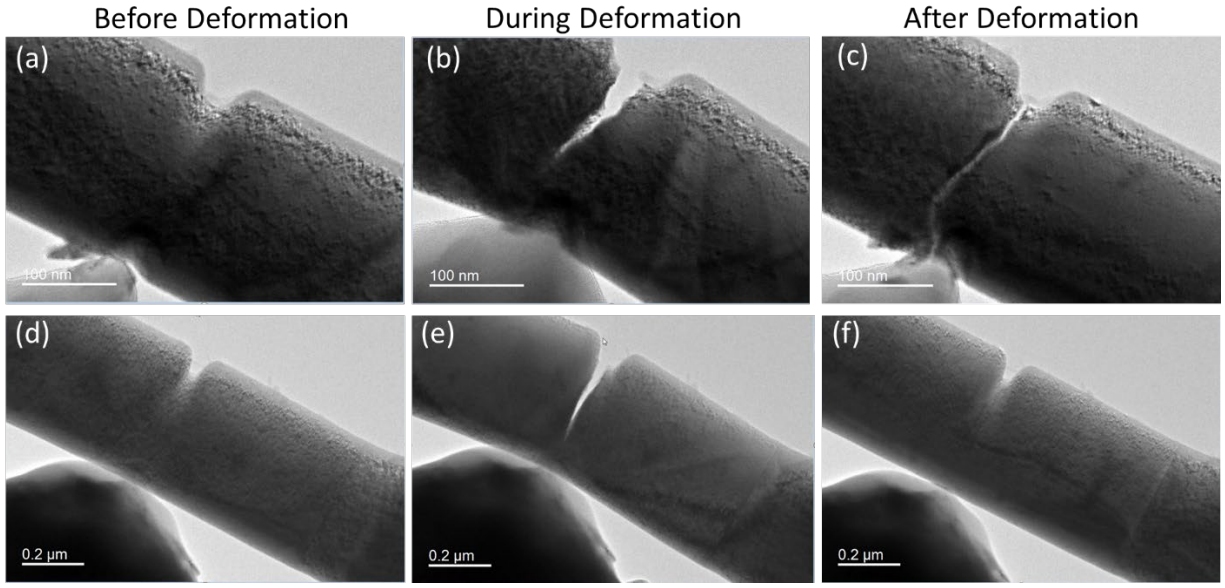

Figure 2.13: (a-c) Frames captured from video taken during the bending and fracture of a single crystal notched beam. The crack initiating and propagating from the notch is visible. Out of plane bending occurred resulting in incomplete closure of the crack after the load is removed. (d-e) Frames captured from video taken during the bending and fracture of a bicrystal beam. A planar grain boundary is visible traversing the beam along the right side of the images. Contrast from strain and bending can be seen during deformation. There appears to be some discontinuity in the strain at the grain boundary evidenced by the change in contrast at the boundary, and is likely caused by changes in the elastic properties of the material in the different grains. The crack closes entirely after the load is removed. Note: the scalebars in each image may be incorrect due to magnification changes not reflected in the scalebar during video collection.

Post-mortem diffraction done on the beam shown in Figure 2.13(a-c) is shown in Figure 2.14. Selected area diffraction patterns show that although no clear domain nucleation could be observed around the notch during the deformation, permanent deformation and domain nucleation indeed did take place, although it was not clear whether this occurred during the fracture process or due to out of plane bending of the sample due to misalignment with the indenter tip.

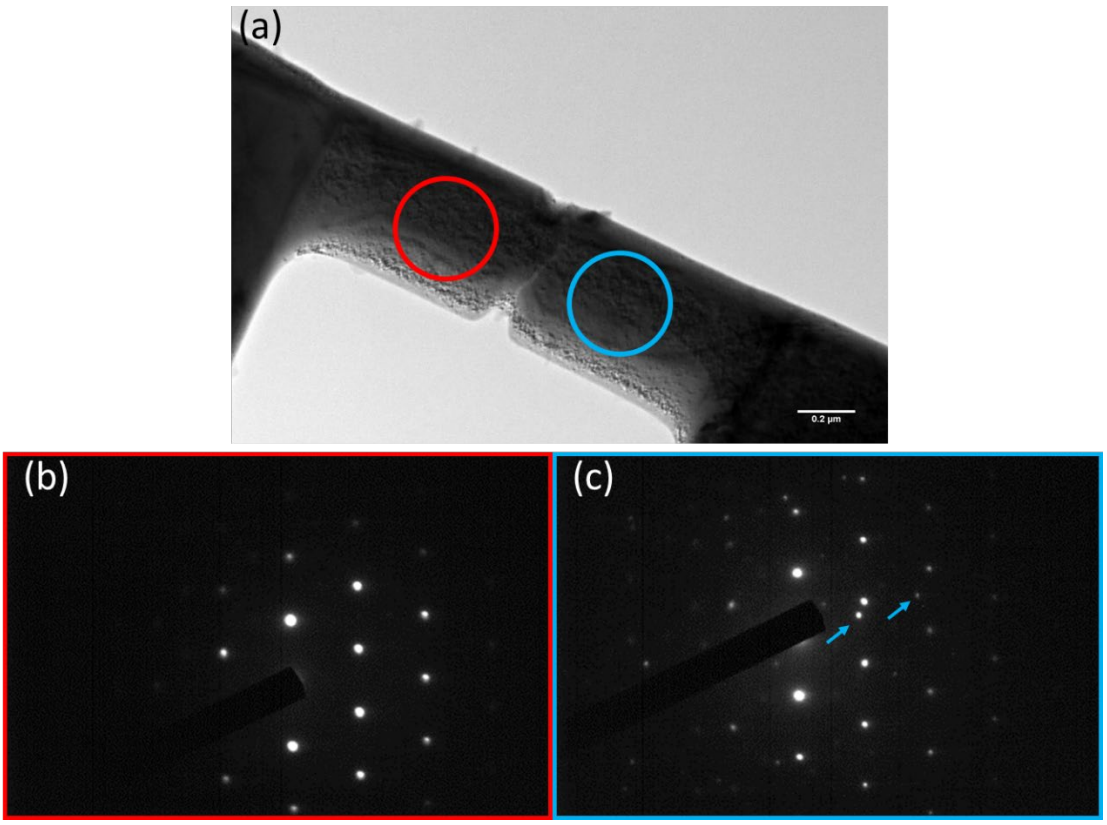

Figure 2.14: (a) TEM bright field image of a beam after deformation and fracture. The locations of two selected area diffraction patterns are shown in red and blue circles. (b) Selected area diffraction pattern showing the (110) zone axis diffraction pattern taken from the left side of the crack. The diffraction pattern shows a single crystal diffraction pattern with no evidence of twinning. (c) Selected area diffraction pattern showing the (110) zone axis diffraction pattern from the right side of the crack. The presence of additional spots, several of which are marked by arrows, is evidence of twinning and permanent deformation in this region.

2.5 Polycrystal Deformation

One of the main goals of the work done in this dissertation is to determine the effect that microstructure has on ferroelastic deformation. Because of this, it is necessary to study deformation in real ceramic microstructures. This section will focus on describing the methods used to deform polycrystalline ferroelastic samples such that the behavior of ferroelastic grains can be studied within the mechanical constraints imposed by the polycrystalline microstructure.

2.5.1 Microindentation

Microindentation techniques are useful for measuring a variety of material properties such as hardness, modulus, strength, and toughness. There are a number of different indenter geometries

commonly used for microindentation testing and different scales that properties such as hardness are measured on. For example, Knoop and Vickers indenters both use sharp pyramidal shaped indenter tips, however, Vickers indenters have a square base while Knoop indenters have an elongated base, and the indenter faces are at different angles. These differences result in different trends in hardness values being measured for various materials using the different indenter geometries [44]. In this work, the primary indentation methods used were Vickers indentation and spherical Hertzian indentation.

Vickers indentation is a common method for measuring hardness and fracture toughness for ceramics. One of the most common uses for Vickers indentation is to measure the hardness of materials. Hardness is measured using the equation:

$$H = \frac{1.8544P}{d^2} \qquad \text{Equation 2.2}$$

where P is the applied force and d is the diagonal length of the indent. Vickers indentation also commonly results in cracks radiating form the sharp corners of the indentation. Despite some controversy over the validity of comparing indentation fracture toughness measurements to other standard toughness evaluation techniques [45], measurement of these cracks is used to quantify toughness using the equation:

$$\Gamma = 2\xi^2 P\left(d^2/_{c^2}\right) \qquad \text{Equation 2.3}$$

where ξ is a geometrical factor equal to 0.016, P is the load, 2d is the diagonal dimension of the indent, and c is the crack length [46,47]. The stress state involved in deformation beneath and around a Vickers indent is complex, and significant residual stresses typically remain in the material after indentation. In this work, Vickers indentation was used for hardness measurements and to induce domain nucleation in polycrystals prepared with varying grain sizes.

Another method of indentation used was Hertzian indention where a spherical contact geometry is used. This contact geometry has the advantage that the stresses associated with the indentation process can be analytically determined using the following equations:

$$a = \sqrt[3]{\frac{3F}{8}\frac{(1-\nu_1^2)/E_1 + (1-\nu_2^2)/E_2}{1/d_1 + 1/d_2}} \quad \text{Equation 2.4}$$

$$p_{max} = \frac{3F}{2\pi a^2} \quad \text{Equation 2.5}$$

$$\sigma_x = \sigma_y = -p_{max}\left[\left(1 - \left|\frac{z}{a}\right|\tan^{-1}\frac{1}{|z/a|}(1+\nu) - \frac{1}{2\left(1+\frac{z^2}{a^2}\right)}\right)\right] \quad \text{Equation 2.6}$$

$$\sigma_z = \frac{-p_{max}}{1+\frac{z^2}{a^2}} \quad \text{Equation 2.7}$$

$$\tau_{max} = \frac{\sigma_x - \sigma_z}{2} = \frac{\sigma_y - \sigma_z}{2} \quad \text{Equation 2.8}$$

where F is the applied force, ν_1 and ν_2 are the Poisson ratios of the indenter and substrate, $E_1$and E_2 are the elastic moduli of the indenter and substrate, d_1 and d_2 are the diameters of the indenter and substrate (d_2 becomes infinite for a flat substrate), z is the depth below the surface, a is the contact radius, $-p_{max}$ is the maximum contact pressure, and σ_x, σ_y, σ_x and τ_{max} are principle stresses and maximum shear stress. These expressions make it possible to calculate and correlate stresses associated with Hertzian indentation to any deformation or fracture observed. Both Vickers and Hertzian indentation geometries were used to locally deform polycrystalline ferroelastic ceramics, however, Hertzian contact stresses were not yet able to be correlated to domain nucleation events. This will be discussed in more detail in Chapter 4.

2.5.2 *In Situ* SEM Deformation

Microindentation provides a route for evaluating the local response of ferroelastic ceramics to a heterogeneous, triaxial stress state, however, these measurements have only been done *ex situ.* To evaluate the local mechanical response of polycrystals to globally applied uniaxial compression, *in situ* SEM deformation coupled with digital image correlation (DIC) was used. Digital image correlation allows for full-field measurement of displacements and strains by tracking features in a series of images. Combining DIC with high resolution SEM imaging has been developed to allow for characterization of mechanical responses at increasingly small length scales [48–51]. These techniques were used for *in situ* evaluation of strain that develops in ferroelastic polycrystals during deformation.

To perform SEM-DIC, compression specimens were prepared to meet several requirements. First, the samples were fabricated into a geometry and with dimensions such that a uniaxial compressive load could reach stresses of several hundred megapascals. The load frame used inside the SEM that was used to compress the samples had a loadcell capable of reading 200N of maximum load. This severely limited the sample size, since high stresses were needed to deform CTZ samples. Because of this, samples were cut into millimeter scale beams with rectangular cross-sections from polished pellets. Samples were cut so that the cross-sectional area ranged from 0.5-1.0mm^2, enabling stresses of 200-400MPa to be applied at 200N. Customized compression platens were machined with a cutout for the beams to rest on, which are shown in Figure 2.15. The cutout was used to align samples during loading to ensure uniaxial compression, as well as to set a fixed height for imaging the samples during deformation. If samples were recessed too far beneath the surface of the platens, the SEM signal from the sample was reduced and imaging became impossible. Spacers cut from a 0.3mm thick Ti-6Al4V sheet were used to ensure that samples extended beyond the edge of the cutout surface, such that the sample bore all of the load during compression testing.

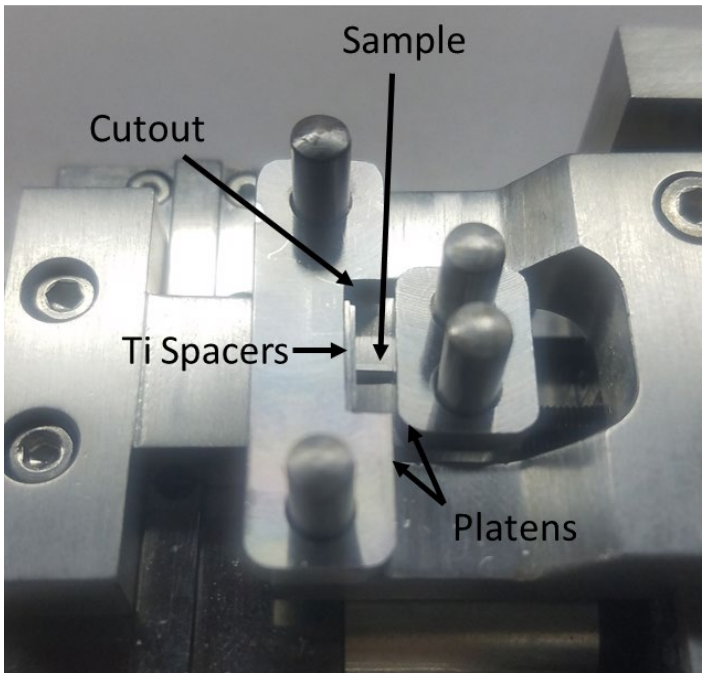

Figure 2.15: Photograph showing custom machined compression platens with a rectangular beam compression sample loaded. The cutout onto which samples were placed as well as the titanium spacers are shown.

Secondly, samples had to be coated with an appropriately sized speckle pattern for the digital image correlation analysis. This was done by sputtering layers of Au, Ti, and Ag onto the polished surface of each sample and using an NaCl solution to reconfigure the layers into DIC-appropriate speckle patterns using a process developed by Montgomery [52]. Images were then captured during loading. An image was taken after every 10N increase in load after waiting at least 60 seconds for drift to settle after each increase in load.

Even with the relatively small samples sizes used, no ferroelastic domain nucleation was observed in the fields of view measured using this technique so far. An example of a strain map collected during compression of a CTZ sample is shown in Figure 2.16. The speckle pattern produced well correlated images, however, the measured strains are very small and nothing except for elastic deformation and noise was measured.

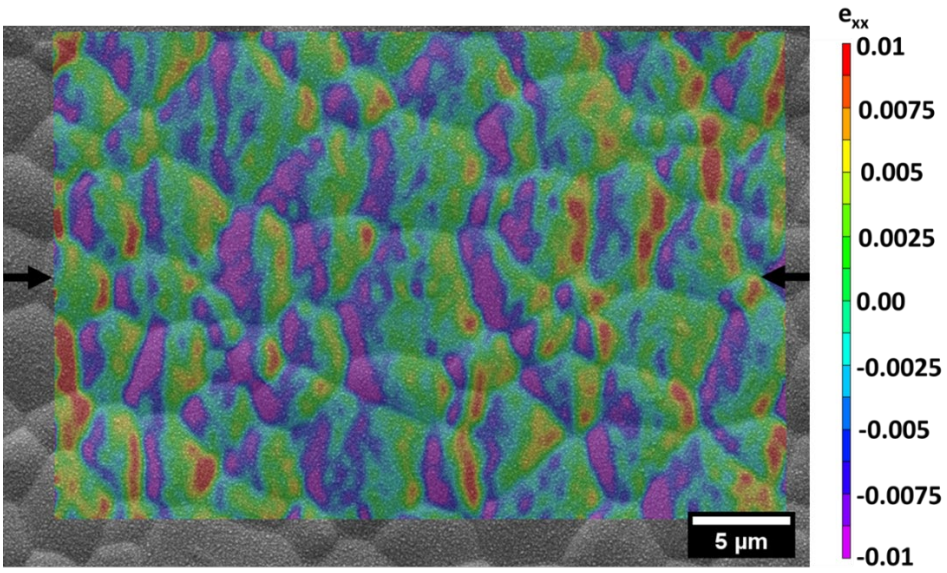

Figure 2.16: Digital image correlation strain map overlaid on an SEM image of a speckle patterned CTZ sample. Arrows show the direction of the applied compressive load. The sample was thermally etched, so that grain interiors and grain boundaries could be visually identified.

To further increase the local stress, and to increase the probability of observing ferroelastic deformation within the field of view, stress concentrators were milled into sample surfaces to locally increase stresses. Several diamond shaped trenches were milled into sample surfaces using FIB, examples of which can be seen in Figure 2.17. Unfortunately, even around stress concentrators, no ferroelastic domain nucleation was yet observed using this SEM-DIC technique.

Also, charging of the sample at the edges of the diamond trenches led to image distortions and artifacts in the DIC measurements as can be seen in Figure 2.17 (c). To mitigate this issue in the future, measurements near stress concentrators should be done such that sharp edges are not contained within the imaging field of view.

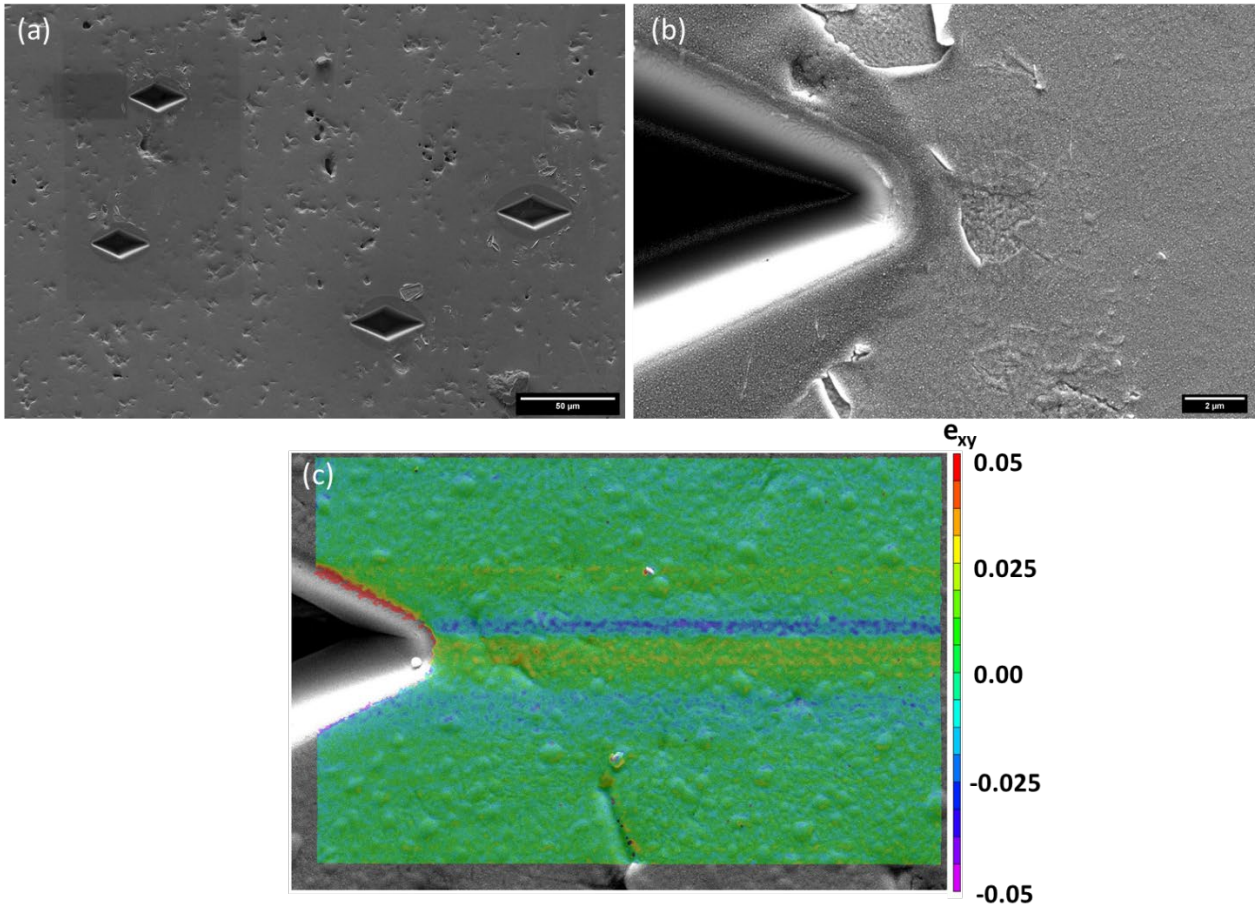

Figure 2.17: (a) Diamond trenches milled into a polished CTZ surface designed to act as local stress concentrators during compressive loading. (b) The sample was then speckle patterned for DIC measurements. (c) DIC strain map showing shear (xy) strain near a milled diamond trench during deformation. The deviations in strain from zero that appear as horizontal bands emanating from the diamond are caused by charging during imaging of the diamond edges, and the resulting images distortions.

2.6 References

[1] J.A. Krogstad, M. Lepple, C.G. Levi, Opportunities for improved TBC durability in the CeO2-TiO2-ZrO2 system, Surf. Coatings Technol. 221 (2013) 44–52. https://doi.org/10.1016/j.surfcoat.2013.01.026.

[2] M.J. Mayo, Synthesis and applications of nanocrystalline ceramics, Mater. Des. 14 (1993) 323–329.

[3] M.J. Mayo, D.C. Hague, D.-J. Chen, Processing nanocrystalline ceramics for applications in superplasticity, Mater. Sci. Eng. A. 166 (1993) 145–159. https://doi.org/https://doi.org/10.1016/0921-5093(93)90318-9.

[4] D. Hennings, Barium titanate based ceramic materials for dielectric use, Int. J. High Technol. Ceram. 3 (1987) 91–111. https://doi.org/https://doi.org/10.1016/0267-3762(87)90031-2.

[5] A. Kolleck, G.A. Schneider, F.A. Meschke, R-Curve Behavior of BaTiO3 - and PZT Ceramics Under the Influence of an Electric Filed Applied Parallel to the Crack Front, Acta Mater. 48 (2000) 4099–4113. https://doi.org/10.1016/S1359-6454(00)00198-1.

[6] F. Meschke, A. Kolleck, G.A. Schneider, R-curve behaviour of BaTiO3 due to stress-induced ferroelastic domain switching, J. Eur. Ceram. Soc. 17 (1997) 1143–1149. https://doi.org/10.1016/s0955-2219(96)00211-7.

[7] W.M. Kriven, B.R. Rosczyk, SOFC Powder Synthesis by the Organic Steric Entrapment Method, in: N. Sammes, A. Smirnova, O. Vasylyev (Eds.), Fuel Cell Technol. State Perspect., Springer Netherlands, Dordrecht, 2005: pp. 381–394.

[8] S.-J. Lee, M.D. Biegalski, W.M. Kriven, Barium Titanate and Barium Orthotitanate Powders Through An Ethylene Glycol Polymerization Route, in: 23rd Annu. Conf. Compos. Adv. Ceram. Mater. Struct. A Ceram. Eng. Sci. Proc., John Wiley & Sons, Ltd, 2008: pp. 11–18. https://doi.org/10.1002/9780470294567.ch2.

[9] N. Orlovskaya, K. Kleveland, T. Grande, M. Einarsrud, Mechanical properties of LaCoO 3 based ceramics, 20 (2000) 51–56.

[10] K. Kleveland, N. Orlovskaya, T. Grande, A. Marie, M. Moe, M. Einarsrud, K. Breder, G. Gogotsi, Ferroelastic Behavior of LaCoO 3 -Based Ceramics, 33 (2001) 2029–2033.

[11] V. V. Kharton, F.M. Figueiredo, A. V. Kovalevsky, A.P. Viskup, E.N. Naumovich, A.A. Yaremchenko, I.A. Bashmakov, F.M.B. Marques, Processing, microstructure and properties of LaCoO3-δ ceramics, J. Eur. Ceram. Soc. 21 (2001) 2301–2309.

https://doi.org/10.1016/S0955-2219(01)00199-6.

[12] H.U. Anderson, Review of p-type doped perovskite materials for SOFC and other applications, Solid State Ionics. 52 (1992) 33–41. https://doi.org/https://doi.org/10.1016/0167-2738(92)90089-8.

[13] J. Mizusaki, Nonstoichiometry, diffusion, and electrical properties of perovskite-type oxide electrode materials, Solid State Ionics. 52 (1992) 79–91. https://doi.org/https://doi.org/10.1016/0167-2738(92)90093-5.

[14] S. Carter, A. Selcuk, R.J. Chater, J. Kajda, J.A. Kilner, B.C.H. Steele, Oxygen transport in selected nonstoichiometric perovskite-structure oxides, Solid State Ionics. 53–56 (1992) 597–605. https://doi.org/https://doi.org/10.1016/0167-2738(92)90435-R.

[15] R.A. [De Souza], J.A. Kilner, Oxygen transport in La1−xSrxMn1−yCoyO3±δ perovskites: Part I. Oxygen tracer diffusion, Solid State Ionics. 106 (1998) 175–187. https://doi.org/https://doi.org/10.1016/S0167-2738(97)00499-2.

[16] C.H. Chen, H. Kruidhof, H.J.M. Bouwmeester, A.J. Burggraaf, Ionic conductivity of perovskite LaCoO3 measured by oxygen permeation technique, J. Appl. Electrochem. 27 (1997) 71–75.

[17] E.R. Twiname, R.E. Mistler, Tape casting and lamination, (2001).

[18] Z.A. Munir, U. Anselmi-Tamburini, M. Ohyanagi, The effect of electric field and pressure on the synthesis and consolidation of materials: A review of the spark plasma sintering method, J. Mater. Sci. 41 (2006) 763–777. https://doi.org/10.1007/s10853-006-6555-2.

[19] O. Guillon, J. Gonzalez-Julian, B. Dargatz, T. Kessel, G. Schierning, J. Räthel, M. Herrmann, Field-assisted sintering technology/spark plasma sintering: Mechanisms, materials, and technology developments, Adv. Eng. Mater. 16 (2014) 830–849. https://doi.org/10.1002/adem.201300409.

[20] D.N.F. Muche, J.W. Drazin, J. Mardinly, S. Dey, R.H.R. Castro, Colossal grain boundary strengthening in ultrafine nanocrystalline oxides, Mater. Lett. 186 (2017) 298–300. https://doi.org/https://doi.org/10.1016/j.matlet.2016.10.035.

[21] D.B. Williams, C.B. Carter, Kikuchi Diffraction, in: Transm. Electron Microsc. A Textb. Mater. Sci., Springer US, Boston, MA, 2009: pp. 311–322. https://doi.org/10.1007/978-0-387-76501-3_19.

[22] N.C. Krieger Lassen, D. Juul Jensen, K. Conradsen, On the statistical analysis of orientation data, Acta Crystallogr. Sect. A. 50 (1994) 741–748. https://doi.org/10.1107/S010876739400437X.

[23] J.A. Venables, C.J. Harland, Electron back-scattering patterns—A new technique for obtaining crystallographic information in the scanning electron microscope, Philos. Mag. A J. Theor. Exp. Appl. Phys. 27 (1973) 1193–1200. https://doi.org/10.1080/14786437308225827.

[24] S.I. Wright, Fundamentals of Automated EBSD, in: A.J. Schwartz, M. Kumar, B.L. Adams (Eds.), Electron Backscatter Diffr. Mater. Sci., Springer US, Boston, MA, 2000: pp. 51–64. https://doi.org/10.1007/978-1-4757-3205-4_5.

[25] The formation of the electron bacscatter diffraction pattern (EBSP), (n.d.). http://www.ebsd.com/images/articles/59/fig_1a.jpg.

[26] S.I. Wright, D.P. Field, D.J. Dingley, Advanced Software Capabilities for Automated EBSD, in: A.J. Schwartz, M. Kumar, B.L. Adams (Eds.), Electron Backscatter Diffr. Mater. Sci., Springer US, Boston, MA, 2000: pp. 141–152. https://doi.org/10.1007/978-1-4757-3205-4_13.

[27] M.M. Nowell, S.I. Wright, Orientation effects on indexing of electron backscatter diffraction patterns, Ultramicroscopy. 103 (2005) 41–58. https://doi.org/https://doi.org/10.1016/j.ultramic.2004.11.012.

[28] S. Martin, H. Berek, C.G. Aneziris, U. Martin, D. Rafaja, Pitfalls of local and quantitative phase analysis in partially stabilized zirconia, J. Appl. Crystallogr. 45 (2012) 1136–1144. https://doi.org/10.1107/S0021889812038733.

[29] V. Ocelík, U. Schepke, H.H. Rasoul, M.S. Cune, J.T.M. De Hosson, On the bulk degradation of yttria-stabilized nanocrystalline zirconia dental implant abutments: an electron backscatter diffraction study, J. Mater. Sci. Mater. Med. 28 (2017) 121.

https://doi.org/10.1007/s10856-017-5927-2.

[30] E.L. Pang, P.M. Larsen, C.A. Schuh, Resolving pseudosymmetry in tetragonal ZrO2 using EBSD with a modified dictionary indexing approach, (2020).

[31] A.J. Wilkinson, D.J. Dingley, G. Meaden, Strain Mapping Using Electron Backscatter Diffraction, in: A.J. Schwartz, M. Kumar, B.L. Adams, D.P. Field (Eds.), Electron Backscatter Diffr. Mater. Sci., Springer US, Boston, MA, 2009: pp. 231–249. https://doi.org/10.1007/978-0-387-88136-2_17.

[32] W.C. Lenthe, S. Singh, M. De Graef, A spherical harmonic transform approach to the indexing of electron back-scattered diffraction patterns, Ultramicroscopy. 207 (2019) 112841. https://doi.org/https://doi.org/10.1016/j.ultramic.2019.112841.

[33] G. Nolze, A. Winkelmann, A.P. Boyle, Pattern matching approach to pseudosymmetry problems in electron backscatter diffraction, Ultramicroscopy. 160 (2016) 146–154. https://doi.org/https://doi.org/10.1016/j.ultramic.2015.10.010.

[34] M.A. Jackson, E. Pascal, M. De Graef, Dictionary Indexing of Electron Back-Scatter Diffraction Patterns: a Hands-On Tutorial, Integr. Mater. Manuf. Innov. 8 (2019) 226–246. https://doi.org/10.1007/s40192-019-00137-4.

[35] Y.-H. Chen, S.U. Park, D. Wei, G. Newstadt, M. Jackson, J.P. Simmons, M. De Graef, A.O. Hero, A Dictionary Approach to EBSD Indexing, (2015).

[36] M. De Graef, Dictionary Indexing Tutorial, in: EBSD 2018 Tutor., 2018.

[37] M.D. Uchic, D.M. Dimiduk, J.N. Florando, W.D. Nix, Exploring specimen size effects in plastic deformation of Ni $_3$ (Al, Ta), MRS Proc. 753 (2002) BB1.4. https://doi.org/10.1557/PROC-753-BB1.4.

[38] A. Lai, Z. Du, C.L. Gan, C.A. Schuh, Shape Memory and Superelastic Ceramics at Small Scales, Science (80-.). 341 (2013) 1505 LP – 1508. https://doi.org/10.1126/science.1239745.

[39] X.M. Zeng, A. Lai, C.L. Gan, C.A. Schuh, Crystal orientation dependence of the stress-induced martensitic transformation in zirconia-based shape memory ceramics, Acta Mater.

116 (2016) 124–135. https://doi.org/10.1016/j.actamat.2016.06.030.

[40] E. Camposilvan, M. Anglada, Size and plasticity effects in zirconia micropillars compression, Acta Mater. 103 (2016) 882–892. https://doi.org/10.1016/j.actamat.2015.10.047.

[41] E. Camposilvan, M. Anglada, Micropillar compression inside zirconia degraded layer, J. Eur. Ceram. Soc. 35 (2015) 4051–4058. https://doi.org/10.1016/j.jeurceramsoc.2015.04.017.

[42] S. Korte, W.J. Clegg, Micropillar compression of ceramics at elevated temperatures, Scr. Mater. 60 (2009) 807–810. https://doi.org/10.1016/j.scriptamat.2009.01.029.

[43] Y. Hu, J.-H. Huang, J.-M. Zuo, In situ characterization of fracture toughness and dynamics of nanocrystalline titanium nitride films, J. Mater. Res. 31 (2016) 370–379. https://doi.org/10.1557/jmr.2016.4.

[44] D. Chicot, D. Mercier, F. Roudet, K. Silva, M.H. Staia, J. Lesage, Comparison of instrumented Knoop and Vickers hardness measurements on various soft materials and hard ceramics, J. Eur. Ceram. Soc. 27 (2007) 1905–1911. https://doi.org/https://doi.org/10.1016/j.jeurceramsoc.2006.06.011.

[45] G.D. Quinn, R.C. Bradt, On the Vickers Indentation Fracture Toughness Test, J. Am. Ceram. Soc. 90 (2007) 673–680. https://doi.org/10.1111/j.1551-2916.2006.01482.x.

[46] T.A. Schaedler, R.M. Leckie, S. Krämer, A.G. Evans, C.G. Levi, Toughening of Nontransformable t′-YSZ by Addition of Titania, J. Am. Ceram. Soc. 90 (2007) 3896–3901. https://doi.org/10.1111/j.1551-2916.2007.01990.x.

[47] G.R. ANSTIS, P. CHANTIKUL, B.R. LAWN, D.B. MARSHALL, A Critical Evaluation of Indentation Techniques for Measuring Fracture Toughness: I, Direct Crack Measurements, J. Am. Ceram. Soc. 64 (1981) 533–538. https://doi.org/10.1111/j.1151-2916.1981.tb10320.x.

[48] M.A. Sutton, N. Li, D.C. Joy, A.P. Reynolds, X. Li, Scanning Electron Microscopy for Quantitative Small and Large Deformation Measurements Part I: SEM Imaging at Magnifications from 200 to 10,000, Exp. Mech. 47 (2007) 775–787.

https://doi.org/10.1007/s11340-007-9042-z.

[49] M.A. Sutton, N. Li, D. Garcia, N. Cornille, J.J. Orteu, S.R. McNeill, H.W. Schreier, X. Li, A.P. Reynolds, Scanning Electron Microscopy for Quantitative Small and Large Deformation Measurements Part II: Experimental Validation for Magnifications from 200 to 10,000, Exp. Mech. 47 (2007) 789–804. https://doi.org/10.1007/s11340-007-9041-0.

[50] N. Li, M.A. Sutton, X. Li, H.W. Schreier, Full-field Thermal Deformation Measurements in a Scanning Electron Microscope by 2D Digital Image Correlation, Exp. Mech. 48 (2008) 635–646. https://doi.org/10.1007/s11340-007-9107-z.

[51] A.D. Kammers, S. Daly, Digital Image Correlation under Scanning Electron Microscopy: Methodology and Validation, Exp. Mech. 53 (2013) 1743–1761. https://doi.org/10.1007/s11340-013-9782-x.

[52] C.B. Montgomery, B. Koohbor, N.R. Sottos, A Robust Patterning Technique for Electron Microscopy-Based Digital Image Correlation at Sub-Micron Resolutions, Exp. Mech. 59 (2019) 1063–1073. https://doi.org/10.1007/s11340-019-00487-2.

CHAPTER 3

EVALUATING A CRITICAL RESOLVED SHEAR STRESS CRITERION FOR DOMAIN NUCLEATION IN FERROELASTIC CERAMICS

In this chapter, the microscale behavior of domain nucleation in ferroelastic single crystals will be discussed. Here, the first hypothesis outlined in section 1.6 will be evaluated, testing whether ferroelastic domain nucleation is governed by a critical resolved shear stress criterion similar to Schmid's law. Tests were performed using single crystal micropillars such that the effect of crystal orientation on the domain nucleation behavior could be isolated. The effect that orientation has on the deformation behavior will be discussed, followed by discussion of the mechanisms responsible for and associated with domain nucleation. The results detailed in this chapter will give context to the domain nucleation behavior observed in bulk polycrystalline samples discussed in chapter 4. These results provide insight into the microscale processes involved in ferroelastic deformation that must be connected to the deformation behavior in bulk microstructures for informed design of intrinsically toughened ceramics.

3.1 Introduction

Ferroelastic deformation provides a mechanism by which typically brittle ceramics may be intrinsically toughened. This toughness is achieved through the stress induced nucleation and motion of domains with differing orientation, but identical structure, within a crystal [1]. The nucleation of these domains occurs by twinning across specific planes for a given crystal structure. Domains may then grow and reconfigure during continued application of stress. Ferroelastic toughening is present in a wide variety of structural and electrical ceramics. For instance, the high toughness seen in single phase tetragonal *t'* zirconia has been ascribed to ferroelastic toughening [2–4], while increased toughness in tetragonal lead zirconate titanate [3,5] and barium titanate [6,7] has also been reported due to nucleation and motion of ferroelastic domains.

The conformation and evolution of ferroelastic domains under stress has been well characterized in a variety of ceramic systems [4,8–11]. However, most studies of domain evolution, to date, have investigated polydomain materials—meaning that the ferroelastic domain boundaries exist in the material before an external load is applied, often as a result of processing. It has been postulated in previous studies of *t'* zirconia, that ferroelastic domain nucleation may

contribute greater increases in toughness relative to that arising from the motion of existing domain boundaries [2]. For this reason, the present investigation focuses the mechanical nucleation of domains in initially single-domain crystals of tetragonal zirconia.

In tetragonal ferroelastic ceramics, domains have been observed to form by twinning on the {110} family of planes [9,10,12]. Typically, the c-axis of the tetragonal unit cell reorients to align perpendicular to compressive stress and parallel to a tensile stress. The deformation and realignment of domains occurs through shear stresses acting on the given deformation plane [13]. Conventionally, a given ferroelastic material is described as having a critical value of shear stress necessary to nucleate or move domain walls or twins. Following the terminology adopted for other ferroic systems, this critical value is termed the coercive stress. Because most studies have been performed on polydomain samples, most values of coercive stress that have been reported are for domain motion rather than nucleation. Here, the authors seek to evaluate the coercive stress for domain nucleation and have hypothesized that domain nucleation in single crystals is governed by a critical resolved shear stress criterion. A critical resolved shear stress criterion like Schmid's Law is evaluated as

$$\tau_c = \sigma_n \cos\phi \cos\lambda \qquad \text{Equation 3.1}$$

where τ_c is the critical resolved shear stress for domain nucleation, σ_n is the normal stress causing the deformation, ϕ is the angle of the twin plane normal with respect to the loading axis, and λ is the angle of the propagation of domain reorientation with respect to the loading axis. A similar approach has been taken previously to evaluate critical resolved shear stress for twinning in FCC crystals, finding that twinning follows Schmid's Law [14]. Critical shear stress criteria have also been used to analyze domain switching mechanics in relaxor ferroelectrics, and have found good agreement with resulting domain morphologies [15].

To test this hypothesis, single-domain crystals with a range of known orientations must be deformed to the point that domains are nucleated. Tetragonal zirconia stabilized with 10 mol% ceria and 10 mol% titania (CTZ) was selected on the basis that it can be synthesized and processed entirely in the tetragonal phase (such that it remains single-domain prior to application of stress), has a relatively high tetragonality (c/a = 1.026), and is known to exhibit a ferroelastic response under stress [16]. Successful evaluation also requires that fracture can be suppressed. Small scale micropillar compression provides a useful route for this, and has been used for similar evaluation of other deformation mechanisms in ceramics [17–21].

3.2 Experimental Methods

3.2.1 Materials and Sample Preparation

Tetragonal phase CTZ powders were prepared using reverse-coprecipitation synthesis [22]. Cerium nitrate, zirconium butoxide, and titanium isopropoxide precursors were dissolved into 200 proof ethanol to achieve the desired molar ratio (10Ce-10Ti-80Zr) of cations. The solution was then slowly added to an excess of ammonium hydroxide with pH maintained above 10.5 to facilitate rapid precipitation. The precipitates were then centrifuged, washed with ethanol several times, and dried. After drying, the precipitates were ground and calcined at 600°C for 4 hours. The powders were then pressed into a 10 mm pellet and sintered in several stages at 1350°C for a total of 231 hours in a box furnace to densify the sample and grow the grains such that single crystal micropillars could be fabricated within them.

X-ray diffraction was used to confirm that the pellet was in the desired tetragonal phase using a Bruker D5000. The pellet was then polished using diamond lapping films and alumina slurries followed by a thermal etch at 1350°C for one hour to enhance grain boundary contrast. The thermally etched sample was mounted onto a stub used for orientation indexing, pillar milling, and pillar deformation. The sample remained on the stub between pillar fabrication and deformation sessions to eliminate opportunity for misalignment of the pillar loading axis.

The orientations of various grains at the sample surface were determined using electron backscatter (EBSD). Patterns were indexed to a tetragonal zirconia phase using six Kikuchi bands. Orientation solutions were accepted only if the mean angular distribution (MAD) was below 1.2°. EBSD was performed in a JEOL 7000F SEM using an Oxford HKL EBSD system. Micropillars were milled into grains with known orientation using an FEI Helios focused ion beam. For this study, all pillars were milled into a single pellet, to reduce the chance of heterogeneity between samples influencing the results. pillars were milled using a four-step procedure optimized to reduce the taper angle of the pillars and to enable control of the dimensions of each pillar. First, rough 5µm diameter, 3µm length pillars were formed by milling with a 9.3nA FIB current to create a 25µm diameter annular trench large enough to accommodate the indenter tip during loading. The FIB current was then reduced to 790pA and the pillar diameter was decreased to 3µm by annular milling. Finally, the FIB current was reduced to 80pA and the pillar diameter was reduced to 2µm in two milling steps. The final height of each pillar was approximately 6.2µm and had taper angles

of less than 2°. These dimensions were selected to ensure uniform compression without buckling, but it can also be noted that the pillar volumes were on par with the volume of an individual grain within a conventionally processed polycrystalline ceramic.

Each pillar was deformed by uniaxial compression inside the FEI Helios FIB using a Hysitron PI-85 indenter equipped with a 12μm diameter diamond flat punch indenter, which was coated with Au/Pd to reduce charging while imaging. The electron beam imaging in the FIB was used to align the indenter tip with each pillar. Deformation was done at a rate of 4nm/sec under displacement control. The load vs displacement curve was continually monitored during deformation. In some cases, the load function was stopped quickly once the first deformation event for a pillar was observed, while in other cases, the deformation was allowed to progress to the end of the 600nm total displacement of the load function before the pillar was unloaded at a rate of 8nm/sec. In some cases, pillars were loaded and deformed several consecutive times. After deformation, several pillars were lifted out and thinned for transmission electron microscopy imaging and diffraction in a JEOL 2010 TEM and a JEOL 2100 CRYO TEM.

3.2.2 Shear Stress Analysis Procedure

In order to evaluate a critical resolved shear stress criterion, several comparisons of orientation and deformation stress were used. As noted in the introduction, the c-axis of the tetragonal crystals tend to align perpendicular to an applied compressive stress through 90° reorientations. Therefore, a first approximation for a resolved shear stress criterion compares the observed normal stress at the onset of deformation to the crystallographic misorientation of the pillar from the (001) plane normal. This approximation evaluates the assumption that pillars with (001) orientation will twin most easily since the shear stress resolved onto the favorable (011) twin plane will be maximized in this orientation. As the (001) plane becomes misoriented further from the loading axis, the resolved shear stress on the (011) plane decreases. Angles of planes relative to the loading axis have been determined using the equation

$$\cos\emptyset = \frac{\frac{1}{a^2}(h_1h_2+k_1k_2)+\frac{1}{c^2}(l_1l_2)}{\sqrt{\left[\frac{1}{a^2}(h_1^2+k_1^2)+\frac{1}{c^2}(l_1^2)\right]\left[\frac{1}{a^2}(h_2^2+k_2^2)+\frac{1}{c^2}(l_2^2)\right]}} \qquad \text{Equation 3.2}$$

which accounts for the tetragonal structure of CTZ [23]. Equation 3.2 can then be used as a reasonable proxy for twinning probability—that is, as a route to test whether orientations closer to

(001) orientations are indeed more favorable for twinning, and orientations further from (001) are less favorable.

The above first order analysis ignores the direction angle found in the conventional formulation of Schmid's Law given in Eq. 3.1. A more complete analysis requires that both a twin plane and shear direction are determined. Several assumptions are necessary to do this, the first of which pertains to the twin plane determination. Twins may nucleate on any of 12 {110}-type planes in the tetragonal crystal structure. Here, the analysis has been performed assuming that the most likely plane for domain nucleation will be the {110}-type twin plane that is closest to 45° in angle to the loading axis (maximum resolved shear stress). This is further complicated by the fact that not all {110} twin planes represent reorientations of the tetragonal c-axis and therefore a proper ferroelastic transition. Of the {110} family of planes, planes where {h≠0, k≠0, l=0) will not involve c-axis reorientations. Rather, they would correspond to a-b reorientations and are considered separately. Here, two cases are considered: one where all {110} planes are included in the calculations (regardless of whether c-axis reorientations are possible), and another where {110} planes corresponding to a-b reorientations are excluded. In the case where the planes are excluded, the next closest {110} plane that does include c-axis reorientations is assumed to activate first. The direction of twin shear must then also be assumed. Based on previous *in situ* straining studies performed on *t'* zirconia, it is assumed that domain reorientation propagates in <110> directions [10].

3.3 Results

3.3.1 Phase and Initial Microstructure

Isolating ferroelastic domain nucleation requires a single tetragonal phase throughout the ceramic and that only a single domain variant is present within each grain of the polycrystalline body. The as prepared ceramic pellets were confirmed to be single phase via X-ray diffraction as shown in Figure 1. The XRD data was fit to a tetragonal zirconia phase with lattice parameters of a=b=3.608 Å, c=5.232 Å., giving a relatively large tetragonality ratio of 1.026, were the ratio is defined as $c/(a\sqrt{2})$ assuming a pseudocubic crystal unit cell according to convention [24]. The phase of each pillar was again confirmed during orientation indexing by EBSD since any poor fit to the tetragonal zirconia phase was rejected for pillar fabrication. The initial microstructure found

to be free of twins at the surface as is expected since the pellets were densified below the estimated Curie temperature for the ferroelastic/paraelastic transition [25].

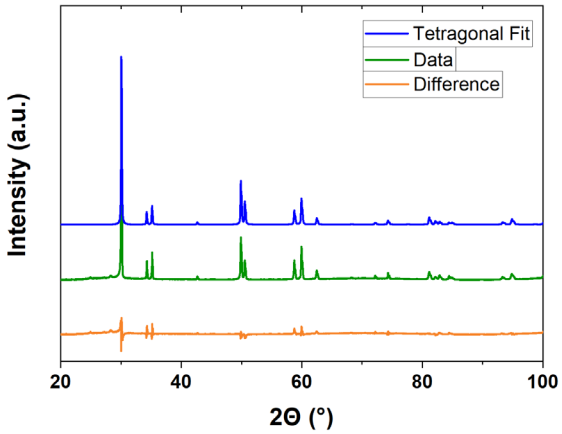

Figure 3.1: XRD of sintered CTZ.

3.3.2 Pillar Compression

Significant deformation events during micropillar compression can be characterized by the magnitude of the displacement discontinuity and the normal stress at which the event occurred, henceforth referred to as the deformation stress. The magnitude of the deformation events varied significantly from pillar to pillar, with the smallest single event producing a jump of less than 1 nm in displacement (Pillar 22) and the largest single event producing a 721 nm jump in displacement (Pillar 7). Initial deformation stresses ranging from 94 MPa (Pillar 18) to 5082 MPa (Pillar 25) were observed. Several representative stress-displacement curves are provided in Figure 3.2, from which it is clear that unloading behavior also varied dramatically. Stress has been plotted against displacement rather than strain due to the fact that the precise gauge length of each pillar could not be directly measured.

For example, Pillars 25 and 11 (Figure 3.2(a) and 3.2(b)) both exhibited a single deformation event before unloading. Pillar 25 was permanently deformed, as is evident from the residual displacement at zero stress and the visible changes in the shape of the Pillar. Similar permanent deformation behavior was found for other pillars as well, specifically pillars 1, 2, 3, 5, 6, 7, 10, 12, 16, 19, 22, 23, and 24. However, Pillar 11 recovered almost completely upon unloading, through the course of several smaller reverse displacement jumps. This was also the

case for pillars 4, 8, 14, 15, 17, 18, 20, and 21. In other cases, like pillars 9 and 13, the recovery occurred all at once or in large reverse displacement jumps, similar to those observed during loading.

Post deformation Pillar morphologies can be classified as those that exhibited (i) no apparent change in shape, Pillars 4, 5, 6, 8, 9, 10, 11, 12, 13, 16, 17, 18, and 21; (ii) shear distortions, Pillars 7, 14, 15, 19, 20, 23, 24, and 25; (iii) surface striations, Pillars 1, 2, and 7; or (iv) fracture, Pillars 3, and 22. Figure 3.2(a,e,f) provide examples of shear distortions and changes in shape. The top surface of the pillars remains flat and parallel to the sample surface indicating that the shear and change in shape is not due to off axis loading or sample bending. Surface striations, characteristic of slip, are apparent on Pillar 2 in Figure 3.2(c), while Figure 3.2(d) illustrates the fourth class of deformed pillar morphology.

Careful inspection of pillars in the second class suggests the presence of multiple twins—consider Figure 3.2(a) and Figure 3.6(a,c,e). These pillars, 25 and 7 respectively, both experienced just one observable deformation event. While Pillar 15 (Figure 3.2(e)), exhibits multiple deformation events in the loading curve, but visually contains what appears to be only a single, large shear distortion.

Several pillars were loaded several times to evaluate the effect of defects introduced during previous loading cycles on subsequent deformation. Pillars were loaded up to three times, with the load being completely removed before the next load was applied. Here again, the behavior of the pillars varied. Some pillars exhibited a reduction in the stress required for a deformation event to occur with subsequent loading cycles, as can be seen in Figure 3.2(e), whereas others experienced an increase in stress required for subsequent deformation events, as is seen in Figure 3.2(f). Repeated loading also gave rise to changes in the loading curve slopes.

After deformation, several representative pillars exhibiting the range of behaviors observed in this study were sectioned and evaluated using TEM. Figure 3.3 shows examples from the interiors of Pillars 9, 2, and 1. Pillar 9 experienced a deformation event that recovered almost completely during unloading. No residual defects were observed in the interior of this pillar. In contrast to pillar 9, pillars 2 and 1 experienced permanent deformation. The interior of pillar 2 exhibited evidence of shearing from dislocation plasticity consistent with the striations observed on the exterior of this pillar, but no evidence of residual twins. Pillar 1 contained residual twins as well as evidence of dislocation plasticity. Figure 3.6 also shows the interior of pillar 7 which

contained a substantial number of nucleated defects, which appear to be multiple twins, as well as microcracks and dislocation activity.

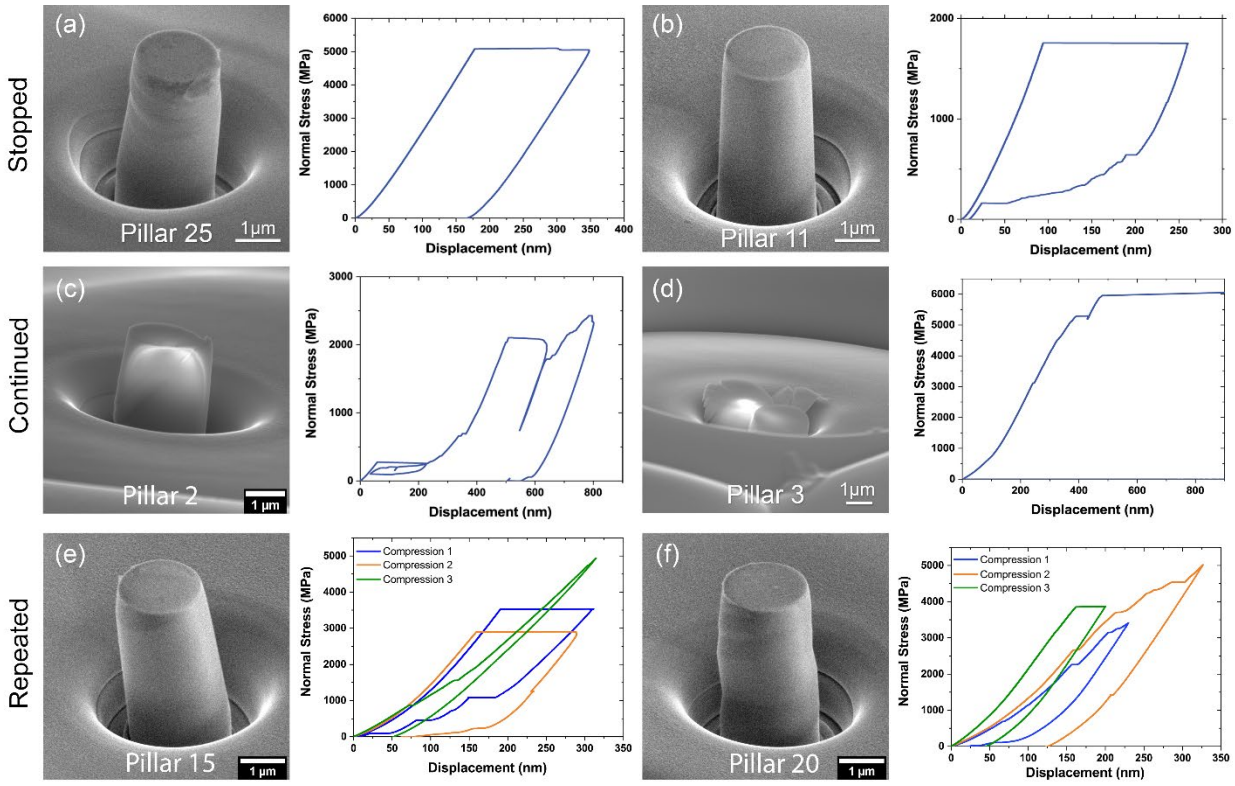

Figure 3.2: Examples of deformed pillars with their respective deformation curves. (a) SEM image of Pillar 25 showing visible shape change corresponding to the large permanent deformation seen in the loading curve. (b) SEM image of Pillar 11 showing no visible shape change, while the loading curve shows recovery of nearly all strain during unloading. (c) SEM image of Pillar 2 for which deformation continued after the initial deformation event shows striations consistent with dislocation plasticity. The loading curve shows numerous large and small deformation events throughout loading. (d) SEM image of Pillar 3 which fractured after exhibiting several relatively small deformation events as seen in the deformation curve. (e) SEM image of Pillar 15 showing shear distortion after three consecutive loadings. The loading curves show a decrease in the normal stress for deformation events during subsequent loading cycles and a decrease in stiffness. (f) SEM image of pillar 20 showing shear distortions after three consecutive loadings. The loading curves show an increase in stress for deformation events during subsequent loadings, and an increase in stiffness.

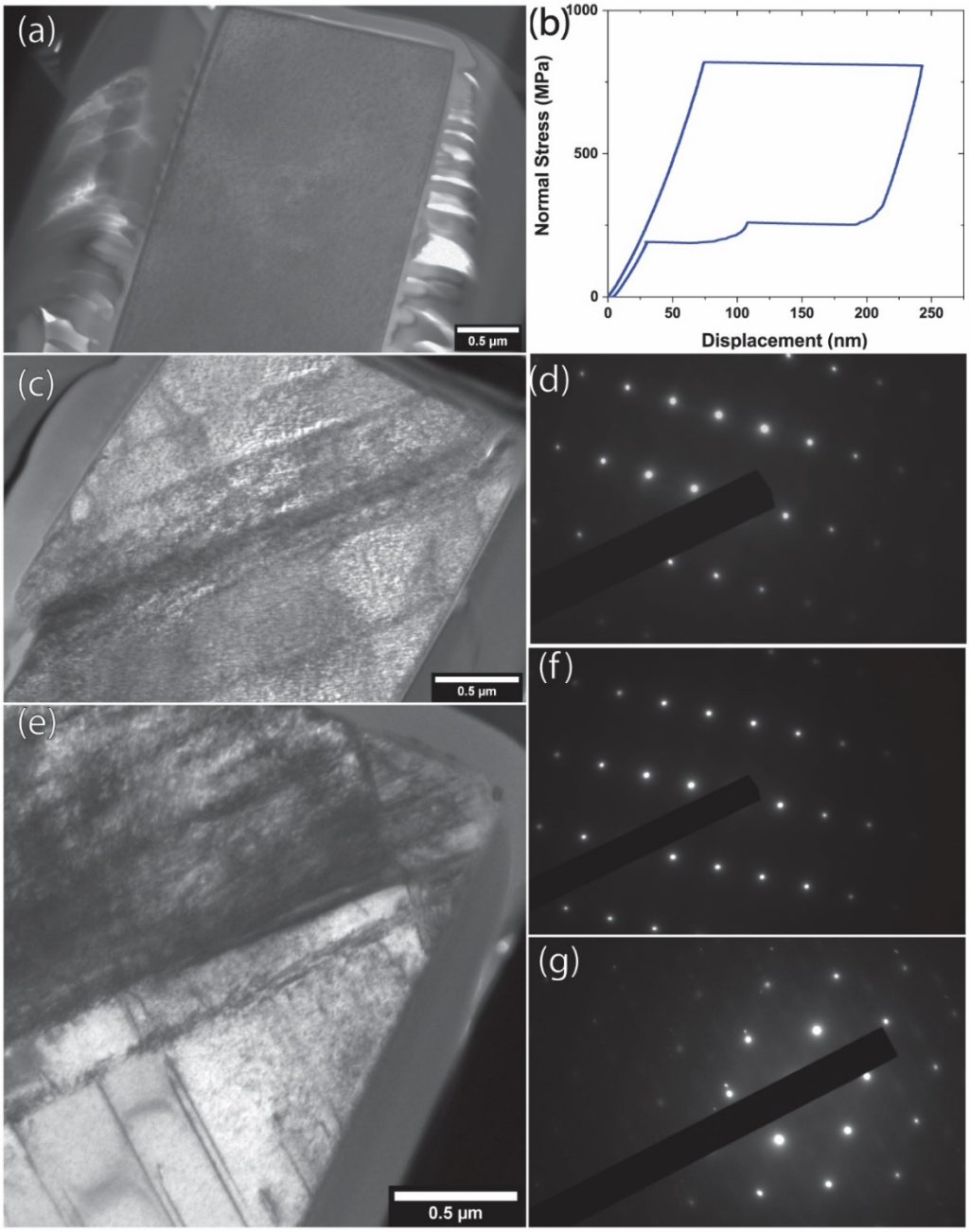

Figure 3.3: TEM images and diffraction patterns of deformed pillars. (a,d) Shows Pillar 9 that experienced nearly complete recovery of deformation upon unloading. The cross-section of the pillar reveals no evidence of remaining twins within the pillar, and the (112) zone axis diffraction pattern shows no spot splitting that would indicate twinning. (b) Stress-displacement curve corresponding to pillar 9 showing that it recovered completely. (c,f) Bright field and selected area diffraction of pillar 2, which exhibited slip traces and permanent deformation. The shearing of the pillar from dislocations can be seen, but the (112) zone axis diffraction pattern again shows no evidence of twinning. (e,g) Bright field and selected area diffraction of pillar 1 which shows evidence of dislocation plasticity as well as twinning.

3.3.3 Resolved Shear Stress and Orientation Dependence

The normal stress at the first deformation event of the first loading cycle for each pillar is tabulated in Table 3.1, along with the out of plane orientation of each pillar (determined via EBSD).

Table 3.1: Compilation of pillar orientation, deformation stress, twin system, Schmid factor, and resolved shear stresses.

Pillar Number	Orientation (hkl)	Deformation Normal Stress (MPa)	Twin System *with a-b excluded	Schmid Factor	Resolved Shear (MPa)
1	(45$\bar{5}$)	1150	(10$\bar{1}$)[101]	0.133	153
2	(132)	277	(110)[$\bar{1}$10]	0.462	128
			*(01$\bar{1}$)[011]	0.336	93.1
3	(16$\bar{1}$)	3115	(011)[01$\bar{1}$]	0.647	2016
4	(322)	2516	(011)[01$\bar{1}$]	0.141	355
5	(52$\bar{2}$)	964	(101)[10$\bar{1}$]	0.529	510
6	(15$\bar{1}$)	2332	(011)[01$\bar{1}$]	0.634	1480
7	(413)	4547	(110)[$\bar{1}$10]	0.445	2025
			*(10$\bar{1}$)[101]	0.352	1602
8	(12$\bar{2}$)	441	(10$\bar{1}$)[101]	0.010	4.28
9	(456)	820	(101)[10$\bar{1}$]	0.092	75.5
10	(65$\bar{1}$)	2216	(10$\bar{1}$)[101]	0.334	721
11	(221)	1756	(011)[01$\bar{1}$]	0.302	530
12	(42$\bar{3}$)	3437	(01$\bar{1}$)[011]	0.055	189
13	(100)	973	(110)[$\bar{1}$10]	0.678	660
			*(101)[10$\bar{1}$]	0.500	487
14	(21$\bar{6}$)	767	(01$\bar{1}$)[0$\bar{1}\bar{1}$]	0.218	167
15	(113)	3522	(011)[0$\bar{1}$1]	0.111	392
16	(014)	4209	(011)[0$\bar{1}$1]	0.526	865
17	(136)	1445	(101)[$\bar{1}$01]	0.178	257
18	(100)	94	(110)[$\bar{1}$10]	0.678	64.0
			*(101)[10$\bar{1}$]	0.500	47.0
19	(124)	768	(101)[$\bar{1}$01]	0.140	108
20	(126)	686	(101)[$\bar{1}$01]	0.218	150
21	(21$\bar{6}$)	375	(01$\bar{1}$)[0$\bar{1}\bar{1}$]	0.218	82.0
22	(013)	1108	(101)[$\bar{1}$01]	0.261	289
23	(116)	748	(101)[$\bar{1}$01]	0.253	189
24	(10$\bar{6}$)	3224	(10$\bar{1}$)[$\bar{1}$0$\bar{1}$]	0.267	860
25	(11$\bar{6}$)	5082	(10$\bar{1}$)[$\bar{1}$0$\bar{1}$]	0.253	1284

It will be assumed that these normal stress values correspond to the initial domain nucleation event for the purposes of the subsequent calculations. The angle of the (001) plane (the direction of the c-axis) with respect to the loading direction was found for each pillar and then the normal stress measured for the initial deformation event in each pillar was then plotted against this misorientation from (001) in Figure 3.5(a). Pillars that recovered are distinguished from those that were permanently deformed. No quantifiable trend can be extracted from the data plotted in Figure 3.5(a) for either of these subsets.

A more thorough analysis, testing a critical resolved shear stress criterion analogous to Schmid's law for domain nucleation has also been performed using the assumptions outlined in Section 2.2. The calculated twin systems, Schmid factors, and resulting resolved shear stresses on those twin systems are given in Table 3.1. It is important to note that several values of Schmid Factor exceed 0.5. This is due to the high tetragonality of this crystal structure leading to angles between planes and crystal directions that are significantly larger than they would be for a cubic crystal structure or even a lower tetragonality ratio. The normal stress for deformation is plotted against these Schmid factors in Figure 3.5(b), again with recovered and permanently deformed pillars being distinguished. Despite the more rigorous analysis, the data in Figure 3.5(a) and Figure 3.5(b) are similarly stochastic. If domain nucleation indeed follows a critical resolved shear stress criterion, the normal stress for nucleation should decrease with increasing Schmid factor, and the calculated resolved shear values should converge to a single value. It is clear from the plots In Figure 3.5 and from the tabulated resolved shear values, that the deformation does not follow a trend with the Schmid factors, nor do the resolved shear stresses converge to a critical value.

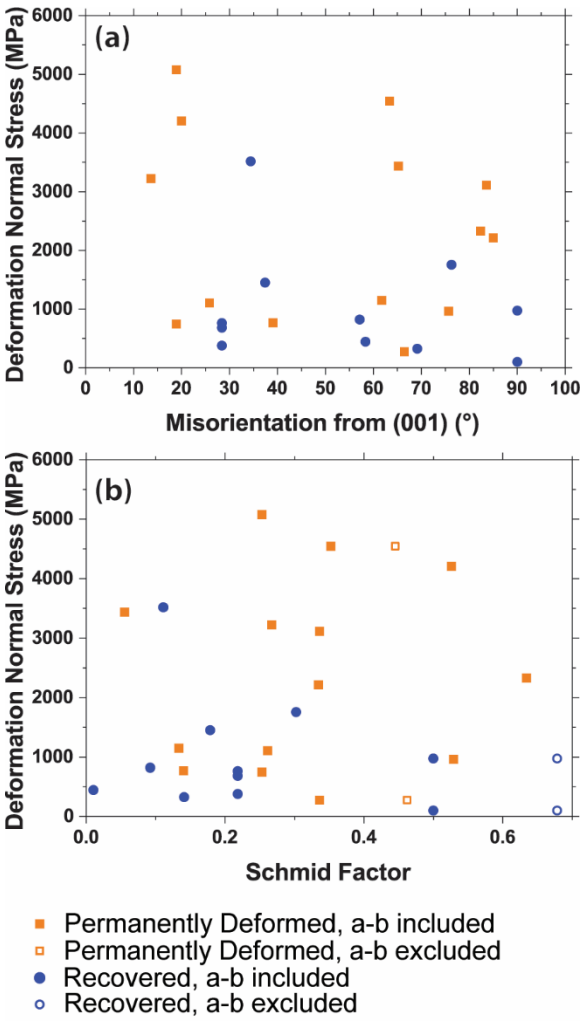

Figure 3.4: Normal stress of deformation plotted against (a) misorientation from the (001) plane normal and (b) Schmid Factor. Schmid factor has been calculated both allowing and disallowing a-b domain transitions.

3.4 Discussion

There are no apparent relationships between misorientation, critical resolved shear stress and the measured normal stress at the onset of deformation. This warrants further discussion of the assumptions underlying the original hypothesis and demands closer evaluation of the active deformation mechanisms at the root of this behavior. Several different modes of deformation have been observed in this study, each of which have implications for the mechanisms associated with single crystal deformation and ferroelastic domain nucleation.

3.4.1 Observed Modes of Deformation

The hypothesis that ferroelastic domain nucleation would follow a critical resolved shear stress criterion was derived from the presiding definition of the coercive stress associated with ferroelasticity. With the exception of Kreher [26] and more recently Landis [27,28], most models describing ferroelastic switching assume that (i) ferroelastic switching occurs at a well-defined stress, e.g. the coercive stress; (ii) that the switching process is discrete (no partial transformations are allowed); and (iii) that once switched, the irreversible strain cannot be reoriented. Landis [28] initially argued and has since demonstrated, e.g. [29], that domain switching may occur over a range of stress levels, incremental transformations are possible and that strain reorientations can take place. These arguments have received greater attention within ferroelectrics, wherein 180º domain switching is commonplace, e.g. [30,31]. Some of these micro-mechanical models have established a direct analog to single crystal metal plasticity and critical resolved shear stress criterion to more accurately describe domain switching [30].

However, even within metallic systems, Schmid's law does not always hold true. Non-Schmid behavior has been identified in several materials for dislocation plasticity as well as for twinning deformation. Notably, non-Schmid behavior of dislocations has been observed in BCC and HCP metals, as well as in intermetallics [32–36]. Non-Schmid twinning behavior has also been seen in HCP materials [37,38]. Often times, such behavior has been attributed to anisotropic dislocation core spreading or other similar mechanisms focused on the nature and behavior of specific dislocation types within a given crystal structure [34–36]. In the current study, such considerations may also be made, but more practically there are likely several interacting or competing factors that give rise to this non-Schmid behavior in ferroelastic CTZ.

First the size of the micropillars and the compressive loading configuration must be considered. Without the constraint and interfaces provided by neighboring grains, the small size of the micropillars imposes a natural cap on the size and distribution of defects within each pillar. The mode I toughness of CTZ is on the order of 53 J/m^2 based on previous characterization [16]. If Griffith's criterion is then used to approximate failure by fracture, assuming a conservative stiffness of 200GPa, the critical flaw size for fracture of CTZ may be approximated as 1.3 μm. Given that all pillars had a diameter of 2μm, such large internal or surface flaws are not possible,

and as a result fracture is suppressed. The probability of fracture is further reduced when considering that the pillars were loaded in compression. Zirconia-based materials typically undergo ferroelastic deformation or fracture before dislocation plasticity at room temperature [39]. However, with fracture largely suppressed on the basis of the length scale, significantly higher stresses can be realized on slip planes as well as the twinning planes. As a result, both dislocation-mediated deformation and twin-mediated deformation are possible, and may be simultaneously (or sequentially) active in a single pillar.

Multiple types of deformation, and combinations thereof, were indeed observed in the pillars compressed in this study. 14 of the 25 pillars in this study maintained some sort of permanent deformation upon unloading. These pillars exhibited evidence of dislocation plasticity, microcracking, as well twinning based deformation and combinations thereof. Some of these pillars experienced partial recovery, such as is seen at the end of the stress-displacement curve for Pillar 2 shown in Figure 3.2(c). In these cases, a combination of twins and dislocations were always observed, but it is assumed that some twins were able to reverse during unloading. Most pillars in this subset did not experience any strain recovery. Several pillars, such as the one shown in Figure 3.2(c) exhibit slip traces characteristic of dislocation plasticity. This indicates that the yield stress was surpassed for that orientation. It is not possible to determine whether such exclusive dislocation-mediated deformation followed Schmid-like behavior without more isolated observations. In many other pillars, such as Pillar 1 shown in Fig 3(e), some combination of dislocation and twin activity was found. Another example of this behavior is seen in Figure 3.6 showing Pillar 7 which contains multiple twins remaining within the pillar after unloading, and no evidence of recovery in the deformation curve. Pillar 7 also exhibits microcracking along with the previously mentioned twinning and dislocation plasticity. The sequence by which these different deformation modes are activated cannot be extracted from post mortem analysis of the microstructure. This greatly obscures any potential relationships between the applied stress and deformation events.

The second subset consists of those pillars that fully recovered following a significant deformation event—*cf.* Figure 3.3(a,b). Twinning deformation has been shown to be reversible in a variety of materials. For example, ferroelastic domain twins in yttria stabilized zirconia are reversible by application of appropriate hysteretic stresses [40] while domains in PZT may be introduced and removed by electrical and mechanical hysteresis [8]. Back switching of ferroelastic

domains simply upon unloading (without negative applied stress) has been documented in ferroelastic ceramics such as La-Sr-Co-Fe oxides [41] and, while not formally ferroelastic, many other so called elastic twinning systems like calcite [42]. Detwinning in HCP, FCC, and BCC metals has also been observed [43–46]. All pillars in this subset exhibited a significant deformation event, eliminating the possibility of a fully elastic process, and dislocation activity would result in permanent strain. Therefore, the complete recovery of strain upon unloading indicates that ferroelastic twinning (and subsequent detwinning) was the dominant deformation mode in this subset. A representative cross-section of a pillar that recovered—*cf.* Figure 3.3(a)—shows no evidence of residual defects within the pillar after recovery. In this study, 11 of the 25 pillars tested experienced full recovery following their initial loading cycle. This subset is differentiated in Figure 3.4, wherein it is clear that there is no relationship between deformation stress, crystal orientation or Schmid factor. This would suggest that twin nucleation exhibits non-Schmid behavior even without competing dislocation plasticity.

3.4.2 Mechanisms of Deformation

Ferroelastic domains often form during a paraelastic to ferroelastic (cubic to tetragonal phase transition for zirconia) phase transition [47,48], which is often discussed as a diffusionless, displacive transition, and results in the complex colony domain structure often observed in polydomain ferroelastic ceramics. Many examples of these domain morphologies have been summarized by Salje [49]. In the case of mechanically nucleated domains, the mechanisms by which the domains nucleate and grow may be different than the displacive mechanism responsible for their formation during a phase transition. Mechanical twin nucleation in metals has been discussed to take place through complex dislocation interactions involving partial dislocations [34,46,50]. There have also been observations of twin nucleation in ionic ceramic structures such as sapphire, which require partial dislocation separation and cross slip [51]. The observations in the current work are not sufficiently exhaustive to precisely determine the mechanism of twin nucleation and growth. Nonetheless, the different morphologies and behaviors during deformation can give some insight on these underlying phenomena.

It is possible that a displacive mechanism is responsible for the deformation twinning that is occurring in these samples. Deformation twinning in ceramics has been described as resulting in abrupt and collective movements of atoms within the entire twin, analogous to displacive

deformation during martensitic transformations [15,52,53]. This type of mechanisms does not distinguish between the nucleation and growth processes for the twins. Previous observations of mechanically nucleated domains in CTZ polycrystals show a modulated ordering of the oxygen sublattice that likely resulted from strain accommodation during large scale twinning [16]. These distortions may be indicative of a displacive mechanical twinning mechanism active in larger scale twins and could result in a pillar deformation morphology schematically depicted as "Mechanism 1" in Figure 3.5. The pillars shown in Figure 3.2(e,f) are characteristic of this morphology. However, for the limited number of pillars with "Mechanism 1" type morphologies, no supporting evidence of the modulated oxygen sublattice could found within the microstructure. Alternatively, if a displacive twinning mechanism occurs, it is assumed to take place without associated dislocation activity. This would result in reversibility with no residual defects unless the domain is otherwise pinned by an intersection with the pillar surface [54]. This type of mechanism may therefore be active in samples that detwin upon unloading and exhibit no residual evidence of dislocation activity.

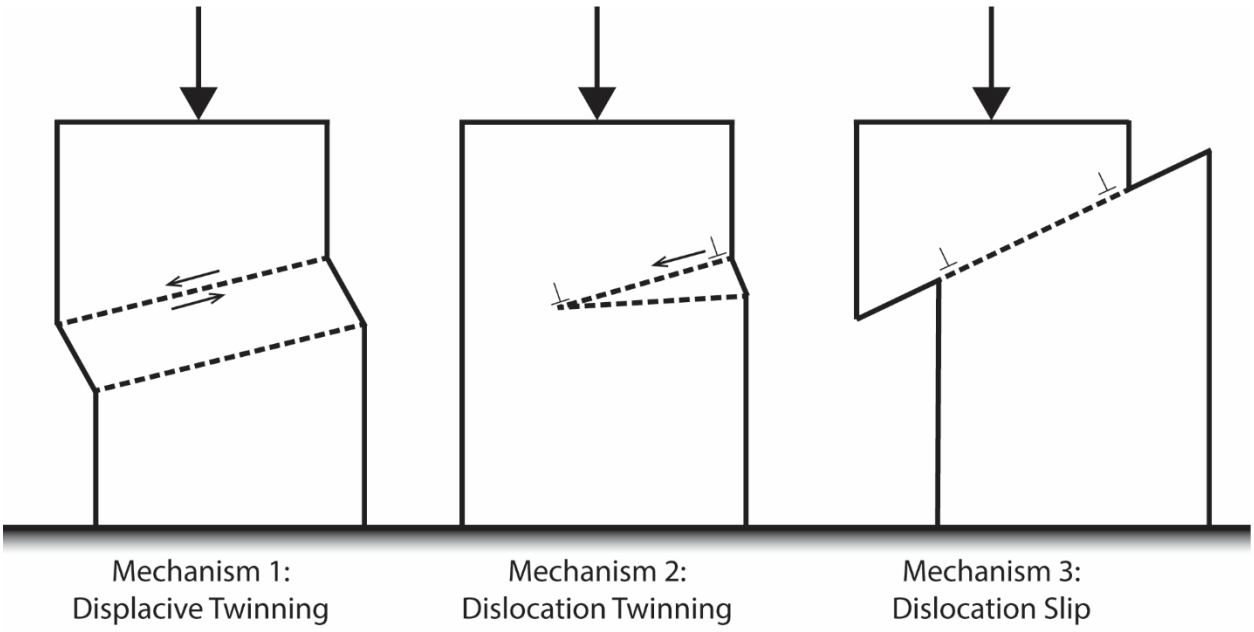

Figure 3.5: Schematic showing morphologies resulting from possible deformation mechanisms including displacive twinning, dislocation mediated twinning, and dislocation slip. Combinations of these mechanisms may be active within the deformed pillars in this study.

Twin nucleation and growth may also take place by a dislocation mediated mechanism, as has been previously described for metals and a handful of ceramics. There have been numerous experimental, theoretical, and simulation-based studies that have illuminated the role of partial

dislocations in twin nucleation. For example, simulations of twin nucleation in FCC aluminum have suggested a partial dislocation interaction mechanism [50], while twinning in HCP metals such as magnesium and titanium has been shown to occur through dislocation interactions at grain boundaries [55,56]. In these ceramic micropillars it is possible that twins nucleate at the pillar surfaces[*] and then propagate via a dislocation mediated mechanism. Many of the domains that have nucleated in this study exhibit a needle-like morphology, schematically depicted as "Mechanism 2" in Figure 3.5. This needle-like morphology has been previously associated with arrays of dislocations and elastic anisotropy [57–59]. In some instances, this type of domain has been reported to detwin [60,61]. Many instances of needle-like domains do however, remain in the pillar microstructure after unloading—*cf* Figure 3.6(a) and (b). These examples are likely the consequence of domain pinning arising from domain interactions with surfaces, neighboring domains, or other defects such as dislocations. It is also possible that when such needle-like domains intersect with a free surface while being subject to a continuously increasing load, the twin boundaries will further separate becoming more parallel and emulating the morphological signature of "Mechanism 1" [62,63].

It is clear that dislocation slip has taken place in some samples in this study, *cf.* Figure 3.2(c) and Figure 3.6. These pillars exhibit distinct slip bands, schematically depicted as "Mechanism 3" in Figure 3.5. Dislocations in YSZ have been observed to form on {100}, (110}, and {111} planes [39,64], but dislocations will only be complete if the Burgers vector lies in the (001) basal plane [39]. Dislocations active outside of the (001) basal plane will be partials, which result in stacking faults in the oxygen sublattice, and may sometimes result in antiphase boundary-like contrast in bright field transmission electron micrographs [4,39]. As noted above, twinning may also arise through the separation of partial dislocation. It is therefore possible that stacking faults generated by partial dislocations on {110} planes may be related to the nucleation mechanism for twinning on these planes. However, the present observations were insufficient to fully deconvolve those complex microstructures containing both significant twinning and dislocation activity such that the full character of dislocations present could be determined.

[*] It cannot be ignored that surface nucleation may be impacted by the pillar preparation via focused ion beam milling. The impact of surface implantation has been widely studied for metallic micropillars. It is, unfortunately, difficult to directly translate these lessons for application in ceramic systems on the basis that radiation damage accumulation in ceramics is highly sensitive to chemistry, crystal structure, and ion energy.

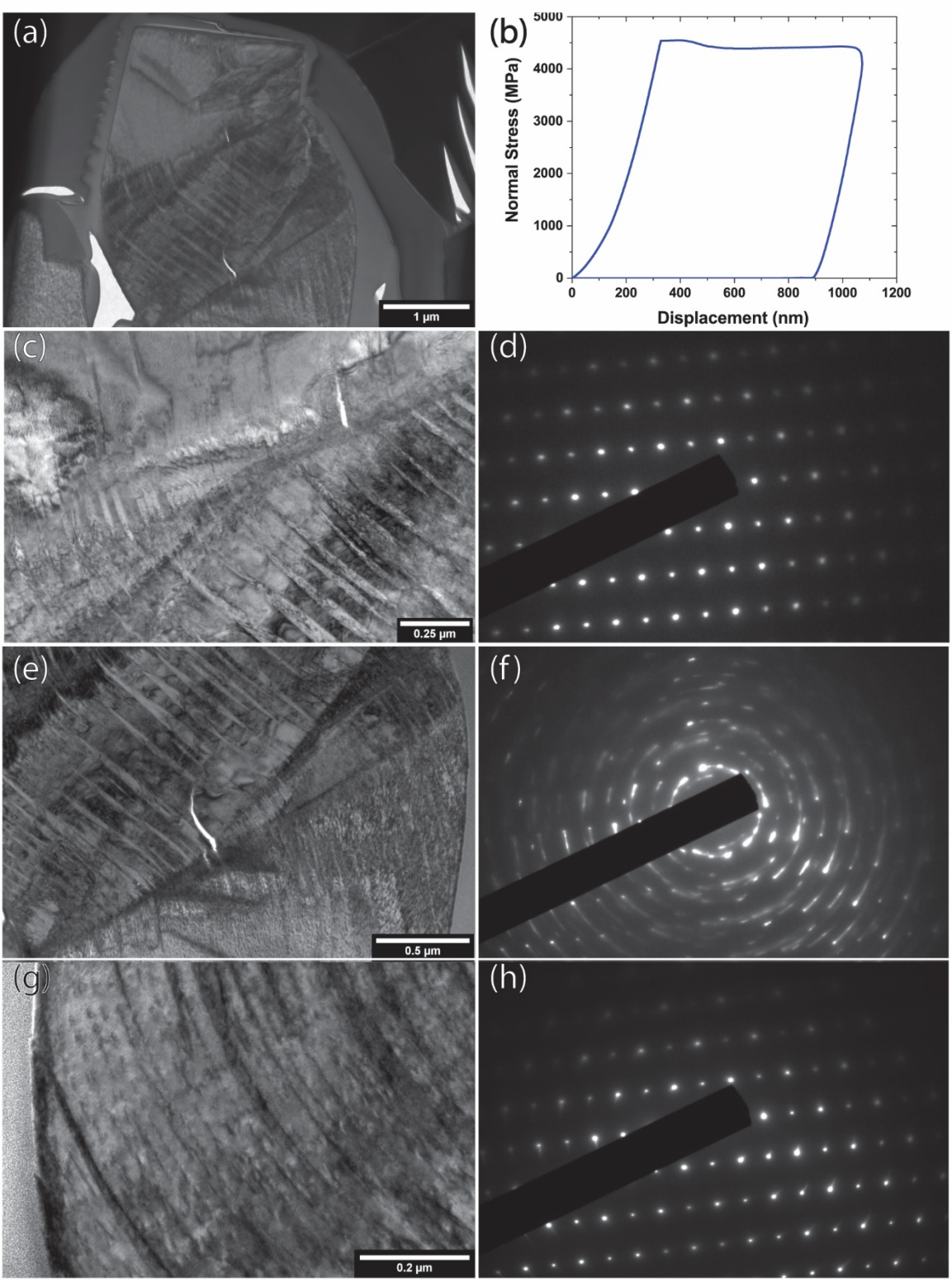

Figure 3.6: Images and diffraction patterns showing deformation of Pillar 7. This Pillar exhibits twinning, dislocation plasticity as well as microcracking. (a,c,e,g) bright field images of the deformed region of Pillar 7. (a) Overview of the deformed Pillar showing large scale twinning, plasticity and microcracking. (b) Stress-displacement curve showing that the deformation occurred

Figure 3.6 (continued): during a single large jump in displacement and no recovery occurred. (c) Needle-like domain nucleated near the top of the deformed region of the Pillar. Contrast within and without the domains indicated high dislocation density. Microcracking is also visible and appears to have dislocations emanating from the tip. (e) Needle-like domains near the bottom of the deformed region. Another "wing crack" shaped microcrack is visible. Domains appear to start and end within the Pillar. (g) Curved boundaries that may indicate antiphase boundaries resulting from dislocation plasticity. Shear steps where dislocations have exited the Pillar are visible. (d, h) Diffraction patterns taken outside the deformed region in the top and bottom of the Pillar, respectively, showing its single crystal, undeformed state. Slight streaking of diffracted spots in (h) indicates plasticity, but not twinning in the Pillar base (f) Diffraction pattern taken within the deformed region showing the presence of multiple additional spots resulting from multiple twins as well as streaking resulting from strain and possible stacking faults.

The potential mechanisms depicted in Figure 3.5 are neither exhaustive nor exclusive. Coexistence, competition or even synergy between these mechanisms are possible in such confined volumes and thus relatively large stresses. The deformation and resulting morphology of Pillar 7, shown in detail in Fig 6, is a good example of this. TEM bright field images of Pillar 7 show that there are multiple needle-like domains of various size nucleated within the Pillar. There is also evidence of significant dislocation plasticity. Diffraction patterns from the center of the Pillar show smearing of the reflections as well as the presence of multiple twin reflections. These characteristics are indicative of lattice distortion arising from the dislocation density and the possible presence of stacking faults in the deformed regions. Microcracks, with the signature wing crack configuration, have formed at the top and bottom interfaces of the deformed region. These wing cracks are likely to have formed during the single large deformation event experienced by Pillar 7 (along with the domain nucleation and dislocation plasticity that occurred). Wing cracks typically form from tensile stress development along inclined defects such as cracks and grain boundaries pre-existing withing a material during compression [65–67]. In this case, however, those defects did not pre-exist but are presumed to have nucleated just prior to the wing crack development. The presence of these cracks illustrates that complex triaxial stresses may develop within even these single crystals during deformation. Evidence of complex, localized stress within such a confined volume also illuminates the potential of path dependent behavior, wherein nucleation of initial defects may strongly influence the development of additional defect features with continued or repeated loading.

Defects, like dislocation or twin boundaries, are expected to accumulate with repeated loading and unloading cycles, thereby providing an additional perspective on the interaction of

these defects. There are several possible scenarios that may arise through such repeated deformation cycles. In one scenario, it would be reasonable to expect that once a ferroelastic domain boundary has been nucleated, the stress necessary to propagate that boundary upon successive loading should be reduced—i.e. the nucleation barrier need only be surpassed once. Pillar 15 in Figure 3.3 seemingly follows this "softening" pathway. The first deformation event occurred above 3.5 GPa, then around 3.0 GPa and finally around 1.5 GPa during the final compression. It is also relevant to note that the Pillar recovers completely, albeit incrementally, after compression #1, but only partially following compression #2. It is reasonable to expect that the domain walls, whether formed via Mechanism #1 or #2, extended across the full diameter of the Pillar during the second cycle, thereby pinning them. As a result, not only is the normal stress much lower for the deformation event during the third cycle, the magnitude of the deformation event is also much smaller. In this case domain-defect(surface) interactions stabilized the domain structure, thereby reducing the backstress for detwinning upon unloading and eliminating the necessity to nucleate the domain boundary in future loading cycles. If, however, different defects are present or accumulated, an alternative "hardening" scenario is possible. In Pillar 20, Figure 3.3(b), the deformation stress increases from just over 2 GPa to nearly 4 GPa in three compression cycles and only incomplete, if any, recovery was observed between each of these. The density of residual defects, whether dislocations, stacking faults, anti-phase boundaries or some form of nanodomains, likely increases with subsequent compressions. Any mobile defect would be increasingly likely to interact with these defects, thereby increasing the applied stress necessary for further deformation.

It is evident that a critical resolved shear stress criterion is insufficient to fully describe the nucleation of ferroelastic domains within such small, unconfined volumes. This is especially true when the nucleation stresses are comparable to those necessary for dislocation activity. As a result, it remains quite difficult to discern any meaningful relationship between single crystal orientation, applied load and deformation behavior in the absence of preexisting ferroelastic domain boundaries. This outcome only emphasizes the need for greater understanding of the role played by highly localized stress fields and the rigid constraint of neighboring grains during deformation. Completely describing and predicting ferroelastic deformation for efficient ferroelastic toughening clearly requires a more complete and complex description of the stress distribution within

polycrystalline ferroelastic ceramics. The first steps towards this goal will be addressed in forthcoming publications.

3.5 Conclusion

A critical resolved shear stress criterion for domain/twin nucleation in ferroelastic CTZ was evaluated within single crystal micropillars. Micropillars of different orientations exhibited drastically different deformation stresses and revealed multiple active types of deformation including ferroelastic domain nucleation, dislocation plasticity, and microcracking. No correlation was found between Pillar crystallographic orientation and the stress at which they deformed, regardless of the deformation types they exhibited. Underlying this non-Schmid deformation behavior, these observations suggest that domain nucleation may occur through different mechanisms such as large scale displacive twinning or dislocation mediated twin nucleation and propagation. Furthermore, domain nucleation may compete more closely with dislocation plasticity at small size scales than previously expected. These results show that ferroelastic domain nucleation is a complex process involving multiple types of potential deformation, and that crystal orientation alone cannot predict ferroelastic deformation behavior, within small, unconstrained volumes.

3.6 References

[1] K. Aizu, Possible Species of "Ferroelastic" Crystals and of Simultaneously Ferroelectric and Ferroelastic Crystals, J. Phys. Soc. Japan. 27 (1969) 387–396. https://doi.org/10.1143/JPSJ.27.387.

[2] C. Mercer, J.R.R. Williams, D.R.R. Clarke, a. G.G. Evans, On a ferroelastic mechanism governing the toughness of metastable tetragonal-prime (t′) yttria-stabilized zirconia, Proc. R. Soc. A Math. Phys. Eng. Sci. 463 (2007) 1393–1408. https://doi.org/10.1098/rspa.2007.1829.

[3] A. V Virkar, J.F. Jue, P. Smith, K. Mehta, K. Prettyman, The role of ferroelasticity in toughening of brittle materials, Phase Transitions. 35 (1991) 27–46. https://doi.org/10.1080/01411599108205204.

[4] D. Baither, M. Bartsch, B. Baufeld, A. Tikhonovsky, A. Foitzik, M. Rühle, U.

Messerschmidt, Ferroelastic and Plastic Deformation of t′-Zirconia Single Crystals, J. Am. Ceram. Soc. 84 (2001) 1755–1762. https://doi.org/10.1111/j.1151-2916.2001.tb00911.x.

[5] K. Mehta, A. V. Virkar, Fracture Mechanisms in Ferroelectric-Ferroelastic Lead Zirconate Titanate (Zr: Ti=0.54:0.46) Ceramics, J. Am. Ceram. Soc. 73 (1990) 567–574. https://doi.org/10.1111/j.1151-2916.1990.tb06554.x.

[6] A. Kolleck, G.A. Schneider, F.A. Meschke, R-Curve Behavior of BaTiO3 - and PZT Ceramics Under the Influence of an Electric Filed Applied Parallel to the Crack Front, Acta Mater. 48 (2000) 4099–4113. https://doi.org/10.1016/S1359-6454(00)00198-1.

[7] F. Meschke, A. Kolleck, G.A. Schneider, R-curve behaviour of BaTiO3 due to stress-induced ferroelastic domain switching, J. Eur. Ceram. Soc. 17 (1997) 1143–1149. https://doi.org/10.1016/s0955-2219(96)00211-7.

[8] P. Gao, J. Britson, C.T. Nelson, J.R. Jokisaari, C. Duan, M. Trassin, S.H. Baek, H. Guo, L. Li, Y. Wang, Y.H. Chu, A.M. Minor, C.B. Eom, R. Ramesh, L.Q. Chen, X. Pan, Ferroelastic domain switching dynamics under electrical and mechanical excitations, Nat. Commun. 5 (2014) 1–8. https://doi.org/10.1038/ncomms4801.

[9] K. Kim, J.E. Huber, In situ observation of ferroelastic domain evolution in a near-morphotropic Pb(Zr,Ti)O3ceramic by piezoresponse force microscopy, J. Eur. Ceram. Soc. 35 (2015) 1459–1468. https://doi.org/10.1016/j.jeurceramsoc.2014.11.027.

[10] B. Baufeld, D. Baither, U. Messerschmidt, M. Bartsch, A.H. Foitzik, M. Rühle, Ferroelasticity of t‘-Zirconia: II, In situ Straining in a High-Voltage Electron Microscope, J. Am. Ceram. Soc. 80 (1997) 1699–1705. https://doi.org/10.1111/j.1151-2916.1997.tb03041.x.

[11] G. Arlt, Twinning in ferroelectric and ferroelastic ceramics: stress relief, J. Mater. Sci. 25 (1990) 2655–2666. https://doi.org/10.1007/BF00584864.

[12] D. Baither, B. Baufeld, U. Messerschmidt, A.H. Foitzik, M. Rühle, Ferroelasticity of t‘-Zirconia: I, High-Voltage Electron Microscopy Studies of the Microstructure in Polydomain Tetragonal Zirconia, J. Am. Ceram. Soc. 80 (1997) 1691–1698. https://doi.org/10.1111/j.1151-2916.1997.tb03040.x.

[13] G.R. Barsch, J.A. Krumhansl, Twin Boundaries in Ferroelastic Media without Interface Dislocations, Phys. Rev. Lett. 53 (1984) 1069–1072. https://doi.org/10.1103/PhysRevLett.53.1069.

[14] M.S. Szczerba, T. Bajor, T. Tokarski, Is there a critical resolved shear stress for twinning in face-centred cubic crystals?, Philos. Mag. 84 (2004) 481–502. https://doi.org/10.1080/14786430310001612175.

[15] J.K. Shang, X. Tan, Indentation-induced domain switching in Pb(Mg1/3Nb2/3)O3–PbTiO3 crystal, Acta Mater. 49 (2001) 2993–2999.

[16] J.A. Krogstad, M. Lepple, C.G. Levi, Opportunities for improved TBC durability in the CeO2-TiO2-ZrO2 system, Surf. Coatings Technol. 221 (2013) 44–52. https://doi.org/10.1016/j.surfcoat.2013.01.026.

[17] A. Lai, Z. Du, C.L. Gan, C.A. Schuh, Shape Memory and Superelastic Ceramics at Small Scales, Science (80-.). 341 (2013) 1505 LP – 1508. https://doi.org/10.1126/science.1239745.

[18] X.M. Zeng, A. Lai, C.L. Gan, C.A. Schuh, Crystal orientation dependence of the stress-induced martensitic transformation in zirconia-based shape memory ceramics, Acta Mater. 116 (2016) 124–135. https://doi.org/10.1016/j.actamat.2016.06.030.

[19] E. Camposilvan, M. Anglada, Size and plasticity effects in zirconia micropillars compression, Acta Mater. 103 (2016) 882–892. https://doi.org/10.1016/j.actamat.2015.10.047.

[20] E. Camposilvan, M. Anglada, Micropillar compression inside zirconia degraded layer, J. Eur. Ceram. Soc. 35 (2015) 4051–4058. https://doi.org/10.1016/j.jeurceramsoc.2015.04.017.

[21] S. Korte, W.J. Clegg, Micropillar compression of ceramics at elevated temperatures, Scr. Mater. 60 (2009) 807–810. https://doi.org/10.1016/j.scriptamat.2009.01.029.

[22] M.J. Mayo, Synthesis and applications of nanocrystalline ceramics, Mater. Des. 14 (1993) 323–329.

[23] D.W. Hogan, D.J. Dyson, Angles between planes in the hexagonal and tetragonal crystal systems, Micron (1969). 2 (1970) 59–61. https://doi.org/10.1016/0047-7206(70)90045-2.

[24] J. Lefevre, Different Structural Modifications of Fluorite Type Phases in Zirconium or Hafnium Oxide Based Systems, Ann. Chim.(Paris). 8 (1963) 117–149.

[25] J.A. Krogstad, Phase Stability of Zirconia-Based Thermal Barrier Coatings, University of California, Santa Barbara, 2012.

[26] W.S. Kreher, Influence of domain switching zones on the fracture toughness of ferroelectrics, J. Mech. Phys. Solids. 50 (2002) 1029–1050. https://doi.org/https://doi.org/10.1016/S0022-5096(01)00110-7.

[27] C.M. Landis, On the Strain Saturation Conditions for Polycrystalline Ferroelastic Materials , J. Appl. Mech. 70 (2003) 470–478. https://doi.org/10.1115/1.1600472.

[28] C.M. Landis, On the fracture toughness of ferroelastic materials, J. Mech. Phys. Solids. 51 (2003) 1347–1369. https://doi.org/https://doi.org/10.1016/S0022-5096(03)00065-6.

[29] J. Sheng, C.M. Landis, Toughening due to domain switching in single crystal ferroelectric materials, Int. J. Fract. 143 (2007) 161–175. https://doi.org/10.1007/s10704-007-9056-7.

[30] J. e. Huber, N. a. Fleck, C.M. Landis, R.M. McMeeking, A constitutive model for ferroelectric polycrystals, J. Mech. Phys. Solids. 47 (1999) 1663–1697. https://doi.org/https://doi.org/10.1016/S0022-5096(98)00122-7.

[31] J. Roedel, W.S. Kreher, Modeling of domain wall contribution to the effective properties of polycrystalline ferroelectric ceramics, in: C.S. Lynch (Ed.), Smart Struct. Mater. 2000 Act. Mater. Behav. Mech., SPIE, 2000: pp. 353–362. https://doi.org/10.1117/12.388219.

[32] H. Lim, C.R. Weinberger, C.C. Battaile, T.E. Buchheit, Application of generalized non-Schmid yield law to low-temperature plasticity in bcc transition metals, Model. Simul. Mater. Sci. Eng. 21 (2013) 0–23. https://doi.org/10.1088/0965-0393/21/4/045015.

[33] P. Steinmann, E. Kuhl, E. Stein, Aspects of non-associated single crystal plasticity: Influence of non-Schmid effects and localization analysis, Int. J. Solids Struct. 35 (1998) 4437–4456. https://doi.org/10.1016/S0020-7683(97)00241-2.

[34] T. Tinga, W.A.M. Brekelmans, M.G.D. Geers, Cube slip and non-Schmid effects in single crystal Ni-base superalloys, Model. Simul. Mater. Sci. Eng. 18 (2010). https://doi.org/10.1088/0965-0393/18/1/015005.

[35] A. Patra, T. Zhu, D.L. McDowell, Constitutive equations for modeling non-Schmid effects in single crystal bcc-Fe at low and ambient temperatures, Int. J. Plast. 59 (2014) 1–14. https://doi.org/10.1016/j.ijplas.2014.03.016.

[36] Q. Qin, J.L. Bassani, Non-Schmid yield behavior in single crystals, J. Mech. Phys. Solids. 40 (1992) 813–833.

[37] C. Lou, X. Zhang, Y. Ren, Non-Schmid-based {10-12} twinning behavior in polycrystalline magnesium alloy, Mater. Charact. 107 (2015) 249–254. https://doi.org/https://doi.org/10.1016/j.matchar.2015.07.022.

[38] C.D. Barrett, H. El Kadiri, M.A. Tschopp, Breakdown of the Schmid law in homogeneous and heterogeneous nucleation events of slip and twinning in magnesium, J. Mech. Phys. Solids. 60 (2012) 2084–2099. https://doi.org/https://doi.org/10.1016/j.jmps.2012.06.015.

[39] U. Messerschmidt, D. Baither, B. Baufeld, M. Bartsch, Plastic deformation of zirconia single crystals: A review, Mater. Sci. Eng. A. 233 (1997) 61–74. https://doi.org/10.1016/s0921-5093(97)00050-6.

[40] K.M. Prettyman, J.F. Jue, A. V Virkar, C.R. Hubbard, O.B. Cavin, M.K. Ferber, Hysteresity effects in 3 mol% yttria-doped zirconia (t'-phase), J. Mater. Sci. 27 (1992) 4167–4174. https://doi.org/10.1007/BF01105121.

[41] W. Araki, J. Malzbender, Ferroelastic deformation of La0.58Sr0.4Co0.2Fe0.8O3-δ under uniaxial compressive loading, J. Eur. Ceram. Soc. 33 (2013) 805–812. https://doi.org/10.1016/j.jeurceramsoc.2012.10.035.

[42] H. Kaga, J.J. Gilman, Twinning and Detwinning in Calcite, J. Appl. Phys. 40 (1969) 3196–3207. https://doi.org/10.1063/1.1658166.

[43] B. Li, H. El Kadiri, X.Y. Zhang, S.N. Mathaudhu, Q. Ma, Structural Origin of Reversible Twinning, Non-Schmid Effect, Incoherent Twin Boundaries and Texture in Hexagonal Close-Packed Metals BT - Magnesium Technology 2012, in: S.N. Mathaudhu, W.H.

Sillekens, N.R. Neelameggham, N. Hort (Eds.), Springer International Publishing, Cham, 2016: pp. 105–110. https://doi.org/10.1007/978-3-319-48203-3_20.

[44] B.Q. Li, M.L. Sui, B. Li, E. Ma, S.X. Mao, Reversible Twinning in Pure Aluminum, Phys. Rev. Lett. 102 (2009) 205504. https://doi.org/10.1103/PhysRevLett.102.205504.

[45] S. Li, X. Ding, J. Deng, T. Lookman, J. Li, X. Ren, J. Sun, A. Saxena, Superelasticity in bcc nanowires by a reversible twinning mechanism, Phys. Rev. B. 82 (2010) 205435. https://doi.org/10.1103/PhysRevB.82.205435.

[46] J. Wang, L. Liu, C.N. Tomé, S.X. Mao, S.K. Gong, Twinning and De-twinning via Glide and Climb of Twinning Dislocations along Serrated Coherent Twin Boundaries in Hexagonal-close-packed Metals, Mater. Res. Lett. 1 (2013) 81–88. https://doi.org/10.1080/21663831.2013.779601.

[47] J. Sapriel, Domain-wall orientations in ferroelastics, Phys. Rev. B. 12 (1975) 5128–5140. https://doi.org/10.1103/PhysRevB.12.5128.

[48] V.K. Wadhawan, Ferroelasticity and related properties of crystals, Phase Transitions. 3 (1982) 3–103. https://doi.org/10.1080/01411598208241323.

[49] E.K.H. Salje, Ferroelastic Materials, Annu. Rev. Mater. Res. 42 (2012) 265–283. https://doi.org/10.1146/annurev-matsci-070511-155022.

[50] B. Li, B.Y. Cao, K.T. Ramesh, E. Ma, A nucleation mechanism of deformation twins in pure aluminum, Acta Mater. 57 (2009) 4500–4507. https://doi.org/10.1016/j.actamat.2009.06.014.

[51] A.H. Heuer, K.P.D. Lagerlöf, J. Castaing, Slip and twinning dislocations in sapphire (α-Al2O3), Philos. Mag. A. 78 (1998) 747–763. https://doi.org/10.1080/01418619808241934.

[52] M. Science, Deformation of Ceramic Materials, Deform. Ceram. Mater. (1975). https://doi.org/10.1007/978-1-4613-4431-5.

[53] W.M. Kriven, Displacive Transformations and their Applications in Structural Ceramics, Le J. Phys. IV. 05 (1995) C8-101-C8-110. https://doi.org/10.1051/jp4:1995811.

[54] R.E. Cooper, F.P. Bowden, Kinetics of elastic twinning in calcite, Proc. R. Soc. London. Ser. A. Math. Phys. Sci. 270 (1962) 525–537. https://doi.org/10.1098/rspa.1962.0242.

[55] J. Wang, I.J. Beyerlein, C.N. Tomé, An atomic and probabilistic perspective on twin nucleation in Mg, Scr. Mater. 63 (2010) 741–746. https://doi.org/10.1016/j.scriptamat.2010.01.047.

[56] L. Wang, Y. Yang, P. Eisenlohr, T.R. Bieler, M.A. Crimp, D.E. Mason, Twin Nucleation by Slip Transfer across Grain Boundaries in Commercial Purity Titanium, Metall. Mater. Trans. A. 41 (2009) 421. https://doi.org/10.1007/s11661-009-0097-6.

[57] Z. Jin, T.R. Bieler, An in-situ observation of mechanical twin nucleation and propagation in TiAl, Philos. Mag. A. 71 (1995) 925–947. https://doi.org/10.1080/01418619508236229.

[58] T.E. Mitchell, J.P. Hirth, The shape, configuration and stress field of twins and martensite plates, Acta Metall. Mater. 39 (1991) 1711–1717. https://doi.org/https://doi.org/10.1016/0956-7151(91)90260-8.

[59] E.K.H. Salje, A. Buckley, G. van Tendeloo, Y. Ishibashi, G.L. Nord, Needle twins and right-angled twins in minerals; comparison between experiment and theory, Am. Mineral. 83 (1998) 811–822. https://doi.org/10.2138/am-1998-7-813.

[60] N. Zárubová, Y. Ge, O. Heczko, S.-P. Hannula, In situ TEM study of deformation twinning in Ni–Mn–Ga non-modulated martensite, Acta Mater. 61 (2013) 5290–5299. https://doi.org/https://doi.org/10.1016/j.actamat.2013.05.020.

[61] T.L. Baker, K.T. Faber, D.W. Readey, Ferroelastic Toughening in Bismuth Vanadate, J. Am. Ceram. Soc. 74 (1991) 1619–1623. https://doi.org/10.1111/j.1151-2916.1991.tb07148.x.

[62] J. Novak, U. Bismayer, E.K.H. Salje, Simulated equilibrium shapes of ferroelastic needle domains, J. Phys. Condens. Matter. 14 (2002) 657–664. https://doi.org/10.1088/0953-8984/14/3/332.

[63] E.K.H. Salje, S.A. Hayward, W.T. Lee, Ferroelastic phase transitions: structure and microstructure, Acta Crystallogr. Sect. A. 61 (2005) 3–18.

https://doi.org/10.1107/S0108767304020318.

[64] N. Zhang, M. Asle Zaeem, Effects of specimen size and yttria concentration on mechanical properties of single crystalline yttria-stabilized tetragonal zirconia nanopillars, J. Appl. Phys. 122 (2017). https://doi.org/10.1063/1.4991339.

[65] M. Adams, G. Sines, Crack Extension from flaws in a brittle material subjected to compression, Tectonophysics. 49 (1978) 97–118. https://doi.org/10.1016/0040-1951(78)90099-9.

[66] N.P. Cannon, E.M. Schulson, T.R. Smith, H.J. Frost, Wing cracks and brittle compressive fracture, Acta Metall. Mater. 38 (1990) 1955–1962. https://doi.org/10.1016/0956-7151(90)90307-3.

[67] A. V. Dyskin, L.N. Germanovich, K.B. Ustinov, A 3-D model of wing crack growth and interaction, Eng. Fract. Mech. 63 (1999) 81–110. https://doi.org/10.1016/S0013-7944(96)00115-4.

CHAPTER 4

INFLUENCE OF GRAIN SIZE AND MICROSTRUCTURAL CONSTRAINT ON FERROELASTIC DOMAIN NUCLEATION

A focus of this research was to evaluate the influence of microstructure on ferroelastic deformation in ceramics. This evaluation was done not only in isolated single crystals but also in polycrystalline microstructures that are more similar to those used in engineering applications. In this chapter, the effect of several variables on ferroelastic domain nucleation in bulk polycrystalline microstructures was examined, and work done to evaluate the second main hypothesis outlined in section 1.6 of this dissertation will be discussed. This chapter will focus on crystal size, microstructural constraint, and stress state as variables influencing domain nucleation. Statistics were collected on the influence of grain size on ferroelastic domain nucleation in polycrystals. The behavior observed in polycrystals can then be combined with the insight gained about mechanisms active in single crystals to connect microscale and macroscale understanding of ferroelastic deformation.

4.1 Introduction

Ceramic materials such as tetragonal zirconia have been shown to exhibit increased toughness due to ferroelastic domain nucleation and motion. Ferroelasticity provides an opportunity for increasing the intrinsic toughness of ceramics used in a variety of structural and electrical applications [1–8]. However, it is not yet fully understood how different microstructural features influence this deformation, especially in regard to the domain nucleation behavior. To fully take advantage of the intrinsic toughening that ferroelastic deformation provides, microstructural features that promote significant ferroelastic deformation rather than fracture must be identified and controlled.

To design toughened microstructures, it is important to understand how the microscale behavior of ferroelastic deformation influences the bulk deformation and toughening behavior. At the microscale, the colony structure of domains and how domains evolve in single crystals has been well studied, as has the development of ferroelastic domains within fracture process zones [5,9–12]. However, there has been less discussion about domain nucleation behavior in polycrystals outside of fracture process zone formation. Many analyses have also been done

evaluating the bulk mechanical response and toughness of ferroelastic polycrystals [6,13–18]. Several studies that have characterized the fracture of ferroelastics have even noted the effect that microstructure has on the toughness, but it has been difficult to deconvolute the effect that the microstructure has on the increased toughness from other toughening mechanisms such crack bridging and crack deflection [3,6,19]. The effect that specific microstructural variables have on the extent of ferroelastic deformation must first be isolated in order to control them when designing microstructures.

In this study, the effect that grain size has on domain nucleation behavior was examined in polycrystals. The intent was not to characterize the toughness or the characteristics of a fracture process zone, but rather to highlight the specific effect that grain size has on the domain nucleation behavior. The conformation of domains that nucleate within grains was also examined. The domain nucleation behavior was also observed using in situ TEM nanopillar compression such that stresses associated with domain nucleation at small scales could be evaluated.

4.2 Experimental Methods

Tetragonal phase CTZ nanopowders were synthesized using a reverse-coprecipitation synthesis procedure outlined in previous literature [8,20]. The crystalline powders were pressed into green body pellets with 10 mm diameters. The pellets were then sintered in a box furnace at 1350°C for times ranging from 1 hour to 231 hours to control final grain size. Pellets were polished using diamond lapping films and colloidal alumina to a surface finish of 20nm. The pellets were then thermally etched such that grain boundaries could be distinguished.

Microindentation was used to locally deform the polycrystals and induce domain nucleation in grains surrounding the indents. Both spherical Hertzian and pyramidal Vickers indentation were used. Images of the indents and surrounding microstructure were collected using a JEOL 7000F scanning electron microscope. A Keyence VK-X1000 3D laser scanning confocal microscope was used to collect area profilometry data of the sample surface surrounding the indents. An FEI Helios focused ion beam was used to lift out samples from the deformed regions surround the Vickers indents for transmission electron microscopy, which done in a JEOL 2010 TEM. Single crystal nanopillars all having approximately the same orientation were also fabricated in the FEI Helios FIB and deformed inside the JEOL 2010 TEM using a Hysitron PI-95 TEM Picoindenter equipped with a 1 μm diamond flat punch indenter. The orientation of the grains from

which the pillars were fabricated was determined using an Oxford HKL EBSD system prior to FIB milling.

To collect meaningful statistics on grain sizes associated with domain nucleation, a trainable Weka segmentation plugin for FIJI (imagej) was used to identify grains and grain boundaries in the SEM micrographs. The segmentation was then used to threshold images for grain size analysis such that a very large number of grains in multiple images could be analyzed to determine grain size distributions for the undeformed grains, twinned grains, and nearest neighbors to twin grains. The "analyze particles" feature in imagej was used to measure Feret diameters for all these subsets of grains. Furthermore, for grains that twinned, two Feret diameters were measured. One diameter was measured parallel to twin boundaries that formed while the other diameter was measured perpendicular to the twin boundaries. This was done such that the effect of the grain shape on twin nucleation could be evaluated.

4.3 Results

Pellets with two different grain size distributions were indented to nucleate twins within the polycrystals. Initially both spherical Hertzian indentation as well as pyramidal Vickers indentations were used. The surfaces of pellets that were indented by each type of contact were examined using SEM and can be seen in Figure 4.1. It was found that only Vickers indents resulted in twin nucleation at the surface. Therefore, Vickers indentation was the method selected to deform the samples for grain size analysis.

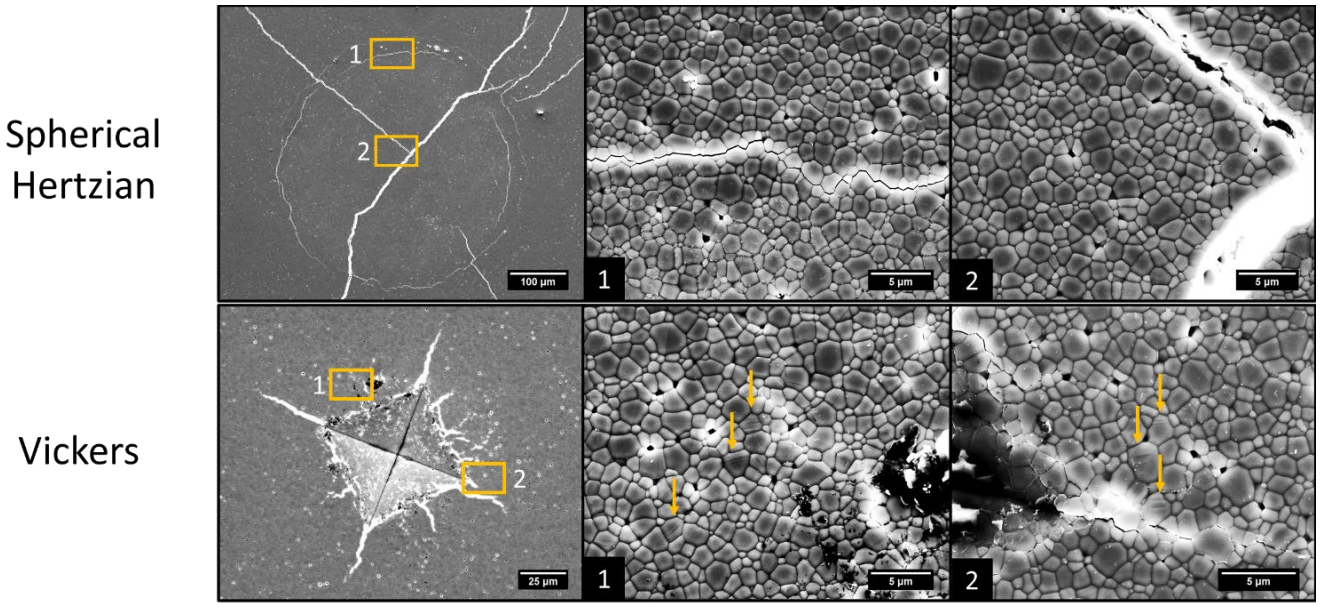

Figure 4.1: SEM images of spherical Hertzian indents which did not induce twinning at the surface, and Vickers indentation which did produce twinning at the surface.

4.3.1 Grain Size Distributions

For each sample, the grain size distribution was measured in three ways: once for the overall grain size distribution, another for the subset of grains that had twins nucleate within then, and another time for grains that neighbored grains with twins, but did not themselves have twins. These subsets are called the grain size, twinned grain size, and nearest neighbor size, respectively. Using the particle size analysis tool built into imagej, large numbers of grains were measured to generate distributions of grain sizes for these subsets. For sample 1, 3045 grains were analyzed, while 14658 were analyzed for the finer grained sample 2. Histograms of each subset for the two different grain size samples have been overlaid in Figure 4.2, and the average and standard deviation for each distribution is given in Table 4.1. Two sample t-tests were performed showing that each subset was significantly different from the overall grain size for each sample, for which the p values are given in Table 4.1. Comparing the means of each distribution, sample 1 twinned grains were 8.75% larger on average than the overall mean, while nearest neighbors were 17.8% smaller than the overall mean. For sample 2 the differences are even greater, with twinned grains 23.3% larger and nearest neighbors 25.2% smaller than the overall mean.

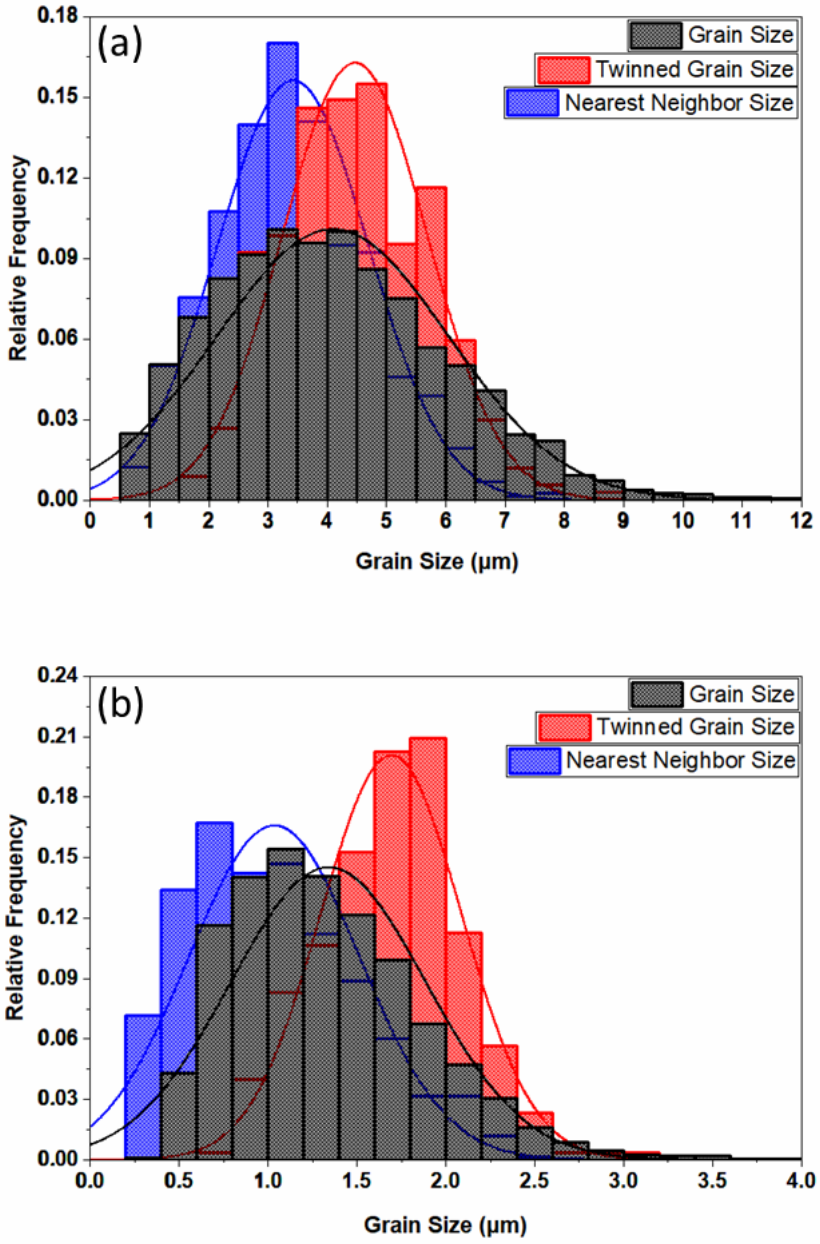

Figure 4.2: a) Histograms of the overall grains size distribution, the subset of grains that exhibited twinning, and the subset of grains that are nearest neighbors to twinned grains but did not contain twins. b) Same three distributions for sample 2 that had a smaller overall grain size distribution.

Table 4.1: Means for the different grain size distributions are displayed alongside the standard deviations in parentheses. To test whether each distribution is statistically different, t-test statistics for difference of means (equal variance assumed) are given for each sample. The p values for each t-test indicate that for both samples, the mean twinned grain size and mean nearest neighbor grain sizes are statistically different from the overall mean grain size.

Sample	Grain size (μm)	Twinned grain size (μm)	Nearest neighbor grain size (μm)	t-test p value Grain size vs. twinned Significance level 0.05	t-test p value Grain size vs. neighbors Significance level 0.05
1	4.094(1.953)	4.469(1.226)	3.425(1.277)	$5.9*10^{-4}$	$3.5*10^{-18}$
2	1.340(0.550)	1.693(0.398)	1.036(0.481)	$1.7*10^{-28}$	$2.8*10^{-40}$

The Feret diameters of the twinned grains taken parallel and perpendicular to twin boundaries were also tracked. The distributions of parallel and perpendicular diameters are shown in Figure 4.3. The perpendicular Feret diameters are on average slightly larger than parallel Feret diameters. However, when performing a two sample t-test to determine if the distributions are significantly different, the resulting p-value indicates that the distributions are not significantly different.

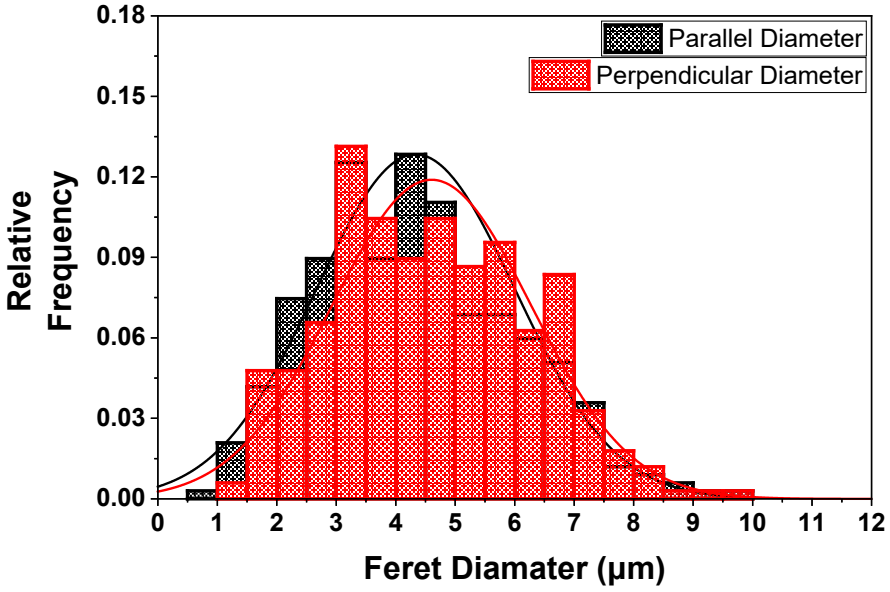

Figure 4.3: Feret diameters of all of the twinned grains in sample 1 measured perpendicular to twin boundaries and parallel to twin boundaries.

4.3.2 Characteristics of Deformation and Domain Conformations

Profilometry data was collected surrounding the indents. Pileup can be observed surrounding the indents, primarily along the flat edges of the Vickers impression, as can be seen in the height map shown in Figure 4.4. The areas surrounding indents were segmented into regions along the flat faces and out from the corners of the indent, as shown in Figure 4.4(a), so that the twin density and maximum pileup heights in these regions may be compared. The twin densities in all the edge and corner regions for indents in sample 1 are compiled in Table 4.2. Table 4.2 also shows the average of the maximum pileup heights measured for both edge and corner regions across all the indents. The twin densities in edge and corner regions have been plotted against maximum pileup height in each individual region as shown in Figure 4.5 and are shown along with their Pearson's r correlation linear trendlines. The Pearson's r and p values for those correlations are also given in Table 4.2. The r and p values indicate that there is no trend between maximum pileup height and twin density for neither edge nor corner regions.

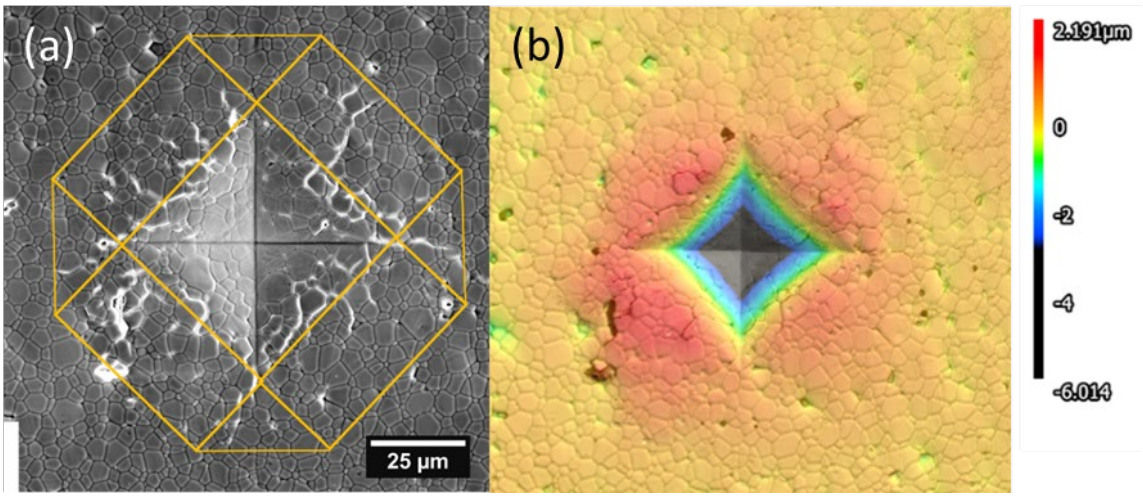

Figure 4.4: (a) image of a Vickers indent showing the segmentation of regions surrounding the indent into edge and corner regions. (b) height map overlaid on an image of the same Vickers indent showing pileup along the indent edges.

Table 4.2: Average twin density, average maximum pileup height, and Pearson's correlation parameters for edge and corner regions surrounding indents in sample 1.

Quantity	Edges	Corners
Average Twin Density (twins/μm^2)	0.016	0.007
Average Maximum Pileup Height (μm)	1.94	1.71
Pearson's r	0.40	0.02
Correlation p value	0.12	0.93

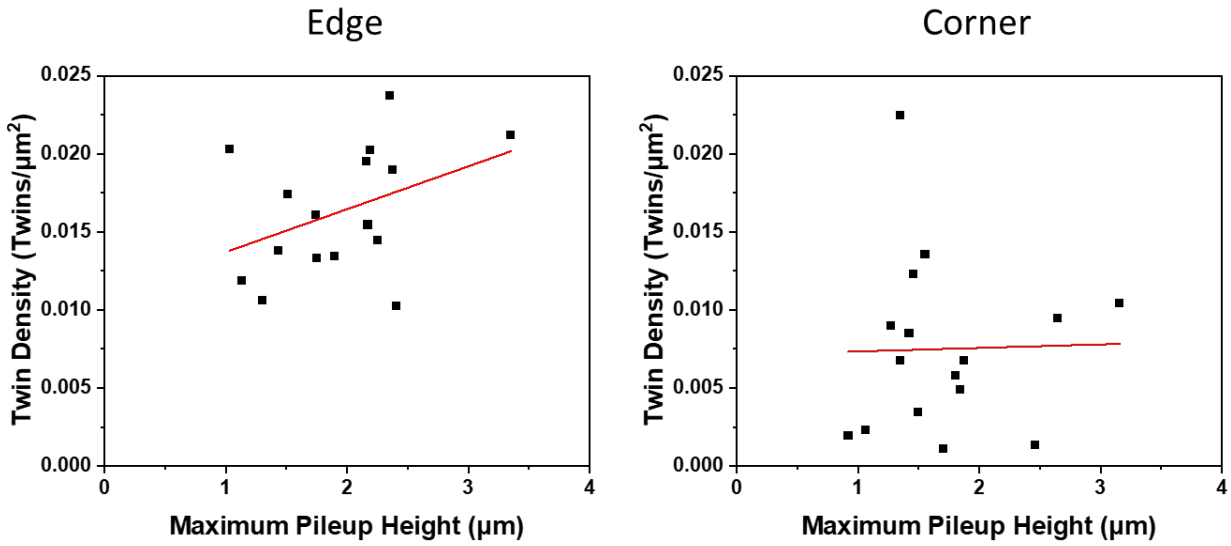

Figure 4.5: Plots showing the twin density calculated in each region plotted against the maximum pileup height observed in each region. Trendlines for both edge and corner regions show that there is no correlation between maximum pileup and twin density.

SEM images of the conformation of the twins have also been collected. Representative images of some domain conformations are shown in Figure 4.6. In some cases, twins appear to propagate through grain boundaries or nucleate similarly oriented twins in the neighboring grain. A particularly common occurrence is that twins appear to propagate from triple junctions, where multiple grain boundaries meet. Larger grains may also exhibit multiple twins that propagate in different directions, often from multiple triple junctions. Twins frequently propagate entirely through the grain they nucleate within, however, there are also cases where twins appear to arrest mid grain (Figure 4.6(a)).

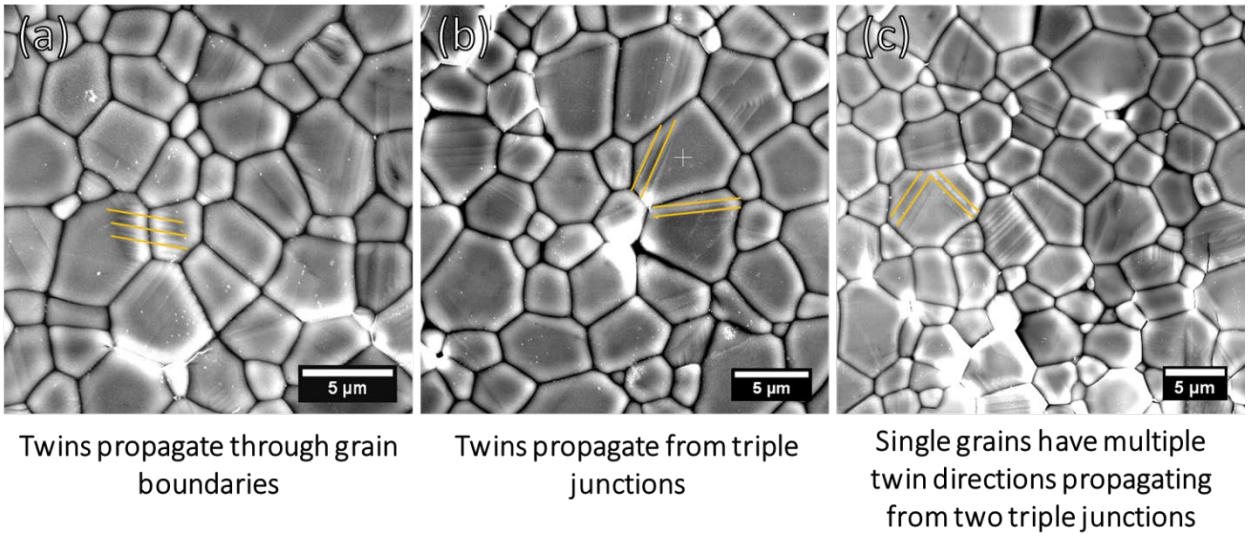

Figure 4.6: SEM images showing different conformations of twins observed. (a) lines highlight where twins appear to propagate through a grain boundary. (b) lines highlight twins that appear to propagate from triple junctions. (c) lines highlight multiple twin directions in a single grain, both of which appear to propagate from triple junctions.

Several grains from a twinned region were imaged in the TEM. Shown in Figure 4.7 is an example of a grain that contains a single large twin lamella. The twin lamella extends entirely through the grain with a uniform thickness. Diffraction from within the twin shows superlattice reflections consistent with previous observations of incommensurate modulation in large scale twinning. The twin intersects a grain boundary subsurface and appears to cause some local dislocation plasticity, microcracking, as well as possibly beginning to nucleate an additional twin in the neighboring grain. Overall dislocation content appears to be low.

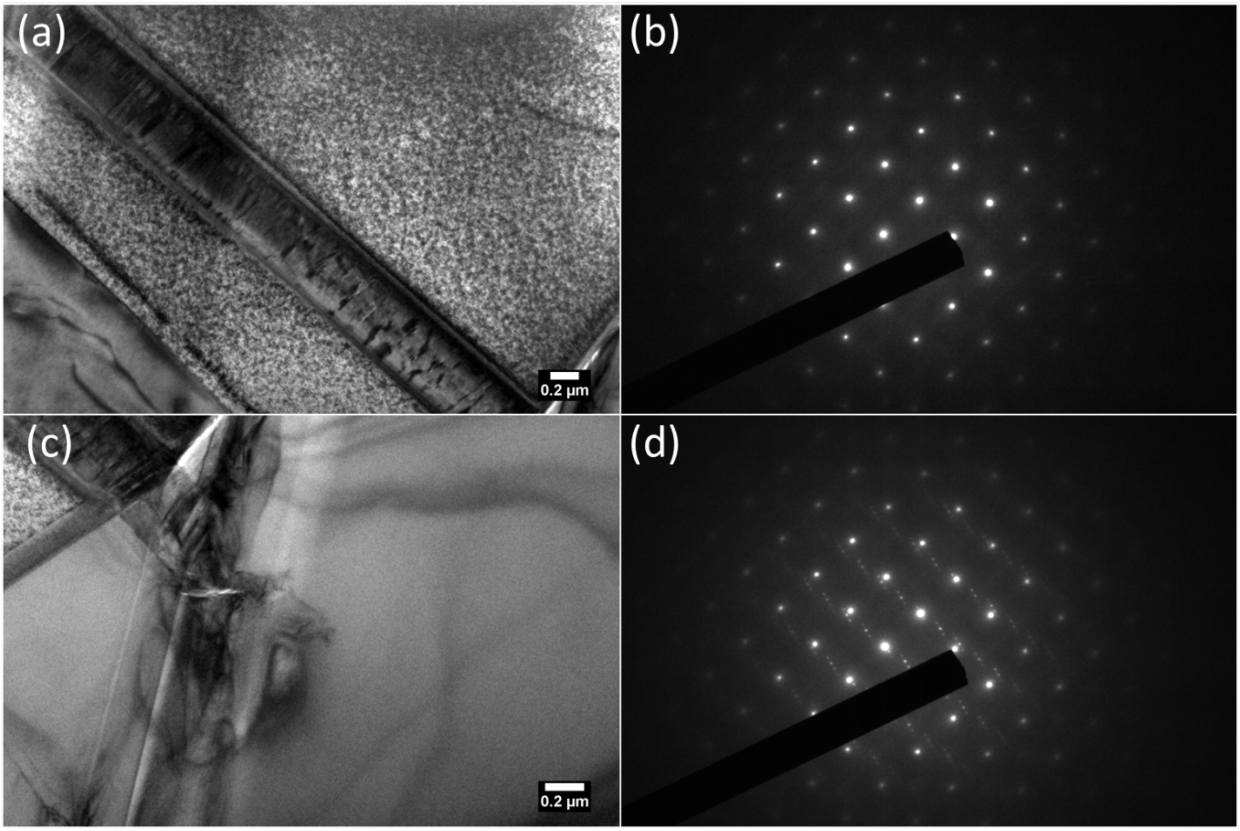

Figure 4.7: TEM images and diffraction of twinned grains. (a) Overview of a twinned grain showing the lamellar structure of the twin. Several dislocations are also visible. (c) Image of where the twin intersects the neighboring grain. Dislocation activity, microcracking and possibly nucleation of additional twins is seen. Diffraction patterns in a [100] zone axis from outside (b) and inside (d) the twin are shown. Superlattice reflections from the twin are visible in (d).

4.3.3 In Situ TEM

Finally, the stresses associated with initial deformation of three nanopillars have been collected. Each of the nanopillars had approximately (112) plane normal orientation along the loading axis so that difference in orientation was not a variable. The normal stress associated with the initial deformation event for each pillar is summarized in Table 4.3 along with the resolved shear stress on the favorable (101) twinning plane. Stress-displacement curves for the pillars are shown in Figure 4.8, where deformation events were seen as evidenced by drops in the measured stress during loading. A bright field image of pillar 3 in Figure 4.8 collected during deformation shows shearing of the pillar along a 33° angle to the indenter. A diffraction pattern of the [111] zone axis collected after deformation is shown in Figure 4.8(b).

Table 4.3: Summary of normal and resolved shear stresses onto the (101) twinning plane for three (112) oriented nanopillars.

Pillar	Normal Stress (GPa)	Resolved Shear (GPa)
1	2.38	1.47
2	3.07	1.89
3	6.16	3.80

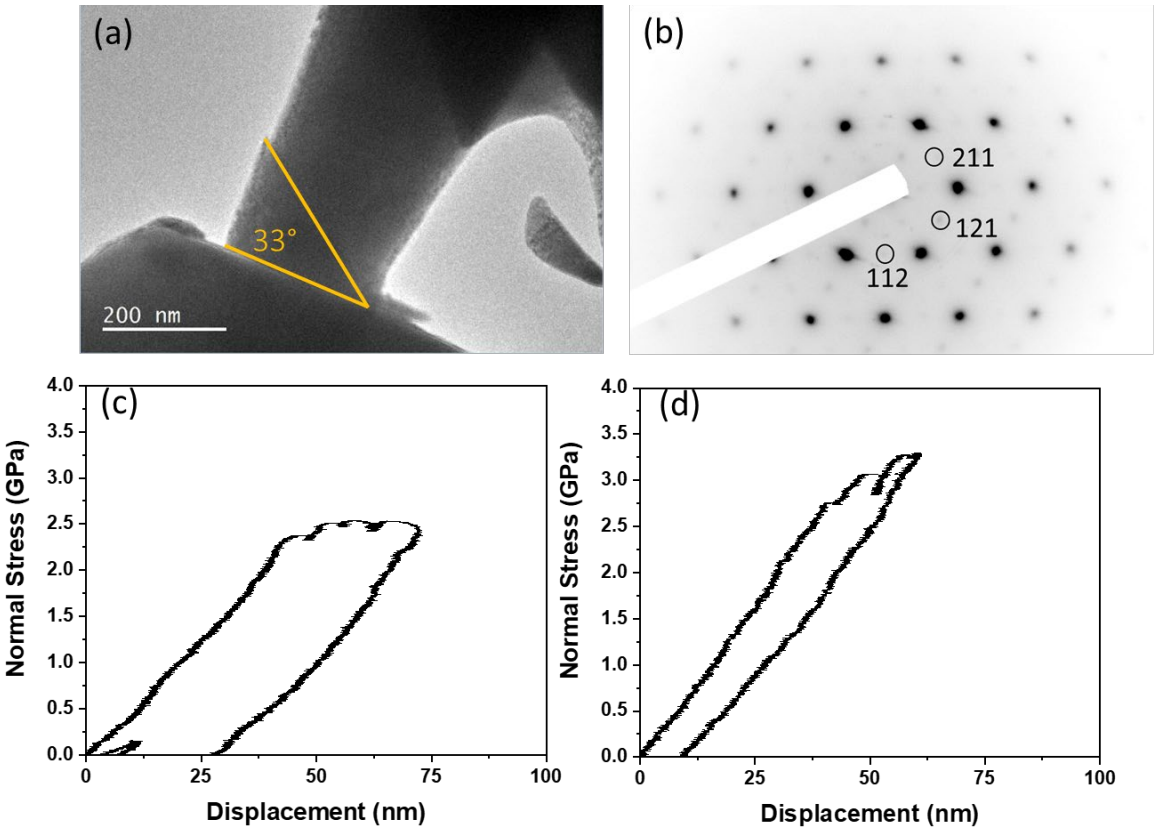

Figure 4.8: (a) image of a pillar during deformation shows shearing along a 33° angle to the indenter tip. (b) diffraction pattern of a pillar in a [111] zone axis shows slight intensity from all {112} reflections indicating the presence of multiple domains. The contrast has been inverted for ease of viewing. (c,d) Stress-displacement curves from nanopillar deformation. Pillar 1 shows multiple load drops indicative of multiple deformation events while pillar 2 shows a single load drop before unloading. They exhibit deformation at different stress despite having similar orientations.

4.4 Discussion

To begin discussing these results it is first important to acknowledge some of the assumptions and limitations involved in the methodologies described above. First it is important to discuss Vickers indentation as a method of deformation. Vickers indentation is often used to measure hardness, elastic modulus, yield strength, and fracture toughness for a material [21–23]. For ceramic materials, hardness and toughness are often measured by this microindentation technique. Although quantification of toughness using indentation is still somewhat controversial, toughness measurements using Vickers indentation are common [24–26]. To measure toughness, Vickers indents must have Palmqvist cracks radiating from the tips of the indent corners [21]. The indents used in this study are not suitable for these measurements since they often do not have the necessary radial cracking and also exhibit microcracking. However, hardness or toughness measurements are not the aim of this study, but rather the aim is to apply a stress state that is suitable for inducing twinning in a large enough area of a polycrystal to collect statistics on the grain sizes favored for twin nucleation. Vickers indentation serves this purpose.

Another interesting feature of the indents is the pileup behavior. Pileup is another factor that makes measurement of properties such as hardness and elastic modulus difficult [27,28]. Pileup is typically reported for materials that deform plastically and that do not work harden significantly [28,29]. However, pileup has also been reported in ferroelastic ceramics and has been attributed primarily to ferroelastic deformation rather than other types of deformation [30]. Here, significant pileup is observed along the flat edges of the indents and is also attributed to ferroelastic deformation in these edge regions. However, the pileup height does not directly correlate to the density of twins observed at the surface of indents for either the edge or corner regions, as shown in in plots in Figure 4.5 and correlation statistics listed in Table 4.2. This lack of correlation is perhaps due to additional ferroelastic deformation subsurface, that was not accounted for in the twin density measurements at the surface. To understand why pileup and ferroelastic deformation is observed in these locations, the stress state surrounding a Vickers indent must be discussed.

Vickers indentation results in elastic deformation, plastic deformation, as well as ferroelastic deformation, and fracture in this case, making analytical determination of the stresses associated with the deformation impossible. This complex stress state makes it difficult to correlate the observed deformation to a value of stress. Typically, Vickers indentation produces high tensile

stresses at the indent corners, which contributes to the cracking that is typically observed, while producing higher compressive and shear stresses along the indent edges and beneath the indent [31]. Hertzian indentation does not have this limitation, as the stresses resulting from Hertzian contacts before fracture are known. In this study it is observed that no twin nucleation at the surface results from Hertzian contacts, even when fracture occurs. It is concluded that this is a result of Herzian contact producing high shear stresses subsurface, rather than at the surface, and having only high compressive stress at the contact interface. Vickers indentation on the other hand causes twin nucleation at the surface, which seems to result from the higher localized shear stresses resulting from the pyramidal contact. Although the twin density did not correlate to pileup height, the regions along the indent edges did exhibit more than double the number of twins per unit area than the indent corners. This provides further evidence that twins preferentially nucleate in regions with high shear stress (edges) rather than regions with higher tensile stresses (corners). Similar observations of shear deformation localized along indent edges have been made previously in materials such as bulk metallic glasses that deform through shear banding [32]. Furthermore, many twins were observed in the absence of significant cracking. This suggests that high shear stress, even without fracture may result in significant ferroelastic deformation. Under the complex stress state that is responsible for nucleating twins, the effect that microstructure has on the probability of nucleating twins will now be discussed.

A large number of grains surrounding indents were analyzed to ensure that significant statistics could be gathered regarding grain sizes favorable for twin nucleation. As can be seen in Figure 4.2 and Table 4.1, samples with two different overall grain size distributions exhibited similar trends. For both samples, twinned grains were larger than the overall average grain size and nearest neighbors to twinned grains are smaller than the average grain size. The difference in size between grains that twinned and their nearest neighbors shows that for grains in close proximity, that should be experiencing similar levels of stress (assuming an isotropic homogenous body, which it is not), larger grains twin more easily. This makes sense when considering the energy dissipation involved in twinning. As grain size increases, the elastic energy stored within a larger crystal may be dissipated more efficiently by formation of twin boundaries than for smaller grain sizes since the volume of the grain (and thus the stored elastic energy) increases faster than the increase in energy due to the addition of planar twin boundaries [33]. This is illustrated schematically in Figure 4.9. The data shown here also suggests that microstructures composed of

large ferroelastic grains embedded in a fine grain matrix are favorable for ferroelastic deformation. Evidence of this has been seen before in toughening curves for ferroelastic materials with bimodal grain size distributions before [6].

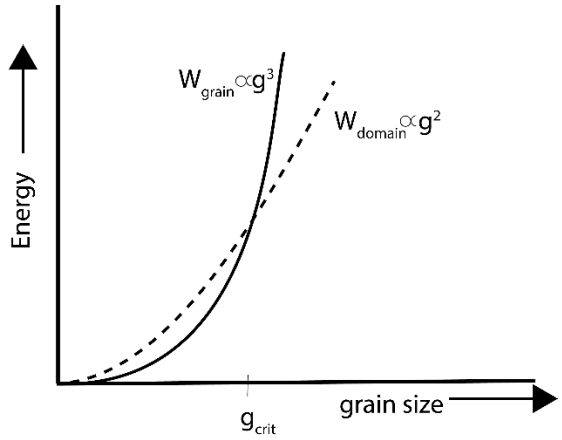

Figure 4.9: Schematic showing the increase in energy associated with elastic energy stored in the grain volume vs increase in energy from introduction of planar domain boundaries.

The grain size alone does not dictate whether twins will nucleate or not. Some insight into other features that influence nucleation may be gained by observing the conformation of twins that are nucleating within the various grains. Figure 4.6(a) shows that there are sometimes twins that appear to propagate through grain boundaries. This could be evidence that an orientation relationship exists between those grains, or that the deformations from twins can act to nucleate additional twins in neighboring grains. The relationship between crystal orientation and domain nucleation stress has been previously examined, and it was shown that the stress required for domain nucleation within single crystals does not correlate to orientation [34]. This does not, however, preclude relative orientations within a polycrystal from influencing the deformation behavior.

Twins are also often observed propagating from triple junctions or from contact areas with relatively smaller grains in the microstructure. This is likely the result of elastic anisotropy leading to the local heterogeneity in how stress is transferred between neighboring grains. Where two grains with different elastic properties meet, shear stress can be localized, promoting the nucleation of twins at the high shear stress interface. A consequence of this is that local stress intensity may be high enough to nucleate twins without a high globally applied stress, whereas in single crystals

under uniaxial compression, the applied stress must reach a high enough global value to cause domain nucleation.

Twins often propagate through entire grains, forming lamellae with parallel twin boundaries. This type of twin is observed in the TEM section of a deformed grain in Figure 4.7. However, twins also sometimes arrest mid grain, as is observed in Figure 4.6(a). This arresting behavior was observed in deformation of single crystals of this material previously [34]. This may be a consequence of a lower stress being applied to those grains, not supplying enough energy to propagate and grow the twin across the entirety of the grain, or it may be a consequence of the twins interacting with defects such as dislocations or other twins propagating in different directions, which may interact resulting in the twins arresting. Twinning in multiple directions is also observed in many of the grains, which may be a result of multiple sites of shear stress localization surrounding a single grain causing multiple twin orientation to nucleate. These observations demonstrate that the constraints imposed by the polycrystalline microstructure are important factors dictating the nucleation of twins.

Since the stress associated with domain nucleation in the polycrystals cannot easily be determined, single crystal nanopillars were deformed using in situ TEM. Uniaxial compression of pillars provides a stress state that can easily measure the stress required for domain nucleation. However, the stresses observed to deform the nanopillars are significantly higher than the coercive stress values reported previously for similar tetragonal zirconia materials, which range from 300-700 MPa [5,35,36]. Nanopillars exhibited deformation stresses of 2.38, 3.07, and 6.16 GPa respectively with translate to 1.47, 1.89, 3.80 GPa in resolved shear stress on the (101) twin plane. Nanopillars exhibited nucleation of multiple domains, similar to what is observed for many grains in the polycrystals, as evidenced by the diffraction pattern shown in Figure 4.8(b). However, the intensity from the (112) spots indicating the presence of multiple domains is very low. This suggests that multiple domains do nucleate, but in very low volumes. It is possible that dislocation plasticity as well as domain nucleation is active, as was seen in previous evaluations of larger scale CTZ single crystals [34]. Deformation in one of the nanopillars was observed to act by shearing along a 33° angle to the indenter tip. This is very close to the 35° angle expected for deformation along the (101) twinning plane. However, the morphology of the shear may indicated that dislocation plasticity was also present. The large values of stress observed here likely are

influenced by size effects. The data on polycrystalline samples here clearly shows that smaller grains are less likely to twin, since the energy penalty for creating twin boundaries is relatively high compared to dissipation of elastic energy through other means such as plasticity or fracture.

However, very high deformation stresses, as well as highly stochastic deformation stresses were also previously observed in micropillar deformation of this material, for which the deformed volume of material was orders of magnitude higher than the nanopillars tested here [34]. It is likely that the stress state as well as the difference in constraints surrounding the crystals is important here. For pillars deformed by uniaxial compression, shear stress responsible for twinning must be resolved onto the twin plane. The stress state is not one of simple shear. Whereas in a polycrystal, difference in elastic modulus between neighboring grains can lead to local shearing of crystals that creates a much more favorable condition for twin nucleation. Furthermore, once twins have nucleated, they may impinge on neighboring grains to assist in the nucleation of additional twins as is observed in Figure 4.7(c). The TEM observations also show that much lower dislocation density is observed in samples taken from the bulk polycrystal compared to the dislocation density observed in nano and micropillars that were deformed. This is further evidence that the size and constraint of the crystal greatly affects how energy is most effectively dissipated in these crystals, and how the favored deformation mechanisms can be controlled by changing the microstructure.

Unfortunately, since the stress state surrounding the Vickers indents here is not known, it is impossible to compare the stresses associated with twin nucleation in the polycrystal to those observed in the single crystal pillars. Therefore, a valuable next step in studying the effect of microstructure on domain nucleation is to use techniques to deform the polycrystal where the stress state can be determined for a specific location where twinning occurs. One possible route to achieve this is to perform Hertzian indentation again, but to image cross sections of the indents such that the microstructure below the surface where high shear stress occurs may be observed. This will have the added benefit of not restricting observations to grains that twinned at the surface, where grains are not fully constrained as they are in real ceramic microstructures.

4.5 Conclusion

Polycrystalline ferroelastic CTZ was deformed using microindentation such that twins were nucleated within many grains. Vickers indentation produced high local shear stresses at the sample surface which resulted in prolific twin nucleation, while Hertzian indention does not

produce high shear stress at the surface, and therefore does not readily nucleate observable twins. Large numbers of grains were analyzed showing that twins more frequently nucleate in relatively large grains that are nearest neighbors with smaller undeformed grains. This suggests that microstructures containing large grains embedded in a fine-grained matrix favor increased ferroelastic deformation. Furthermore, twins were frequently observed to nucleate emanating from triple junctions in the microstructure. This further corroborates that high local shear stress that results from microstructural heterogeneity is important for promoting twin nucleation.

Deformation stresses in single crystal CTZ nanopillars were measured using *in situ* TEM and were found to be much higher than coercive stress values previously reported in similar tetragonal zirconia materials. These observations combined with the results observed in polycrystals suggest that size scale as well as the stress state resulting from microstructural constraints plays an important role in ferroelastic deformation.

4.6 References

[1] A. V Virkar, R.L.K. Matsumoto, Ferroelastic Domain Switching as a Toughening Mechanism in Tetragonal Zirconia, J. Am. Ceram. Soc. 69 (1986) C-224-C-226. https://doi.org/10.1111/j.1151-2916.1986.tb07341.x.

[2] A.G. Evans, D.R. Clarke, C.G. Levi, The influence of oxides on the performance of advanced gas turbines, J. Eur. Ceram. Soc. 28 (2008) 1405–1419. https://doi.org/https://doi.org/10.1016/j.jeurceramsoc.2007.12.023.

[3] A. Kolleck, G.A. Schneider, F.A. Meschke, R-Curve Behavior of BaTiO3 - and PZT Ceramics Under the Influence of an Electric Filed Applied Parallel to the Crack Front, Acta Mater. 48 (2000) 4099–4113. https://doi.org/10.1016/S1359-6454(00)00198-1.

[4] N. Orlovskaya, M. Lugovy, S. Pathak, D. Steinmetz, J. Lloyd, L. Fegely, M. Radovic, E.A. Payzant, E. Lara-Curzio, L.F. Allard, J. Kuebler, Thermal and mechanical properties of LaCoO3 and La0.8Ca0.2CoO3 perovskites, J. Power Sources. 182 (2008) 230–239. https://doi.org/10.1016/j.jpowsour.2008.03.072.

[5] C. Mercer, J.R.R. Williams, D.R.R. Clarke, a. G.G. Evans, On a ferroelastic mechanism governing the toughness of metastable tetragonal-prime (t′) yttria-stabilized zirconia, Proc.

R. Soc. A Math. Phys. Eng. Sci. 463 (2007) 1393–1408. https://doi.org/10.1098/rspa.2007.1829.

[6] F. Meschke, A. Kolleck, G.A. Schneider, R-curve behaviour of BaTiO3 due to stress-induced ferroelastic domain switching, J. Eur. Ceram. Soc. 17 (1997) 1143–1149. https://doi.org/10.1016/s0955-2219(96)00211-7.

[7] K. Mehta, A. V. Virkar, Fracture Mechanisms in Ferroelectric-Ferroelastic Lead Zirconate Titanate (Zr: Ti=0.54:0.46) Ceramics, J. Am. Ceram. Soc. 73 (1990) 567–574. https://doi.org/10.1111/j.1151-2916.1990.tb06554.x.

[8] J.A. Krogstad, M. Lepple, C.G. Levi, Opportunities for improved TBC durability in the CeO2-TiO2-ZrO2 system, Surf. Coatings Technol. 221 (2013) 44–52. https://doi.org/10.1016/j.surfcoat.2013.01.026.

[9] D. Baither, B. Baufeld, U. Messerschmidt, A.H. Foitzik, M. Rühle, Ferroelasticity of t‘-Zirconia: I, High-Voltage Electron Microscopy Studies of the Microstructure in Polydomain Tetragonal Zirconia, J. Am. Ceram. Soc. 80 (1997) 1691–1698. https://doi.org/10.1111/j.1151-2916.1997.tb03040.x.

[10] B. Baufeld, D. Baither, U. Messerschmidt, M. Bartsch, A.H. Foitzik, M. Rühle, Ferroelasticity of t‘-Zirconia: II, In situ Straining in a High-Voltage Electron Microscope, J. Am. Ceram. Soc. 80 (1997) 1699–1705. https://doi.org/10.1111/j.1151-2916.1997.tb03041.x.

[11] J. Sheng, C.M. Landis, Toughening due to domain switching in single crystal ferroelectric materials, Int. J. Fract. 143 (2007) 161–175. https://doi.org/10.1007/s10704-007-9056-7.

[12] K. Kim, J.E. Huber, In situ observation of ferroelastic domain evolution in a near-morphotropic Pb(Zr,Ti)O3ceramic by piezoresponse force microscopy, J. Eur. Ceram. Soc. 35 (2015) 1459–1468. https://doi.org/10.1016/j.jeurceramsoc.2014.11.027.

[13] J.L. Jones, E.B. Slamovich, K.J. Bowman, Domain texture distributions in tetragonal lead zirconate titanate by x-ray and neutron diffraction, J. Appl. Phys. 97 (2005). https://doi.org/10.1063/1.1849821.

[14] J.L. Jones, M. Hoffman, R-curve and stress-strain behavior of ferroelastic ceramics, J.

Am. Ceram. Soc. 89 (2006) 3721–3727. https://doi.org/10.1111/j.1551-2916.2006.01300.x.

[15] W.S. Kreher, Influence of domain switching zones on the fracture toughness of ferroelectrics, J. Mech. Phys. Solids. 50 (2002) 1029–1050. https://doi.org/https://doi.org/10.1016/S0022-5096(01)00110-7.

[16] K.M. Prettyman, J.F. Jue, A. V Virkar, C.R. Hubbard, O.B. Cavin, M.K. Ferber, Hysteresity effects in 3 mol% yttria-doped zirconia (t'-phase), J. Mater. Sci. 27 (1992) 4167–4174. https://doi.org/10.1007/BF01105121.

[17] M. V Swain, R.H.J. Hannink, R-curve behavior in zirconia ceramics, American Ceramic Society, Inc, United States, 1983. http://inis.iaea.org/search/search.aspx?orig_q=RN:17050039.

[18] G. Rauchs, T. Fett, D. Munz, R-curve behaviour of 9Ce-TZP zirconia ceramics, Eng. Fract. Mech. 69 (2002) 389–401. https://doi.org/https://doi.org/10.1016/S0013-7944(01)00073-X.

[19] J.S. Yang, X.M. Chen, T. Aizawa, M. Kuwabara, PZT based piezoelectric ceramics with enhanced fracture toughness, Solid State Ionics. 108 (1998) 117–121. https://doi.org/https://doi.org/10.1016/S0167-2738(98)00028-9.

[20] M.J. Mayo, Synthesis and applications of nanocrystalline ceramics, Mater. Des. 14 (1993) 323–329.

[21] A.G. Evans, E.A. Charles, Fracture Toughness Determinations by Indentation, J. Am. Ceram. Soc. 59 (1976) 371–372. https://doi.org/10.1111/j.1151-2916.1976.tb10991.x.

[22] Y.-T. Cheng, C.-M. Cheng, What is indentation hardness?, Surf. Coatings Technol. 133–134 (2000) 417–424. https://doi.org/https://doi.org/10.1016/S0257-8972(00)00896-3.

[23] A.E. Giannakopoulos, P.-L. Larsson, R. Vestergaard, Analysis of Vickers indentation, Int. J. Solids Struct. 31 (1994) 2679–2708. https://doi.org/https://doi.org/10.1016/0020-7683(94)90225-9.

[24] G.D. Quinn, R.C. Bradt, On the Vickers Indentation Fracture Toughness Test, J. Am.

Ceram. Soc. 90 (2007) 673–680. https://doi.org/10.1111/j.1551-2916.2006.01482.x.

[25] R. Morrell, Fracture toughness testing for advanced technical ceramics: internationally agreed good practice, Adv. Appl. Ceram. 105 (2006) 88–98. https://doi.org/10.1179/174367606X84422.

[26] C.B. Ponton, R.D. Rawlings, Vickers indentation fracture toughness test Part 1 Review of literature and formulation of standardised indentation toughness equations, Mater. Sci. Technol. 5 (1989) 865–872. https://doi.org/10.1179/mst.1989.5.9.865.

[27] S.K. Kang, J.Y. Kim, C.P. Park, H.U. Kim, D. Kwon, Conventional Vickers and true instrumented indentation hardness determined by instrumented indentation tests, J. Mater. Res. 25 (2010) 337–343. https://doi.org/10.1557/jmr.2010.0045.

[28] A. Bolshakov, G.M. Pharr, Influences of pileup on the measurement of mechanical properties by load and depth sensing indentation techniques, J. Mater. Res. 13 (1998) 1049–1058. https://doi.org/10.1557/JMR.1998.0146.

[29] K. Matsuda, Prediction of stress-strain curves of elastic-plastic materials based on the Vickers indentation, Philos. Mag. A. 82 (2002) 1941–1951. https://doi.org/10.1080/01418610208235706.

[30] F.R. Chien, F.J. Ubic, V. Prakash, A.H. Heuer, Stress-induced martensitic transformation and ferroelastic deformation adjacent microhardness indents in tetragonal zirconia single crystals, Acta Mater. 46 (1998) 2151–2171. https://doi.org/10.1016/S1359-6454(97)00444-8.

[31] K.E. Johanns, J.H. Lee, Y.F. Gao, G.M. Pharr, An evaluation of the advantages and limitations in simulating indentation cracking with cohesive zone finite elements, Model. Simul. Mater. Sci. Eng. 22 (2013) 15011. https://doi.org/10.1088/0965-0393/22/1/015011.

[32] S. Jana, U. Ramamurty, K. Chattopadhyay, Y. Kawamura, Subsurface deformation during Vickers indentation of bulk metallic glasses, Mater. Sci. Eng. A. 375–377 (2004) 1191–1195. https://doi.org/https://doi.org/10.1016/j.msea.2003.10.068.

[33] G. Arlt, Twinning in ferroelectric and ferroelastic ceramics: stress relief, J. Mater. Sci. 25 (1990) 2655–2666. https://doi.org/10.1007/BF00584864.

[34] C. Smith, Q. Rizzardi, R. Maass, J. Krogstad, Evaluating a Critical Resolved Shear Stress Criterion for Domain Nucelation in Ferroelastic Ceramics, Manuscript in preparation (2020).

[35] D. Baither, M. Bartsch, B. Baufeld, A. Tikhonovsky, A. Foitzik, M. Rühle, U. Messerschmidt, Ferroelastic and Plastic Deformation of t′-Zirconia Single Crystals, J. Am. Ceram. Soc. 84 (2001) 1755–1762. https://doi.org/10.1111/j.1151-2916.2001.tb00911.x.

[36] U. Messerschmidt, D. Baither, B. Baufeld, M. Bartsch, Plastic deformation of zirconia single crystals: A review, Mater. Sci. Eng. A. 233 (1997) 61–74. https://doi.org/10.1016/s0921-5093(97)00050-6.

CHAPTER 5

VARIATION IN DENSIFICATION BEHAVIOR OF IONIC CONDUCTING YSZ PROCESSED VIA SPARK PLASMA SINTERING

So far in this dissertation, the relationship between microstructural features and ferroelastic deformation has been discussed, and an improved understanding linking microscale and macroscale deformation behavior has been developed. As mentioned in section 1.6, there was also a secondary objective associated with this dissertation focused on developing an improved understanding of the mechanisms associated with advanced ceramic processing done by spark plasma sintering (SPS). This chapter will discuss the research done to test the hypothesis that electric current plays a role in the densification behavior of ionic conducting ceramics processed by spark plasma sintering. The goal of reporting on variability in processing materials using the SPS technique will also be discussed. This secondary objective is distinct from the sections discussing ferroelastic deformation, however, understanding ceramic processing is still crucial to being able to design microstructures, and therefore is complementary to the overall goal of developing improved microstructural designs for intrinsically toughened ceramics.

5.1 Introduction

Although the use of large electric currents for the purpose of sintering is not a recent development, the commercialization of spark plasma sintering (SPS) or field assisted sintering techniques (FAST), in the past few decades has generated significant interest in the field. This rise in popularity is, in large part, due to spark plasma sintering's ability to both synthesize and process a wide range of materials including ceramics, metals, and composites to form exceptionally dense bulk nanostructured materials [1–3]. Spark plasma sintering is particularly remarkable in its ability to complete this processing using reduced temperatures and sintering times when compared to other sintering and consolidation techniques, such as hot pressing and conventional pressureless sintering [1].

Despite the rapid increase in popularity of spark plasma sintering, there is still considerable debate surrounding the precise mechanisms driving densification. SPS relies on a combination of mechanical, thermal, and electrical driving forces, which may all influence the sintering behavior for various materials differently [4]. The role that the electric current plays in sintering has been

the subject of particular interest and debate. For electrically conductive samples, current has been proposed to influence sintering through mechanisms including current percolation and Joule heating [5], Peltier heating [6], and electromigration [1]. However, for electrically insulating samples the role of the current is even less clear, with some results suggesting that direct application of current does not affect densification mechanisms [7], while others suggest that electric fields and currents associated with SPS do improve sinterability for ceramics [8–10].

In the absence of a mechanistic understanding of sintering under SPS conditions, an empirical approach is commonly employed to identify the appropriate SPS parameters specific to different materials. This is further complicated by the fact that it is difficult to directly measure and predict many key experimental parameters in the sample during SPS processing, such as powder temperature [11], heating rate [12], pressure gradients [4], and local current density. Because of the experimental challenges and mechanistic uncertainty, groups often report using wide ranges of experimental parameters to process similar materials, making comparisons of results difficult or impossible. For example processing temperatures ranging from 1275-1600°C have been reported to achieve full density for alumina when sintered using 50 MPa of applied pressure in the SPS [10]. Similarly, for tungsten carbide, temperatures ranging from 1425-1800°C while applied pressures of 50-126 MPa have been used to achieve densities >98% [13,14]. The wide range of parameters mentioned here serves to showcase that selection of appropriate parameters even for well-studied materials is often non-trivial, and the outcomes may still deviate significantly from those reported in literature.

Here we will focus on the processing of yttria stabilized zirconia (YSZ), which has maintained consistent interest for SPS processing because of its ubiquity as a high toughness structural ceramic, and as an electrical ceramic often used in solid state electrolytes. YSZ's function as an electrical ceramic is of particular interest here. The substitution of Y^{3+} ions for Zr^{4+} in YSZ creates oxygen vacancies, which leads to enhanced oxygen ion conductivity. Furthermore, YSZ may transition from an electrical insulator to either an ionic or electronic conductor at high temperature and low oxygen partial pressure [15]. This presents unique challenges in predicting its SPS processing behavior. YSZ is known to electrochemically reduce when sintered at elevated temperatures under the reducing conditions created during SPS processing [3,7,16]. Therefore, post-sintering re-oxidation steps are often required, further limiting control of the microstructure using this technique [16]. YSZ has been shown to develop drastically different electrical and

mechanical properties when sintered using different SPS parameters [16]. Because of this, selecting appropriate sintering conditions for YSZ and other ionic conductors becomes increasingly important to realize targeted properties for given applications.

Because YSZ has been extensively studied within the spark plasma sintering community, a vast range of processing conditions for sintering YSZ have been reported in the current literature. Sintering temperatures of 800-1500°C have been commonly reported [17–19], while pressures ranging from 15 MPa to several hundreds of MPa have been used [17,20]. It is clear that different combinations of processing conditions can have a significant impact on the properties of the YSZ. For instance, if high density and nanocrystalline grain size are desired, high pressures with lower temperatures (1050-1200°C) relative to conventional sintering temperatures are preferred [20]. However, if high ionic conductivity is the desired property, using multiple SPS sintering cycles at even lower temperatures (1000°C) are preferred [18].

What has not been thoroughly discussed in the current literature, however, is the variability or experimental reproducibility between and even within samples prepared under the same sintering conditions. Transitioning SPS beyond laboratory scale testing and niche applications, will require highly reliable and reproduceable results. For materials such as YSZ, where physical and electrical properties are dynamic both during and after processing, open discussion of processing variability is of even greater importance as it may provide much needed insight on the underlying mechanisms. Thus, this study aims to systematically quantify the variability in properties between and within samples sintered under identical conditions and explore routes for reducing this variability through modified sample configuration and, therefore, current paths during sintering.

5.2 Experimental Methods

5.2.1 Materials and Equipment Used

Two sample configurations were used during sintering in this study: (i) 8 wt% Y_2O_3-ZrO_2 yttria stabilized zirconia (YSZ) samples, which contacted the carbon of the die and punches directly during sintering (referred to as ‘bare’ samples), and (ii) YSZ samples, of the same composition and source, that were capped at the top and bottom by electrically conductive nickel (Ni) disks and electrically insulating alumina powder (referred to as ‘layered’ samples).

Schematics of each configuration can be viewed in Figure 5.1. The sintering procedures are described below.

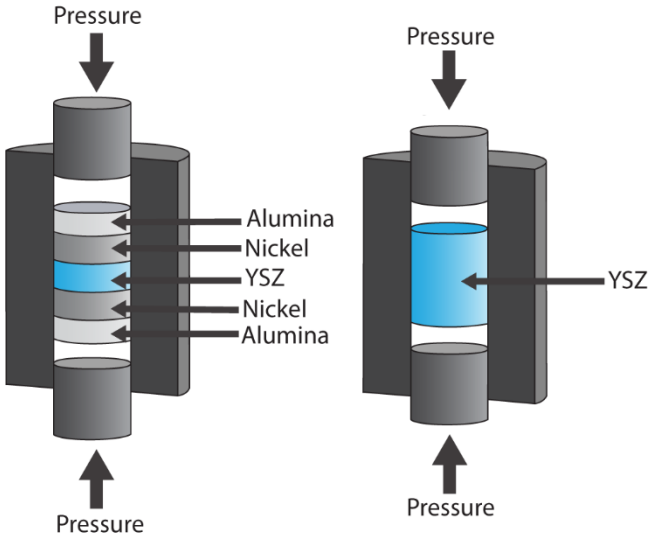

Figure 5.1: Schematics showing the position of the YSZ green body within a graphite die. The bare sample has the YSZ in contact with graphite foil and the punches of the die while the layered samples include Ni and Al_2O_3 layers on either side of the YSZ. Both bare and layered samples were designed so that the total sample heights were approximately the same prior to sintering.

All sintering in this study was performed using a Fuji SPS-615 Dr. Sinter unit (Fuji Electronic Industrial Co., Saitama, Japan). Standard strength graphite dies with an inner diameter of 20 mm were used for sintering nickel samples that were later used in the layered configuration, while 20.5 mm inner diameter dies were used for all ceramic and layered samples (dies also supplied by Fuji Electronic Industrial Co., Saitama, Japan). Samples sintered in 20.5 mm diameter dies were wrapped in a single layer of carbon foil to ensure easy release from the die. The 8 wt% Y_2O_3-ZrO_2 powders used were submicron in size and had a trace metals purity of 99.9% (Sigma Aldrich, St. Louis, MO, USA). Submicron Ni powders (Sigma Aldrich, St. Louis, MO, USA) were used to fabricate 1 mm thick disks with a 20 mm diameter, to ensure that they fit into the 20.5mm dies. These Ni disks were used as the conductive caps for the layered sample configuration. 1 µm alumina powder (Baikowski International Corporation, Charlotte, NC, USA) was used to separate the Ni disks from the punches and prevent undesirable reactions at the punch/sample interface in the layered configuration. 20 mm diameter binderless green body YSZ pellets were pressed under 31 MPa pressure using a Carver press prior to loading into the graphite dies for sintering to ensure comparable particle packing prior to sintering.

5.2.2 Sintering

The Ni disks were densified via SPS under vacuum at 750°C with a two-minute hold and an applied pressure of 30 MPa in order to create dense, conductive disks of the appropriate diameter for the layered samples. Heating rates of 100°C/min up to 700°C and 50°C/min up to 750°C were used. Temperature was measured and controlled during sintering of the Ni disks using a K-type thermocouple placed into a small borehole on the outside of the graphite die. Several bare YSZ samples were initially sintered at temperatures ranging from 800°C-1200°C with an applied pressure of 33 MPa to develop baseline results for the hardness resulting from different sintering temperatures.

All other sintering for both the bare and layered YSZ samples was done under vacuum using a maximum temperature of 1100°C, with a 10 minute hold and an applied pressure of 33 MPa. Heating rates of 100°C/min from 600°C to 1100°C were used, with no temperature control below 573°C. Temperature was measured using a CHINO IR-AH digital radiation thermometer (CHINO Corporation, Tokyo, Japan) aimed at the same borehole on the outside of the die. Dies were wrapped in carbon wool to reduce heat loss during sintering.

5.2.3 Sample Characterization

The mechanical properties of the sintered samples were characterized using a Vickers hardness test. Indents were performed using a Zeiss Microhardness tester (Carl Zeiss AG, Oberkochen, Germany). Loads of 500g were used for all indents and at least 10 indents were performed on the cross section of each sintered sample. Indents were spaced at least 500μm apart to avoid any interaction between the indents. Indent dimensions were measured using an optical microscope. The Vickers hardness number HV, was calculated and converted to MPa using the formula

$$HV = 1854.4L/d^2 \qquad \text{Equation 5.1}$$

where d is the mean diagonal length for the indent and L is the load in gram force according to ASTM standard C1327-15 [21]. Microstructural characterization was performed using a JEOL 7000F scanning electron microscope and a JEOL 2100 CRYO transmission electron microscope (JEOL Ltd., Tokyo, Japan).

5.3 Results

Initially, bare YSZ samples were sintered at temperatures ranging from 800°C-1200°C and hardness measurements were done, the preliminary results of which are shown in Figure 5.2. It can be seen that there is a steep increase in the hardness of YSZ samples when temperatures around 1150°C are used. After 1150°C the hardness becomes very sensitive to the sintering temperature.

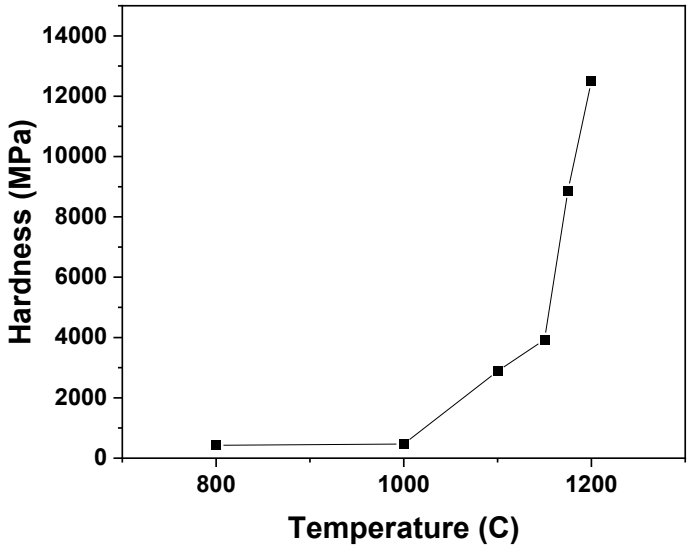

Figure 5.2: Vickers hardness measured against sintering temperature for bare YSZ samples.

During the densification of each bare and layered sample, several parameters—including the die temperature, applied current, and Z-axis displacement (distance the bottom SPS ram has moved up since starting the sintering program)—were recorded. Figure 5.3 reports Z-axis displacement, temperature, and current plots for samples prepared with both bare and layered configurations. It is important to note that temperatures below 573 °C cannot be measured using the digital radiation thermometer used in this system. Therefore, data collected before the temperature reached 573 °C, and the system began effectively reading the temperature has been excluded.

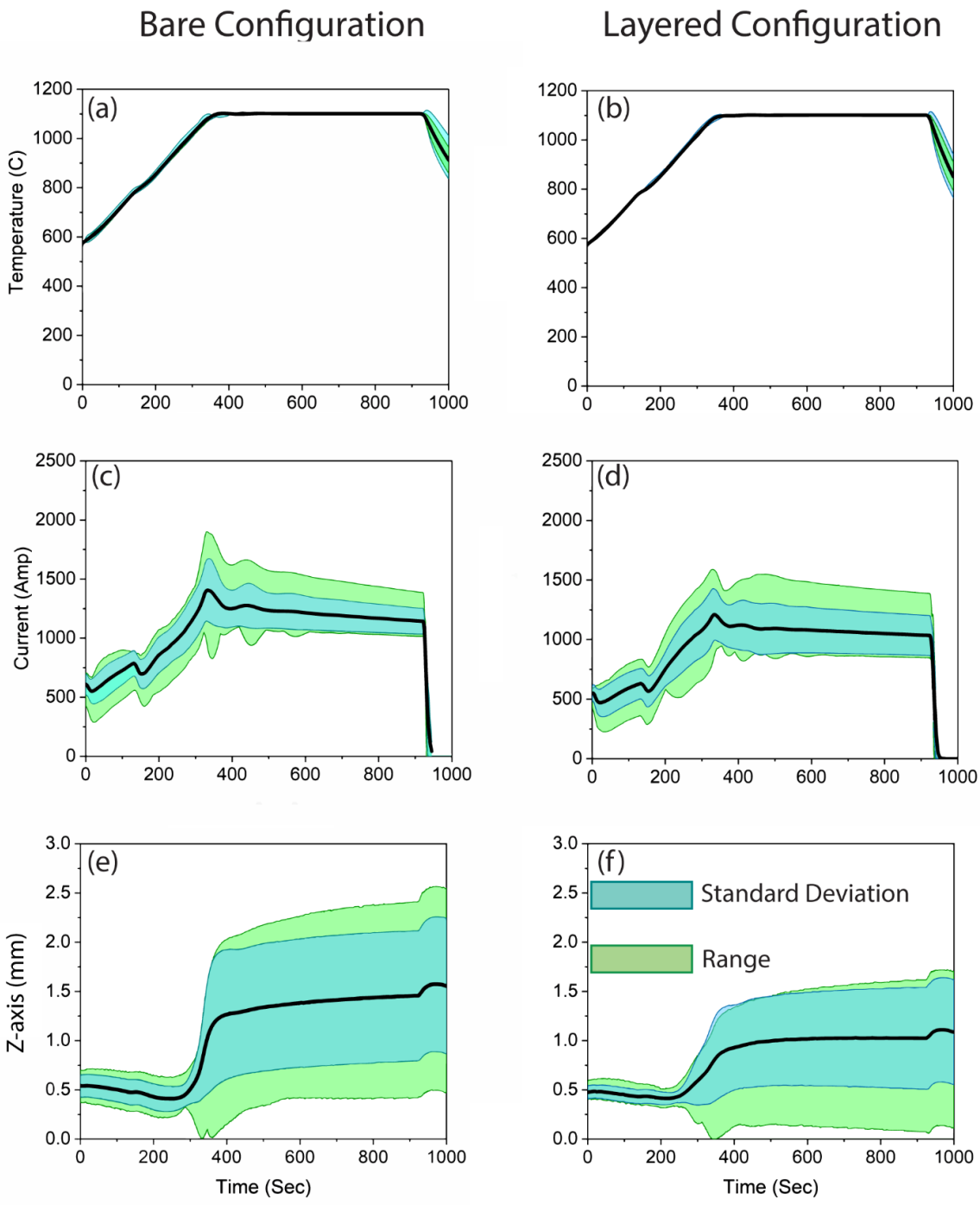

Figure 5.3: Temperature, Z-axis, and current profiles collected during sintering of bare (a, c, e) and layered (b, d, f) samples. Each plot shows the average profile collected for all ten samples in each configuration (black line) as well as the range of values at each time during sintering (shaded green) and the standard deviation of values at each time (shaded blue).

The plots in Figure 5.3 show the average current, temperature, and Z-axis displacement collected for all ten samples in each configuration with both the total range of values as well as the standard deviation of values at each time overlaid to show the variation in the SPS parameters and densification between different samples. It can be seen that for both bare and layered configurations, the temperature profiles during sintering have very narrow ranges, with only small deviations from the average occurring throughout the processing between all ten samples in each configuration. This is to be expected for a machine with properly tuned PID values operating in automatic temperature control. However, the current needed to achieve these temperatures, and the resulting Z-axis displacement due to densification had large ranges for both configurations. The average current profiles for bare and layered configurations are similar in shape and magnitude, however, the range of values at a given time was large, with some points having more than a 1000 Amp difference between samples to achieve the same temperature for the bare configuration. The Z-axis displacement profiles are similar in shape; however, the average displacement for bare samples is consistently larger in magnitude than for layered samples. Similarly, the range of displacement values for bare samples is larger than the range for the layered samples.

Following sintering, each sample was sectioned, polished and mounted in epoxy for micro-indentation. The micro-indentation serves as a localized measure of the materials hardness and can be taken as an analog to the densification that has occurred during sintering, with higher hardness corresponding to a greater degree of densification [22]. Micro-indentation has been used in this way because the density of a single layer of the layered samples cannot be accurately measured using other techniques such as the Archimedes method or gas pycnometry. It also provides an opportunity to reveal site-specific variations in density within a single layer/specimen. The Vickers hardness has been compiled for the YSZ in all ten samples for both bare and layered configurations. Hardness was also compiled for the Ni layers contained in the layered configiration samples. All hardness data collected for each configuration has been compiled and plotted on box-and-whisker plots shown in Figure 5.4(a). The box-and-whisker plots show the means, medians, interquartile range (IQR), and 1.5 times the interquartile range (represented by the whiskers) of hardness values for both bare and layered configurations. Outliers were defined as datapoints that fell outside of 1.5 times the interquartile range. These outliers were excluded from calculations of the median and mean, and are shown on the plot as well. The outliers lie above the whiskers for

the bare samples and Ni layers in Figure 5.4(a). Figure 5.4(b) presents box-and-whisker plots for each individual YSZ sample. These illustrate the distribution in hardness within each unique sample that was prepared. Sample 10 of layered configuration fractured significantly during sectioning, allowing limited room for indentation, and resulting in only a single data point for that sample. It can be seen that the range of hardness values found in the bare samples is much larger than the range observed for layered samples.

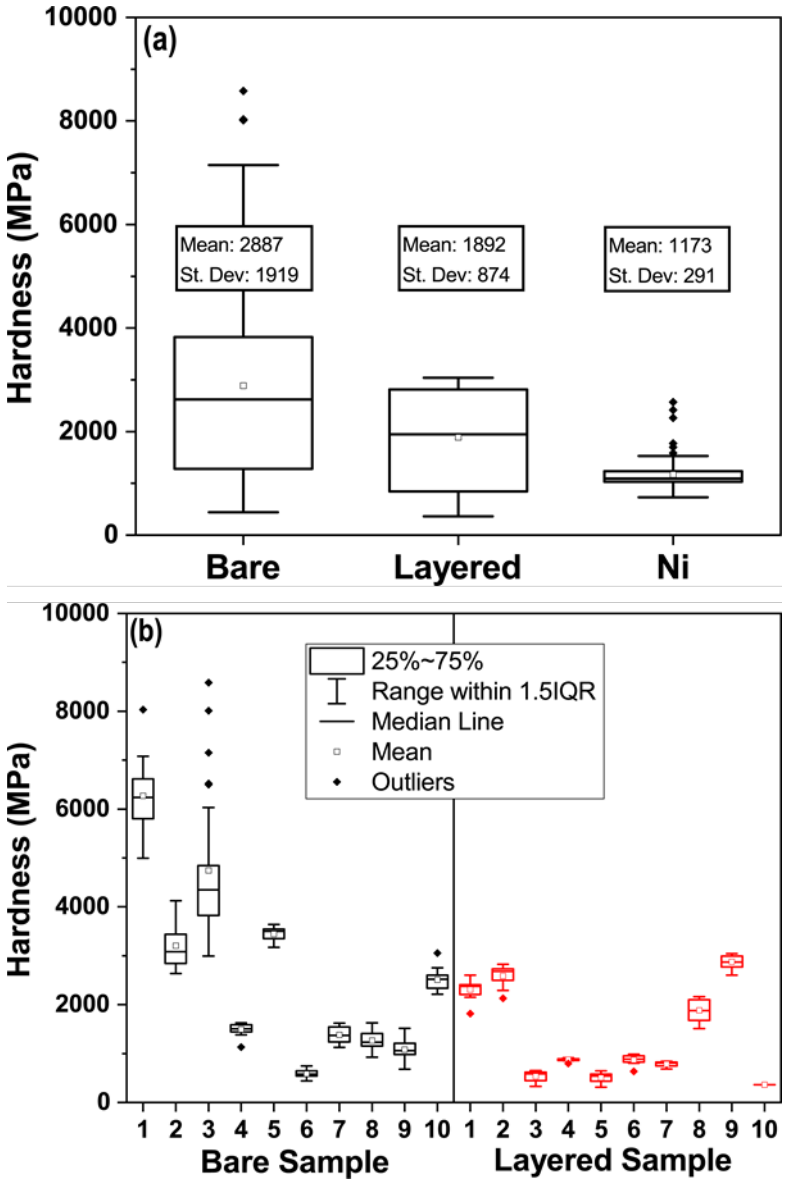

Figure 5.4: (a) Box-and-whisker plots of compiled Vickers hardness data for all YSZ samples produced in bare and layered configurations. Hardness values of the Ni layers in the layered configuration have also been compiled. (b) Box-and-whisker plots of Vickers hardness data for each individual YSZ sample. Each plot shows the mean, median, interquartile range, and outliers falling beyond 1.5 IQR for the data being considered.

The locations of indents done on sample cross-sections typically spanned nearly the full length of the cross-section. The hardness measurements from individual indents were tracked and plotted against indent number for several of the bare YSZ samples. This was done to determine if there were hardness gradients across samples. Figure 5.5 shows the hardness values measured across sample cross-sections for bare samples 1, 2, and 6, which each had different mean hardness values and different ranges in hardness. There appears to be no trend in the location of indents to hardness values measured across each of these samples.

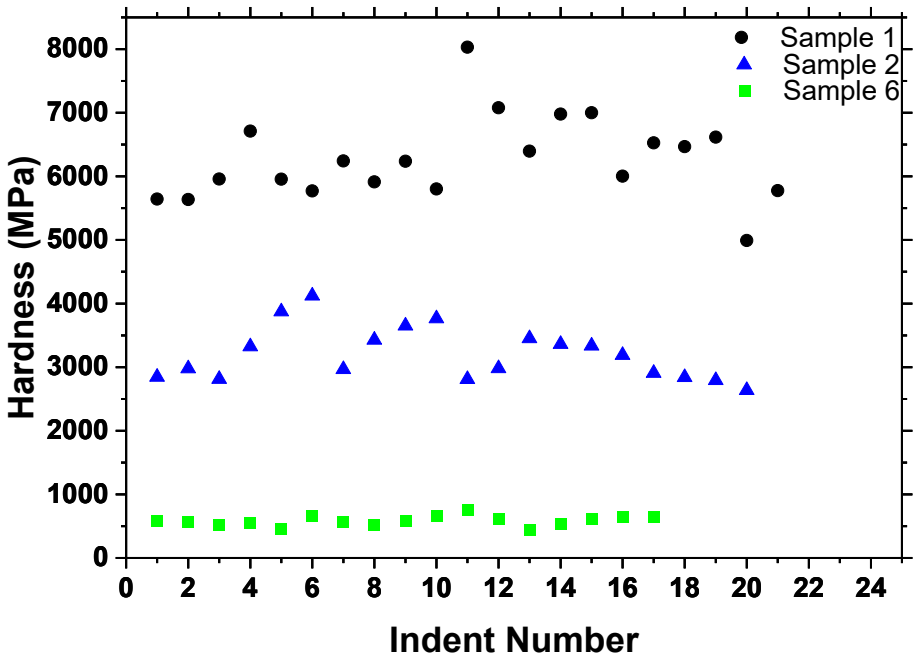

Figure 5.5: Hardness measurements from individual indents plotted against indent number for bare samples 1, 2, and 6 which exhibited different mean sample hardness.

Photographs of the cross section of each sample were taken. The images of three examples of bare sample cross sections, as well as three representative images of layered cross sections, are shown in Figure 5.6. It is important to note that the samples shown have been specifically selected for imaging because of the variation in darkening across the sections for the bare samples, while the selected layered samples are representative of the degree of darkening seen in all layered samples. The darkening of the samples is indicative of reduction and oxygen deficiency in those regions of the YSZ [23].

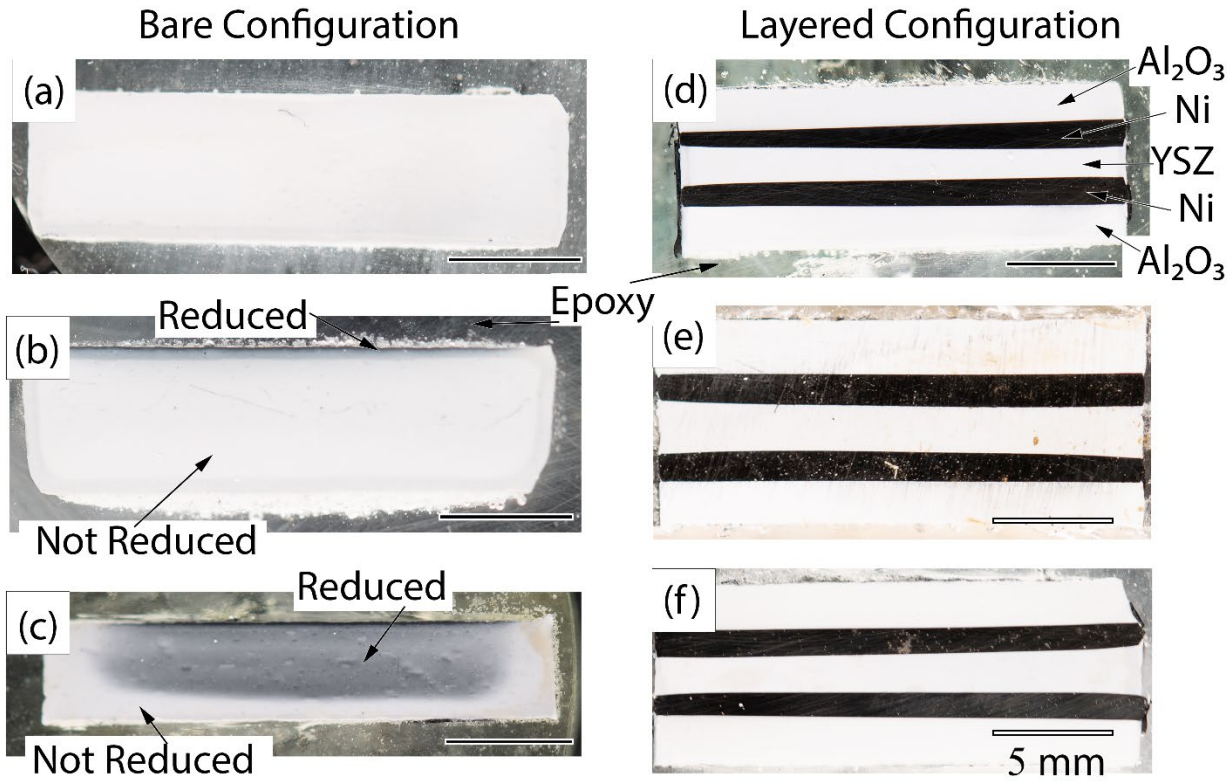

Figure 5.6 (a,b,c) Bare samples 7, 4 and 1, respectively. (a) Sample 7 exhibits no visible darkening or reduction through the sample cross section. (b) Sample 4 exhibits a slight reduction through the cross section as evidenced by the darkened region at the top surface of the sample. (c) Sample 1 exhibits significant reduction through the cross section, and the 'tongue shaped' reduction front can clearly be seen. (d,e,f) Layered samples 9, 5 and 1, respectively. No reduction is seen in the cross section of any of the layered samples. The direction of current flow was from top to bottom in each of these images.

Finally, the interface between the Ni and YSZ found in layered samples has been characterized by scanning electron and transmission electron microscopy. Figure 5.7 shows representative examples of the interface that forms during sintering. There is a notable lack of intermetallic or oxide reaction products at the Ni/YSZ interfaces that have been sampled. Figure 5.7 also shows the significant porosity found in many samples, indicating incomplete sintering.

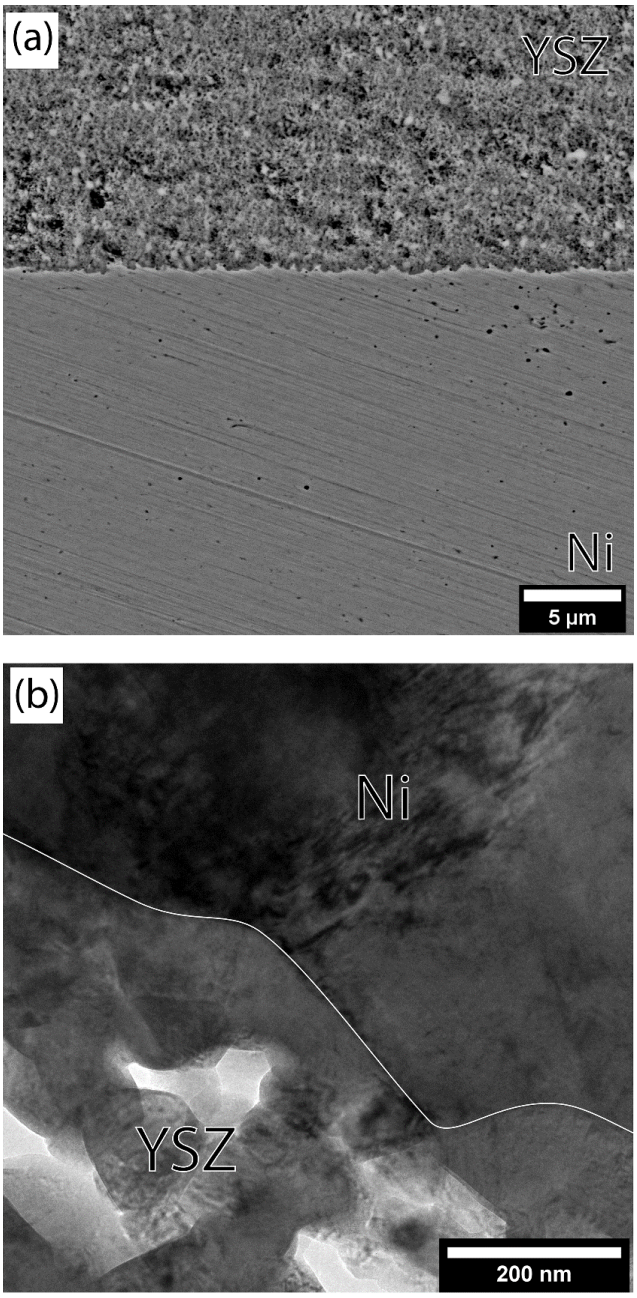

Figure 5.7: (a) Backscatter scanning electron micrograph of a Ni/YSZ interface showing the porous YSZ and the interface with the sintered Ni. Backscatter contrast does not show the presence of a third phase at the interface. (b) Transmission electron micrograph of the Ni/YSZ interface showing no evidence of oxide or intermetallic reaction products at the interface. The interface has been outlined for clarity. Large degrees of porosity indicative of incomplete sintering may again be seen in the YSZ.

5.4 Discussion

Previous reports of SPS processing of YSZ have not included significant discussion of variability or homogeneity of samples prepared under identical instrument parameters. The data presented in this study and the following discussion highlight the need for consistent and transparent reporting of processing variability to both ease the transition of SPS techniques into broader application sectors and to provide new insight on the fundamental densification mechanisms associated with different material classes. Thus, the set of processing parameters used in this study were thoughtfully selected to fall within ranges that have previously been used in SPS processing of YSZ. Figure 5.2 shows that the temperature which was selected (1100°C) falls below a steep increase in hardness and densification that occurs around 1150°C. This means that samples processed at 1100°C should have densification behavior less sensitive to variations in temperature than if processing was done at higher temperatures. The variability in hardness (density) and reduction between and within these samples are further discussed herein, including potential extension to mechanistic underpinnings.

5.4.1 Variability in Hardness

Density of ceramic bodies is frequently measured using the Archimedes method or pycnometry. However, these techniques measure the global density of the material. Here, Vickers indentation has been used to measure hardness as an analog for the density of the material, such that local variation of the property can be recorded by indenting along a cross section of each pellet that has been sintered. The Vickers hardness of the pellet decreases as the density of the pellet decreases [22]. In this way, density variations between pellets as well as within single pellets may be quantified and compared.

It is clear from Figure 5.4(a) that the median hardness achieved in the bare samples is greater than the median hardness observed for layered samples. In fact, the mean hardness of the bare set is greater than the maximum hardness for the layered set. The mean hardness for the bare samples was 2887 MPa compared to a mean of 1892 MPa for the layered samples. It is also notable that the range of properties observed in the bare samples (as denoted by the 1.5 IQR whiskers) is greater than that observed in the layered samples. The standard deviation in hardness for the bare samples was 1919 MPa whereas the standard deviation for the layered samples was only 874 MPa.

The variation in hardness for both configurations is significant, but it is clear that the bare samples exhibit much greater variation in hardness across all the samples measured. This suggests that under the selected processing conditions, the variability in the density is highest between different bare samples. The variation in hardness was also measured for the Ni layers in the layered configuration. The Ni exhibited much less variability in hardness than either of the sets of YSZ samples, indicating that the variability is increased in the YSZ layers compared to a metallic layer. The data represented in Figure 5.4(a) compares the range of hardness values between the two configurations in general. It is also important to explore the variability within individual samples of each set to gauge whether this variability arises solely from differences in hardness between the samples, or if heterogeneity in hardness within individual samples also contributes. Box-and-whisker plots for each individual sample have also been plotted as shown in Figure 5.4(b).

Careful inspection of Figure 5.4(b) reveals that bare samples 1, 2 and 3 exhibit a larger range in hardness than the other samples. It is interesting to note that bare samples 4-10 have hardness values much closer to those typical for the layered samples. Comparing Figures 5.4(a) and 5.4(b) it is noted that layered samples have much less scatter in their hardness individually as well as overall. It is also observed in Figure 5.4(b) that samples with high mean and median hardness have a wider distribution of hardness across the individual sample. This is not universally true, however, given that bare sample 5 exhibited a high mean and median hardness but also had a relatively small range in measured hardness. It can therefore be inferred that, under the selected processing conditions, samples that densify more are often doing so in a non-uniform manner. Uniform densification clearly remains possible; however, the specific conditions that lead to uniform densification of bare samples remain unclear. Other observable differences in the samples, e.g .color, may provide additional clues.

5.4.2 Variability in Reduction

It is well documented that YSZ darkens due to reduction and loss of oxygen [23]. This process occurs when YSZ is exposed to reducing environments, but also occurs during ionic transport driven by electric potentials across the material [23]. In SPS, a reducing environment (carbon die at high temperature under vacuum) is combined with an electric potential and current that also can drive oxygen transport and reduction. Furthermore, both the electronic and ionic conductivity of YSZ changes as a function of temperature and oxygen vacancy concentration,

which means that the conductivity of YSZ will increase during the SPS consolidation process [15,24].

Of all the samples prepared in this study, only bare samples exhibited visible reduction (darkening), however, not all of the bare samples exhibited the same degree of reduction through the cross section. Figure 5.6 shows that in some cases bare samples exhibited no visible darkening while other samples showed reduction across much of the cross section. The layered samples, however, showed no visible darkening in any of the samples produced. Interestingly, the samples with the highest degree of visible reduction correlated to samples with the greatest variations in hardness (i.e. bare samples 1-3).

As mentioned previously, there are two likely driving forces for oxygen loss during sintering. The first probable cause of oxygen transport is the reducing atmosphere created by the carbon die and the vacuum in the SPS chamber. At high temperature, it is expected that this factor would cause oxygen transport out of the YSZ equally from all surfaces. This type of reduction has been observed during hot isostatic pressing of YSZ, since samples are exposed to high temperatures and reducing environments, but not to electric fields or currents [25]. Alternatively, an electric potential applied across YSZ is known to cause blackening starting at one side of the specimen and progressing to the other. Janek and Korte [23] described a characteristic "tongue-shaped" reduction front that is observed in several of the reduced bare samples in this study, an example of which can be seen in Figure 5.6(e). The configuration of these reduced regions, where observed, would suggest that the reduction of the bare samples is largely electrically driven rather than thermally driven. Considering that the thermal diffusion distance of oxygen over only 10 minutes at 1100ºC is expected to be quite small (on the order of 30 μm when calculated using bulk YSZ diffusion values [26]), such electrically driven reduction is reasonable via SPS. It follows then, that reduced samples experienced at least some direct current passage, while the current likely bypassed those samples with little or no evident reduction. This is contrary to reported simulated current distributions through YSZ during SPS. These models have described current passing exclusively around the sample, much like the simulated current path around an insulating sample such as alumina [27].

Samples exhibiting significant degrees of electrically-driven reduction during sintering correlate to samples with high hardness and high variability in hardness. Together, these observations suggest that high hardness (and similarly, high density) is achieved when current

passes through the sample itself, rather than through the die adjacent to the sample. However, it also suggests that for YSZ, when current passes through the sample, the microstructural homogeneity suffers. Furthermore, the heterogeneity does not appear to be a function of location within bare samples, suggesting that differences in hardness across samples is not a result of pressure gradients, but is more likely due to differences in electrical and ionic conduction. No reduction is observed in any of the layered samples, which is consistent with the original goal of the Ni layer—to intentionally reduce or eliminate current in the YSZ layer by providing a highly conductive alternate pathway. This seems to be corroborated by the lower hardness and lower variability in hardness observed in these samples. By adding a highly conductive capping layer to the YSZ, current passing through the sample can be avoided, resulting in less dense but also more homogeneous samples.

The assumption that little or no current passes through the Ni into the YSZ is supported by the observation that there is no reaction between the two materials at either Ni/YSZ interface. Figure 5.7 shows representative scanning electron and transmission electron micrographs of the Ni/YSZ interface. The formation of intermetallics and Ni oxides are well known indicators of current flowing between Ni and YSZ [28,29]. However, no evidence of intermetallic formation or oxidation of the Ni was found, thus, the lack of these reaction products in the samples here suggests that current does not flow across this interface in the layered samples.

5.4.3 Implications About Processing and Sintering Mechanisms

In current SPS processing literature it is common to report properties such as hardness or density for a given processing condition without error bars. The data reported here demonstrate that such practices may, at least in some instances, be misleading. In the case of the processing conditions outlined herein, if only one sample in the bare configuration had been prepared, the hardness that may have been reported could have varied by nearly an order of magnitude. This is obviously concerning. Clearly, for the processing conditions used in this study, prediction of the resultant sample properties with any degree of certainty would have been impossible, especially if the bare sample configuration was used.

The current body of literature also reports a wide range of possible mechanisms that may be responsible for densification during processing by SPS. However, there has been little conclusive evidence to show the precise role that the high current plays in densifying different

materials. It is generally accepted that the path of the electric current depends on the electrical conductivity of the material being processed, with conductive materials allowing more current to pass directly through the sample powder and insulators causing the current to pass through the surrounding die and heat the sample indirectly. However, in ionic conductors like YSZ, the current flow through the specimen may evolve with the onset and progress of densification. Once YSZ begins to reduce, much more current may pass through the sample, but may do so heterogeneously, making predicting the path of the current more complex.

In this study, it is observed that the current path affects densification of YSZ significantly. Those samples exhibiting greater degrees of reduction over the cross-section correlate to samples with higher relative hardness, thereby suggesting that increased sample conductivity (associated with blackening and reduction) may be correlated with increased densification. Moreover, incomplete reduction translates to increased microstructural heterogeneity. A more comprehensive picture emerges from these two observations: as a sample begins to reduce, more current passes through the portion of the sample that has reduced, causing increased densification in those regions, whereas, unreduced regions experience a current abatement, thus diminishing the rate of densification. For layered samples, the path of the current has been intentionally prevented from passing through the YSZ. The diminished hardness and absence of blackening/reduction in these samples further suggests that current flow through the samples plays a significant role in the rapid densification of YSZ specifically and possibly other mixed conductors. Beyond this, it is impossible to make more specific conclusions about the mechanisms responsible for the densification or lack thereof observed here.

5.5 Conclusion

Continued adoption and maturation of SPS processing methods requires significant advancements in reduction and control of processing related variability. This effort provides a case study to demonstrate the potential magnitude of such variations in a seemingly well studied materials system, yttria stabilized zirconia. Using hardness measurements as a proxy for local density and microstructural heterogeneities, and visible evidence of reduction as an indicator of inhomogeneous ionic/electronic conductivity, a correlation between current pathways and enhanced densification has been inferred. This is corroborated through use of a layered sample configuration, in which the current was intentional routed around the YSZ layer. Little or no

reduction was observed in the layered samples. Likewise, the average hardness, thereby the density, was reduced but more uniform across and between the layered samples. These conclusions were only afforded through systematic characterization of at least ten specimens in each configuration. Through consistent characterization and reporting of intrinsic property variations, along with more thorough, statistically derived descriptions of SPS processing parameters, it may be possible to provide greater insight on the fundamental mechanisms underlying SPS consolidation while simultaneously imparting greater confidence and reproducibility to the technique.

5.6 References

[1] Z.A. Munir, U. Anselmi-Tamburini, M. Ohyanagi, The effect of electric field and pressure on the synthesis and consolidation of materials: A review of the spark plasma sintering method, J. Mater. Sci. 41 (2006) 763–777. https://doi.org/10.1007/s10853-006-6555-2.

[2] L. Wang, J. Zhang, W. Jiang, Recent development in reactive synthesis of nanostructured bulk materials by spark plasma sintering, Int. J. Refract. Met. Hard Mater. 39 (2013) 103–112. https://doi.org/10.1016/j.ijrmhm.2013.01.017.

[3] O. Guillon, J. Gonzalez-Julian, B. Dargatz, T. Kessel, G. Schierning, J. Räthel, M. Herrmann, Field-assisted sintering technology/spark plasma sintering: Mechanisms, materials, and technology developments, Adv. Eng. Mater. 16 (2014) 830–849. https://doi.org/10.1002/adem.201300409.

[4] R.H.R. Castro, K. van Benthem, Sintering, 2013. https://doi.org/10.1007/978-3-642-31009-6.

[5] D. Schwesig, G. Schierning, R. Theissmann, N. Stein, N. Petermann, H. Wiggers, R. Schmechel, D.E. Wolf, From nanoparticles to nanocrystalline bulk: Percolation effects in field assisted sintering of silicon nanoparticles, Nanotechnology. 22 (2011). https://doi.org/10.1088/0957-4484/22/13/135601.

[6] A. Becker, S. Angst, A. Schmitz, M. Engenhorst, J. Stoetzel, D. Gautam, H. Wiggers, D.E. Wolf, G. Schierning, R. Schmechel, The effect of Peltier heat during current activated densification, Appl. Phys. Lett. 101 (2012) 1–5.

https://doi.org/10.1063/1.4731272.

[7] J. Langer, M.J. Hoffmann, O. Guillon, Electric field-assisted sintering in comparison with the hot pressing of yttria-stabilized zirconia, J. Am. Ceram. Soc. 94 (2011) 24–31. https://doi.org/10.1111/j.1551-2916.2010.04016.x.

[8] P. Dahl, I. Kaus, Z. Zhao, M. Johnsson, M. Nygren, K. Wiik, T. Grande, M.A. Einarsrud, Densification and properties of zirconia prepared by three different sintering techniques, Ceram. Int. 33 (2007) 1603–1610. https://doi.org/10.1016/j.ceramint.2006.07.005.

[9] T. Takeuchi, I. Kondoh, N. Tamari, N. Balakrishnan, K. Nomura, H. Kageyama, Y. Takeda, Improvement of Mechanical Strength of 8 mol % Yttria-Stabilized Zirconia Ceramics by Spark-Plasma Sintering, J. Electrochem. Soc. 149 (2002) A455. https://doi.org/10.1149/1.1456915.

[10] Z. Shen, M. Johnsson, Z. Zhao, M. Nygren, Spark Plasma Sintering of Alumina, J. Am. Ceram. Soc. 85 (n.d.) 1921–1927. https://doi.org/10.1111/j.1151-2916.2002.tb00381.x.

[11] G. Molénat, L. Durand, J. Galy, A. Couret, Temperature Control in Spark Plasma Sintering: An FEM Approach, J. Metall. 2010 (2010) 1–9. https://doi.org/10.1155/2010/145431.

[12] E.A. Olevsky, S. Kandukuri, L. Froyen, Consolidation enhancement in spark-plasma sintering: Impact of high heating rates, J. Appl. Phys. 102 (2007). https://doi.org/10.1063/1.2822189.

[13] J. Zhao, T. Holland, C. Unuvar, Z.A. Munir, Sparking plasma sintering of nanometric tungsten carbide, Int. J. Refract. Met. Hard Mater. 27 (2009) 130–139. https://doi.org/10.1016/j.ijrmhm.2008.06.004.

[14] S.I. Cha, S.H. Hong, Microstructures of binderless tungsten carbides sintered by spark plasma sintering process, 356 (2003) 381–389. https://doi.org/10.1016/S0921-5093(03)00151-5.

[15] J.-H. Park, R.N. Blumenthal, Electronic Transport in 8 Mole Percent Y2O3-ZrO2, J. Electrochem. Soc. 136 (1989) 2867. https://doi.org/10.1149/1.2096302.

[16] U. Anselmi-Tamburini, J.E. Garay, Z.A. Munir, A. Tacca, F. Maglia, G. Spinolo, G. Chiodelli, G. Spinolo, Spark plasma sintering and characterization of bulk nanostructured fully stabilized zirconia: Part II. Characterization studies, J. Mater. Res. 19 (2004) 3263–3269. https://doi.org/10.1557/JMR.2004.0424.

[17] U. Anselmi-Tamburini, J.E. Garay, Z.A. Munir, A. Tacca, F. Maglia, G. Spinolo, Spark plasma sintering and characterization of bulk nanostructured fully stabilized zirconia: Part I. Densification studies, J. Mater. Res. 19 (2004) 3255–3262. https://doi.org/10.1557/JMR.2004.0423.

[18] X.J. Chen, K.A. Khor, S.H. Chan, L.G. Yu, Preparation yttria-stabilized zirconia electrolyte by spark-plasma sintering, Mater. Sci. Eng. A. 341 (2003) 43–48. https://doi.org/10.1016/S0921-5093(02)00079-5.

[19] K.A. Khor, L.G. Yu, S.H. Chan, X.J. Chen, Densification of plasma sprayed YSZ electrolytes by spark plasma sintering (SPS), J. Eur. Ceram. Soc. 23 (2003) 1855–1863. https://doi.org/10.1016/S0955-2219(02)00421-1.

[20] H.B. Zhang, B.-N. Kim, K. Morita, H. Yoshida, J.-H. Lim, K. Hiraga, Optimization of high-pressure sintering of transparent zirconia with nano-sized grains, J. Alloys Compd. 508 (2010) 196–199. https://doi.org/https://doi.org/10.1016/j.jallcom.2010.08.045.

[21] Standard Test Method for Vickers Indentation Hardness of Advanced Ceramics BT - Standard Test Method for Vickers Indentation Hardness of Advanced Ceramics, (15AD).

[22] J. Luo, R. Stevens, Porosity-dependence of elastic moduli and hardness of 3Y-TZP ceramics, Ceram. Int. 25 (1999) 281–286. https://doi.org/10.1016/S0272-8842(98)00037-6.

[23] J. Janek, C. Korte, Electrochemical blackening of yttria-stabilized zirconia â□□ morphological instability of the moving reaction front, Solid State Ionics. 116 (1999) 181–195. https://doi.org/10.1016/S0167-2738(98)00415-9.

[24] C. Ahamer, A.K. Opitz, G.M. Rupp, J. Fleig, Revisiting the Temperature Dependent Ionic Conductivity of Yttria Stabilized Zirconia (YSZ), J. Electrochem. Soc. 164 (2017) F790–F803. https://doi.org/10.1149/2.0641707jes.

[25] M. Koizumi, Hot Isostatic Pressing— Theory and Applications, 2007.

[26] R.A. De Souza, M.J. Pietrowski, U. Anselmi-Tamburini, S. Kim, Z.A. Munir, M. Martin, Oxygen diffusion in nanocrystalline yttria-stabilized zirconia: the effect of grain boundaries, Phys. Chem. Chem. Phys. 10 (2008) 2067–2072. https://doi.org/10.1039/b719363g.

[27] C. Manière, G. Lee, E.A. Olevsky, All-Materials-Inclusive Flash Spark Plasma Sintering, Sci. Rep. 7 (2017) 1–8. https://doi.org/10.1038/s41598-017-15365-x.

[28] T. Wagner, R. Kirchheim, M. Ruhle, Electrochemically-Induced Rreactions AT Ni / ZrO2 Interfaces, Acta Metall. Mater. 40 (1992) S85-93. http://www.sciencedirect.com/science/article/pii/095671519290267I?via=ihub.

[29] T. Wagner, G. Duscher, Decomposition of the ZrO 2 electrolyte in contact with Ni : Structure and chemical composition of the Ni – electrolyte interface, J. Mater. Res. 14 (1999) 3340.

CHAPTER 6

SUMMARY AND FUTURE DIRECTIONS

This study has provided new insights into the relationship between microscale ferroelastic domain nucleation processes and the bulk deformation response of the material. Additional insights into the spark plasma sintering method used for processing ceramics have also been presented. The results outlined here have implications that improve the overall understanding of processing-microstructure-property relationships that exist for ferroelastic ceramics. In this chapter, the key results gained from this research will be concisely summarized. Utilizing this improved understanding of ferroelasticity will provide insight into methods that can be utilized for informed design of toughened ceramic microstructures in the future. Furthermore, several aspects of the research outlined here were preliminary, therefore, several continued and additional experiments that may expand upon this work will be outlined here.

6.1 Summary

This dissertation primarily discussed the multiscale characterization of ferroelastic deformation in ceramic materials, with the main objective focused on understanding the relationship between local microstructure and ferroelastic domain nucleation behavior. With improved understanding of how specific microstructural features influence ferroelastic domain nucleation, those features can be tuned when designing ceramic materials to improve their intrinsic toughness.

Firstly, characterization of the domain nucleation process in single crystals of CTZ was discussed. This microscale aspect of this research revealed that domain nucleation in single crystal CTZ micropillars did not adhere to a critical resolved shear stress criterion, but rather exhibited non-Schmid behavior. Furthermore, this study indicated that several deformation mechanisms may be active in close competition or cooperation in single crystals. Dislocation plasticity, microcracking, as well as evidence of displacive and dislocation mediated twinning were all observed. This work specifically highlighted the effect of orientation on ferroelastic coercive stress. These results complement previous work which had largely characterized coercive stresses only as a bulk property or had focused on stresses required for domain motion rather than nucleation. Here, the data suggests that on a single crystal basis, quantifying coercive stress for

domain nucleation is more complex due to the convoluted mechanisms involved in the twin formation.

Secondly, domain nucleation in the same CTZ material was evaluated in bulk polycrystalline microstructures. Microindentation was used to deform large numbers of grains in several samples with different overall grain size distributions. Analysis showed that larger grains within a given sample more frequently nucleated multiple domains than smaller grains in the same regions. Furthermore, undeformed nearest neighbor grains to grains that contained ferroelastic twins were significantly smaller than the average grain size. The nucleation of twins was also shown to be sensitive to the stress state applied to the samples. Therefore, twin nucleation was linked to high local shear stresses that develop in locally heterogenous microstructures such as polycrystals. The same shear stress localization does not occur in single crystal nanopillars, which deform at considerably higher stresses than have been reported as coercive stresses for similar tetragonal zirconia materials previously.

Finally, the variability in ionic conducting YSZ samples processed using spark plasma sintering was investigated. By processing multiple samples with different geometries using identical SPS parameters, significant variability between samples as well as within individual samples was shown. Inserting a conducive capping layer around the YSZ resulted in decreased overall densification as well as increased consistency in the resulting properties. Samples that did not have the conductive layers exhibited varyind degrees of electrochemical reduction resulting from electric current (or lack thereof) passing through the sample during densification. These results indicate that electric current plays an important role in the densification of YSZ processed by SPS. Furthermore, these results suggest that the properties of certain types of materials processed using this technique can be highly variable and that care should be taken in ensuring diligent reporting of processing conditions and validation of resulting material properties.

Together, these multiscale studies have indicated that domain nucleation processes in single crystals are complex, however, microstructural features such as grain size can still serve as indicators of how much ferroelastic deformation can be achieved in a material. Although individual crystal orientation may not predict domain nucleation within a grain, the local microstructural environment can still be tuned to increase the probability of deformation through domain nucleation rather than through fracture. This work also highlights that care should be taken

in determining appropriate processing conditions to achieve these desired microstructures for ceramics. These results also indicate a number of promising future directions that can be taken to further improve our understanding of ferroelastic deformation. The present results along with the additional experiments that will be proposed will enable a more informed design of intrinsically toughened microstructures in the future.

6.2 Future Directions

There were a number of experiments and techniques outlined in this dissertation that showed promising preliminary results for evaluating additional characteristics of ferroelastic deformation. Several future routes that may be taken to expand upon what has been learned here will be outlined.

6.2.1 Additional Evaluations of Single Crystals

One aspect of the domain nucleation process observed in this study that warrants further investigation is the presence of incommensurate modulations and ordering resulting from the domain nucleation. This type of ordering has been previously observed in domains nucleated by deformations in coarse grained polycrystals [1] and was observed again in domains nucleated by Vickers indentation in this study, however, they have not been definitively observed in the domains that nucleate in small scale single crystal samples. To determine whether finer domains that nucleate in micropillars and nanopillars also exhibit similar incommensurate modulation, additional sections of pillars should be made. Selected area electron diffraction specifically targeting the [100] zone axis, should be collected to check for the presence of superlattice reflections that indicate the presence of the ordering. Determining whether fine domains that nucleate at small size scales exhibit ordering will lend insight into whether the mechanism responsible for domain nucleation is different in coarse grained polycrystals than in small scale crystals. Beyond this, high resolution STEM imaging can be used to image fine domains to determine the structure at the tip of needle-like domains, and characterization of the types of dislocations should be done. This may provide further insight into the dislocation mediated twinning mechanism compared to the bulk twinning mechanisms.

Additional mechanical tests may also be used to measure any microplasticity present prior to domain nucleation. One method that may be useful in determining whether there is any

dislocation activity prior to large scale deformation in ferroelastic single crystals is using the Onset of Plasticity via Relaxation Analysis (OPRA) described by Pandy et al. [2]. OPRA was developed to more accurately determine yield points using small scale stress relaxation tests. This test methodology may be adapted to ceramic micropillar compression experiments to determine whether dislocation activity precedes domain nucleation in some or all cases of deformation observed in CTZ micropillars. To accomplish this, additional micropillar compression tests should be done but instead of using a constant displacement rate for the loading function, alternating steps of loading and holding should be used (similar to how the SEM-DIC tests are performed as outlined in Chapter 2). Any relaxation of the load during the holding segments are indicative of plastic deformation. Therefore, by using carefully incremented loading of CTZ micropillars, these tests may be used to further determine whether dislocation plasticity is associated with domain nucleation and to increase the distinction between different deformation mechanisms active in ferroelastic single crystals.

Lastly, incorporating computational methods into future evaluations of ferroelastic deformation could provide additional insight into the domain nucleation mechanisms. If energy terms such as the twin boundary energy and surface energy can be computed for CTZ (or other ferroelastics), the relationship between crystal volume and energy minimization through twin boundary formation may be quantified. Molecular dynamics simulations, like those that have been performed by Zhang and Asle Zaeem [3] to study deformation in YSZ nanopillars, could be performed to compare the simulated deformation to experimentally observed deformation mechanisms. Finite element analysis techniques, like those used by Hu [4], may also prove useful in quantifying stresses responsible for deformations observed in the various geometries used for in situ TEM deformation experiments described in Chapter 2.

6.2.2 Additional Evaluations in Polycrystals

Although grain size has been thoroughly evaluated as a variable affecting domain nucleation in polycrystalline microstructures in this work, there are other variables that warrant further examination. Preliminary results were collected on the orientations of grains that nucleated multiple domains within polycrystals, however, comprehensive statistics and additional analysis is still required. Figure 6.1 shows the orientations of grains that contained twins surrounding a Vickers indent like those indents used for the grain size analysis discussed in Chapter 4. However,

these results have so far been limited by poor indexing using traditional Hough based EBSD indexing techniques, and there are too few results to confidently determine whether favorable orientations for twinning in bulk exist.

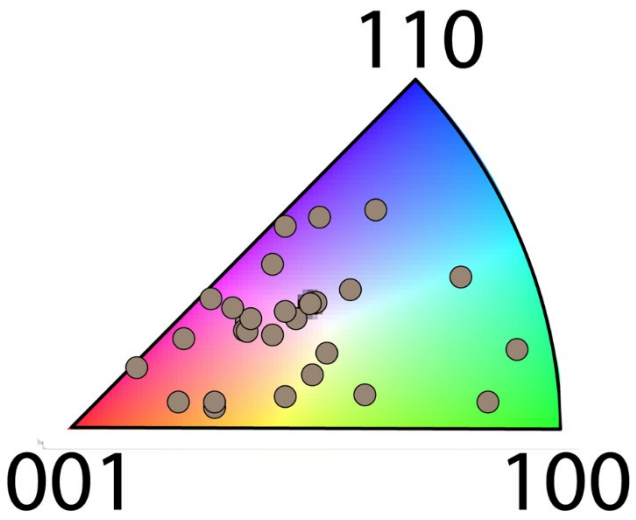

Figure 6.1: An inverse pole figure schematic for tetragonal zirconia showing the orientations of grains containing twins in a deformed polycrystalline microstructure.

By collecting additional statistics on the orientations of grains that contain twins it will be possible to determine whether a favorable orientation exists within a polycrystalline microstructure for domain nucleation. To accomplish this, the advanced indexing methods using dictionary indexing described in Chapter 2 should be used. Dictionary indexing using EMsoft was attempted as outline in Chapter 2, however, additional work should be done to validate its utility in improving indexing of CTZ materials. If reliability of indexing can be improved, and misindexing due to pseudosymmetry eliminated, then many more maps of deformed microstructures can be confidently collected. Data processing using existing software such as EDAX OIM will then become significantly more useful for easily identifying grains and twin boundaries. Perhaps an even more promising aspect of collecting orientation maps of deformed regions will be evaluating whether specific orientation relationships exist between neighboring grains that twin, or grains that twin but whose neighbors do not. The results discussed in Chapter 4 indicate that domain conformations depend on the local microstructural environment, therefore evaluating the local orientations and misorientations associated with various conformations (such as when twins appear to transcend grain boundaries) will be highly insightful. Furthermore, using the elastic tensor

combined with orientation maps, relative stiffnesses of grains can be determined, and an improved picture of how elastic anisotropy affects domain nucleation can be developed.

Another variable that can be measured using techniques developed in this dissertation is the strain, and more specifically, the strain heterogeneity that develops within polycrystalline microstructures during ferroelastic deformation. Mechanical compatibility locally between grains within a polycrystal has been identified to contribute to the domain nucleation behavior, therefore, measuring the local stains that develop as the microstructure deforms will increase our understanding of how microstructure influences this process. SEM-DIC enables this measurement of the local strain associated with a domain nucleation events. The strain can be measured in the twinned grains along with residual elastic strains that remain in grains that did not twin. Furthermore, as Kammers and Daly [5] showed, strain mapping using SEM-DIC can be combined with information about the crystallography obtained using EBSD. The combination of these techniques enables overlaying Schmid factors or elastic stiffness maps with *in situ* observations of the deformation. A fruitful experiment for ferroelastic polycrystals could be performed using these techniques to measure local strain associated with individual grain nucleation events and compare that to the global strain applied by the load frame while simultaneously knowing crystallographic orientations associated with the deformation. Perhaps a similar analysis as that done by Daniels et al. [6] could be done to quantify the deviation in domain switching strain from the average strain.

These additional *in situ* tests may also be combined with further *ex situ* measurements utilizing techniques that enable correlation of local stresses to observe domain nucleation events. An example of this was briefly outlined in Chapter 4, and may utilize Hertzian indentation. Since shear stresses can be measured as function of depth beneath a spherical indent, cross-section created below Hertzian indents can be used to identify the shear stress at locations where twins are observed. This has the added benefit of observing microstructures that were fully three-dimensionally constrained at the time of deformation, rather than surfaces which lack some of the constraints that may influence the deformation process.

This work may be extended to other materials compositions and other microstructures. For instance, by varying the composition of CTZ, the lattice parameters, tetragonality ratios, and phase fraction of the tetragonal phase can be controlled. Therefore, opportunity still exists to evaluate the influence these variables have on various aspects of ferroelastic deformation. Similarly, other

overall compositions such as barium titanate and lanthanum cobaltite that were mentioned in Chapter 2 could be used for similar mechanical testing that has been done on and proposed for existing CTZ materials. BTO and LCO both exhibit abnormal grain growth which may provide favorable microstructures for increased ferroelastic deformation. Therefore, mechanical and microstructural evaluation performed on these materials may be used to further validate microstructural conditions that are favorable for ferroelastic deformation. Composite microstructures consisting of relatively mechanically soft ferroelastics embedded in stiffer matrix grains may also be fabricated and evaluated.

Finally, beyond the opportunity to test the effect of composition and phase on the deformation behavior, utilizing other compositions allows for the influence of temperature to also be incorporated. So far, all of the mechanical evaluations discussed in this dissertation were done at ambient temperature. By utilizing hot stages in conjunction with *in situ* mechanical tests, the effect that temperature has on the deformation can be combined with the other variables that have already been evaluated. This may prove particularly useful when testing materials such as barium titanate that have phase transitions temperatures (Curie temperatures) that are easily obtained using existing instrumentation.

6.2.3 Final Remarks

Overall, this dissertation represents the successful development of an improved understanding of the influence that local microstructure has on ferroelastic deformation in ceramics. The influence of crystal orientation and grain size have been thoroughly characterized, and their effects on domain nucleation behaviors have been quantified. Several additional promising routes of examination were also identified and outlined, paving the way for additional insight to be developed in the future. The insights gained by this work may be used to improve the fundamental understanding of deformation mechanisms in ceramics, and as a baseline for improved design of intrinsically toughened ceramics microstructures in the future.

6.3 References

[1] J.A. Krogstad, M. Lepple, C.G. Levi, Opportunities for improved TBC durability in the CeO2-TiO2-ZrO2 system, Surf. Coatings Technol. 221 (2013) 44–52. https://doi.org/10.1016/j.surfcoat.2013.01.026.

[2] A. Pandey, R. Wheeler, A. Shyam, T.B. Stoughton, Onset of Plasticity via Relaxation Analysis (OPRA), Exp. Mech. 56 (2016) 1095–1107. https://doi.org/10.1007/s11340-016-0152-3.

[3] N. Zhang, M. [Asle Zaeem], Competing mechanisms between dislocation and phase transformation in plastic deformation of single crystalline yttria-stabilized tetragonal zirconia nanopillars, Acta Mater. 120 (2016) 337–347. https://doi.org/https://doi.org/10.1016/j.actamat.2016.08.075.

[4] Y. Hu, J.-H. Huang, J.-M. Zuo, In situ characterization of fracture toughness and dynamics of nanocrystalline titanium nitride films, J. Mater. Res. 31 (2016) 370–379. https://doi.org/10.1557/jmr.2016.4.

[5] A.D. Kammers, S. Daly, Digital Image Correlation under Scanning Electron Microscopy: Methodology and Validation, Exp. Mech. 53 (2013) 1743–1761. https://doi.org/10.1007/s11340-013-9782-x.

[6] J.E. Daniels, M. Majkut, Q. Cao, S. Schmidt, J. Wright, W. Jo, J. Oddershede, Heterogeneous grain-scale response in ferroic polycrystals under electric field, Sci. Rep. 6 (2016) 22820. https://doi.org/10.1038/srep22820.